Development of a Label-Free, Non-Faradaic Impedimetric Biosensor for the Monitoring of Caspase-9 in Mammalian Cell culture

Boyang Chen

A thesis submitted in partial fulfilment of the requirements of the University of the West of England, Bristol

for the degree of Doctor of Philosophy

Faculty of Environment and Technology, University of the West of England, Bristol

May 2024

Abstract

Development of a Label-Free, Non-Faradaic Impedimetric Biosensor for the Monitoring of Caspase-9 in Mammalian Cell culture

By

Boyang Chen

Doctor of Philosophy in Biotechnology

University of the West of England, 2023

Professor Janice Kiely, Director of Studies

Lower yields and poorer quality of biopharmaceutical products result from cell death in bioreactors. Such cell death is commonly associated with programmed cell death or apoptosis. During apoptosis, caspases are activated and cause a cascade of events that eventually lead to cell destruction. In this thesis an impedance spectroscopy measurement technique for the detection of caspase-9 in buffer and a complex fluids, culture media, is reported. Enhanced sensitivity is achieved by leveraging the physiochemical properties of zinc oxide and copper oxide at the electrode-solution interface. Characterisation of the biosensor surface was performed using scanning electron microscopy and indirectly using an enzyme-linked immunosorbent assay. The characteristic biomolecular interactions between the target analyte and specific capture probe of the biosensor are quantified using non-faradaic electrical impedance spectroscopy (EIS). The developed biosensor demonstrated a detection limit of 0.07 U/mL (0.032 μM) in buffer. The sensor requires a low sample volume of 50 μL without the need for sample dilution, facilitating rapid analysis. Using a luminescence-based assay, the presence of active caspase-9 was detected in the culture media following exposure to a pro-apoptotic agent. It is envisioned that the caspase-9 biosensor will be useful as a cell stress screening device for apoptosis monitoring.

Thesis Structure

To provide background to the chosen application area, in chapter 1, the significance of caspase-9 in apoptosis and the need for apoptosis monitoring in industrial cell lines is discussed. Issues with the current techniques for apoptosis detection are also addressed. In addition, the basic components of a biosensor are described and various biosensing approaches cited in the literature have been identified. These methods were compared and, in so doing, the benefits associated with label-free, antibody-based impedimetric biosensors are highlighted. To strengthen the case for adoption of the impedimetric approach, explanations of the measurement principles, e.g. comparing faradaic with non-faradaic arrangements, are provided in chapter 2.

Zinc oxide (ZnO)/copper oxide (CuO) composites have shown great promise as sensor surface materials, delivering high sensitivity biosensors. In this work, this approach has been applied for the detection of caspase-9. In chapter 3, methodologies for fabrication of ZnO/CuO sensor surfaces using a sonication-based technique are evaluated and results of the morphological and biochemical characterisation of the fabricated surfaces are presented. The main focuses in the thesis was the use of impedance spectroscopy to quantify caspase-9. The 1% ZnO/1% CuO biosensor demonstrated a linear range from 1 – 16 nM, with a limit of detection of 0.33 nM. In addition, an equivalent circuit model (described in chapter 2) was fitted to enhance understanding of the biomolecular events occurring at the sensor surface.

To evaluate the biosensors performance as a method of monitoring the vitality of cell culture systems, Chinese hamster ovary (CHO) cell culture samples were used. The cells were

subjected to apoptotic agents and the changes in impedance signal were compared and the relationship between caspase-9 activity and concentration was explored. The biosensor results were compared enzymatic capase-9 assay under similar experimental conditions to evaluate the effectiveness of the biosensor for early detection of apoptosis.

In conclusion, the label-free, non-faradaic biosensor can detect changes in caspase-9 concentration in both buffer and cell culture media. The changes in caspase-9 concentration is correlated with apoptotic progression and can provide insights on the health of the cells. Consequently, the sensor could be used in a cell culture setting and, with adaptation such as integrating the sensor in a flow-through closed loop system could enable the possibility of continuous *in situ* monitoring of apoptosis.

Contents

List of Figures

List of Tables

Abbreviations

2D - two dimensional
3D - three dimensional
Ab - antibody
AC - alternating current
APDMES - (3-aminopropyl) dimethylethoxysilane
APTES - 3-aminopropyltriethoxysilane
Bcl-2 – B cell lymphoma 2
BHK – Baby hamster kidney
CHO - Chinese hamster ovary
CRP – C-reactive protein
CuO - copper oxide
Cys – cysteine
DAPI - 4′,6-diamidino-2-phenylindole
DC - direct current
EDC - N-Ethyl-N'-(3-dimethylamino-propyl) carbodiimide hydrochloride
EDL – electrical double layer
EIS – electrical impedance spectroscopy
ELISA – enzyme-linked immunosorbent assay
Fab - fragment antigen-binding
FACS - fluorescence activated cell sorting
Fc - fragment crystallizable
FDA – Food Drug Administration
GOD - glucose oxidase enzyme
HEK-293 – Human embryonic kidney-293
LFA - lateral flow assay
Mab - monoclonal antibody
mRNA – messenger Ribonucleic acid
NC - nitrocellulose
NFIS – non-faradaic impedance spectroscopy
NFκB – Nuclear factor kappa B
NHS - N-hydroxysuccinimide
PCR - polymerase chain reaction
PFU – plaque-forming unit
PS – Phosphatidylserine
QCM - quartz crystal microbalance
RNA - Ribonucleic acid
SAM - self-assembled monolayer
SDS - sodium dodecyl sulfate
SEM - scanning electron microscopy
SPR - surface plasmon resonance
TEM - transmission electron microscopy
TNFR - tumour necrosis factor receptor
ZnO – zinc oxide

Acknowledgements

I couldn't have done my PhD without the invaluable financial support from UWE and the EPSRC studentship. During my research, I learned to think in new ways and be more creative. I took my time to grow and learn, exploring my ideas independently but also taking guidance when I needed it. Doing research taught me to explore novel approaches, designing experiments, solving problems, and articulating complex concepts. This journey wasn't just about getting smarter; it taught me how to tackle the unknown with confidence.

I want to give a huge thanks to Professors Janice Kiely and Richard Luxton for being amazing mentors in the biosensors world. They didn't just teach me about this field - they helped me become a better researcher. Working with them, I've learned so much and kept getting better at what I do. Every step forward was proof of the awesome lessons and skills I gained during our time working together. I would like to extend my thanks to Ibidapo Williams for his supervision and guidance in the cell culture lab. He helped me get up to speed with the cell culture process and various techniques. I would like to thank David Patton for his help on getting excellent cross-sectional images of the sensor using electron microscopy. I would like to thank Dr John Eveness and Alex Yue for their guidance on conducting experiments using impedance spectroscopy and data analysis. I would like to thank all the technicians and staff in the Health Tech Hub for their wonderful and academic help. Finally, I would like to thank my parents and friends for their support during my PhD journey. Their encouragement and belief in me were invaluable, providing the strength and motivation needed to navigate this challenging yet rewarding path.

Chapter 1
Introduction

1.1 Mammalian cell culture in biopharmaceutical production

It has been over three decades since the US Food and Drug Administration (FDA) approved the first biopharmaceutical product, Humulin, a biosynthetic "human" insulin made via recombinant DNA. Since then there has been a rapid increase in the number of FDA approved products produced in mammalian cell culture, starting in 1986 with the production of recombinant tissue plasminogen activator (tPA) with genetically engineered Chinese Hamster Ovary (CHO) cells and the simultaneous introduction of the first monoclonal antibody (MAb), ORTOCLONE OKT3 (muromonab-CD3) as a treatment for solid transplant rejection. The rate of product approvals and sales of MAb products have increased dramatically. In 2019, global sales revenue for all MAb drugs was US$163 billion representing about 70% of total sales for all pharmaceutical products (about $230 billion) [1].

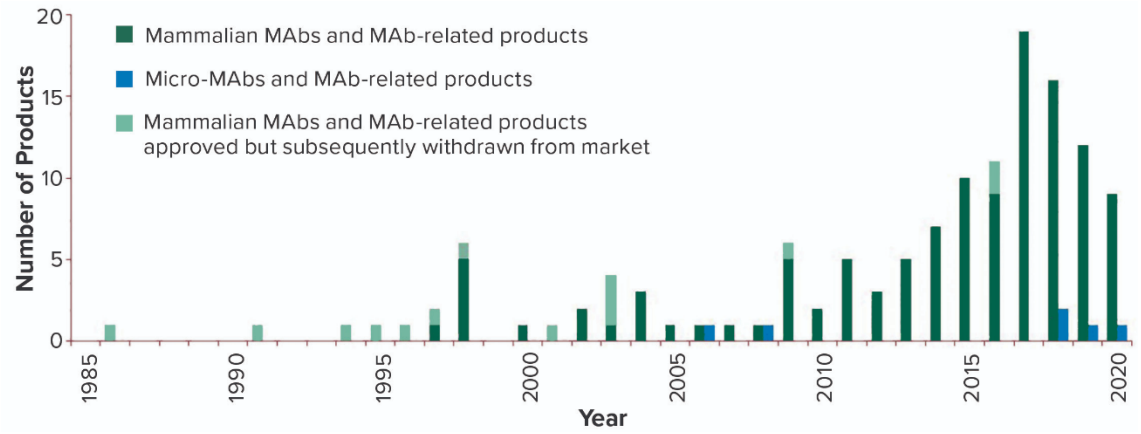

Figure 1.1 Annual approvals of monoclonal antibody products showing the number first approved for commercial sale in the United States or Europe each year since 1985; totals include all MAb and antibody-related products up to 27 August 2020. Adapted from [1].

As Figure 1.1 shows, the number of MAb products approved for commercial sale in the U.S and Europe has grown significantly, with around 3 - 5 products approved each year between 2010 and 2014, then 10 – 19 new products approved each year between 2015 and 2019.

Most therapeutic recombinant proteins are obtained by biotechnological processes [2]. Depending on the desired product properties and functionality, different expression systems may be employed including bacteria, mammalian cells, yeast, insect cells, transgenic plants, and transgenic animals [3]. New technologies are continuously being developed to improve the productivity and product quality of novel biopharmaceutics [4]. Bacterial systems such as *Escherichia coli* offers a fast growth rate with high product yield. Yeast systems can provide post-translational modifications (PTMs), but Mammalian cell lines have been used for the majority of the approved recombinant therapeutics. From 2016 to 2019, 52 of the 62 (84%) therapeutic recombinant proteins available in the market were derived from mammalian cells [3].

Protein synthetic pathways within animal cells have an innate ability for proper folding and post-translational processing of these proteins make animal cells preferable as host for producing biological components of therapeutic and diagnostic interest. As a result, mammalian cell lines have been used extensively for the production of a wide variety of biotherapeutics, including monoclonal antibodies, hormones, vaccines, enzymes, growth and blood factors. Most of these products are produced in CHO cell lines, which are considered as the “workhorse” for protein and antibody manufacturing, although NS0 mouse myeloma,

baby hamster kidney (BHK), human embryonic kidney-293 (HEK-293) and a few human derived cell lines are also used in production [5].

A major proponent of the vast improvement in bioprocess productivity and quality over the last two decades is the advancement in feeding and harvesting strategies that have taken the bioprocess from batch, to fed-batch and on to perfusion processes. Batch fermentation processes are often considered the first processes adopted by the biopharmaceutical industry [6]. Here cells are added to the culture media, which has been pre-filled with nutrients like glucose, glutamine, and minerals. The media remains the same during the entire process and is not supplemented, refilled, or exchanged at any time. The depletion of nutrient media and accumulation of toxic waste products often leads to significant population drop towards the end of the culture cycle. Fed-batch culture differs from the batch processes in that nutrients are added repeatedly throughout the culture process to replace the nutrients depleted by the increasing cell population. Control of the cells' metabolic rate is obtained by adjusting the feed rate of glucose which directly affects the growth rate and rate of respiration [6]. Fed-batch cultures have remained the prevalent bioprocessing method for many decades. Continuous bioprocessing, or perfusion technology is a newer method for cell culture processes. Here, the bioreactor can run at a fixed volume and fixed cell concentration for long periods of time. During this time the cells are continuously harvested whilst the feed media is constantly replaced, and toxic metabolites are removed [7]. Despite, the benefits of perfusion technology, regulatory issues are still a hurdle for its wide spread adoption [8].

A major challenge in mammalian cell line development is that the volumetric yield of protein is typically ~10–100 fold lower than that achieved when using microbial host systems, due to

slower growth, lower cell-based productivity and high death rate of mammalian cells [5]. As the demand for biologics continues to increase, significant pressure is on the continuous improvement of the size and volumetric productivity of commercial animal cell culture systems. Hence, to meet the market demands cells must be grown at high densities in large bioreactors for a prolonged period of time. One problem with high density culture production is the enhanced environmental stress exerted on the cells due to nutrient and oxygen transport limitations, accumulation of toxic metabolites and elevated osmolarity [9]. Consequently, often the first signs of cell stress include: prolongation of the cell cycle, up-regulation of the transcription factors NF-κB and Bcl-2, and triggering of death receptors, which activates the extrinsic apoptotic signalling pathway [5]. Under sustained and sever environmental stress, many cell lines undergo one of the two cell death mechanisms; passive cell death (necrosis) and programmed cell death (apoptosis and autophagy). Hence, many researchers have tried to explore strategies involving genetic modification of cell lines and alteration of culture media and bioreactor conditions, which usually seek to improve culture longevity, cell density, cell viability or protein productivity.

1.2 Types of cell death

For multicellular organisms, cell death is an essential biological process, that allows for normal development and homeostasis by elimination of unwanted cells [10]. In the progression of pathogenic condition of human diseases such as cancer and autoimmune diseases, cell death deregulation is prevalent [10]. There are three major types of morphologically distinct cell death: apoptosis, autophagy and necrosis [11].

Molecular mechanisms involved in various types of cell death are distinct but sometimes overlapping signalling pathways are engaged in response to specific stimuli [12]. In brief, apoptosis is defined mechanistically as a pathway of regulated cell death that involves the

sequential activation of caspases, a family of cysteine (Cys) proteases [13]. Apoptotic cell death is characterised morphologically by chromosome condensation, nuclear fragmentation, and membrane blebbing [13]. In contrast to apoptosis, necrosis is considered to be an unregulated, accidental cell death caused by non-specific, or non-physiological stress inducers and is characterised by a physically damaged cell such as vacuolization of the cytoplasm, swelling of the mitochondria, nucleus and cytoplasm that eventually leads to the rupture of the plasma membrane and the release of the intracellular contents [14,15]. Programmed cell death can sometimes result from caspase-independent signalling pathways, and these can be loosely categorized into cathepsin-dependent (autophagy) and calpain-dependent (apoptosis-like programmed cell death and necroptosis) cell death (Fig 1.2). Autophagy is sometimes described as a degradation mechanism rather than a form of cell death, although it can also induce cell death [16]. It is characterised by the formation of the autophagosome, which is a bilayer vesicle containing damaged organelles, proteins, and other cytoplasmic components [14,16]. Calcium dependent proteases, calpains, have been implicated in the apoptotic neuronal cell death pathways. Calpains appear to function upstream of caspase pathways by cleaving key proapoptotic BcL-2 proteins such as (Bax and Bid) and promoting cytochrome c release and apoptotic progression. Necroptosis is an alternative mode of regulated cell death mimicking features of apoptosis and necrosis [17]. Necroptosis describes the initial progression of cell death via apoptotic signalling pathways however, this eventually leads to secondary necrosis as evidenced by the display of characteristic necrosis phenotypes [17].

Understanding of cell death pathways has expanded rapidly in the last decades owing to great advances in chemical biology, pathway analysis and cell death research. Further, the evolution of technology has made it possible to assess such biomolecular changes with routine bench-top experiments and high-throughput screening assays [18].

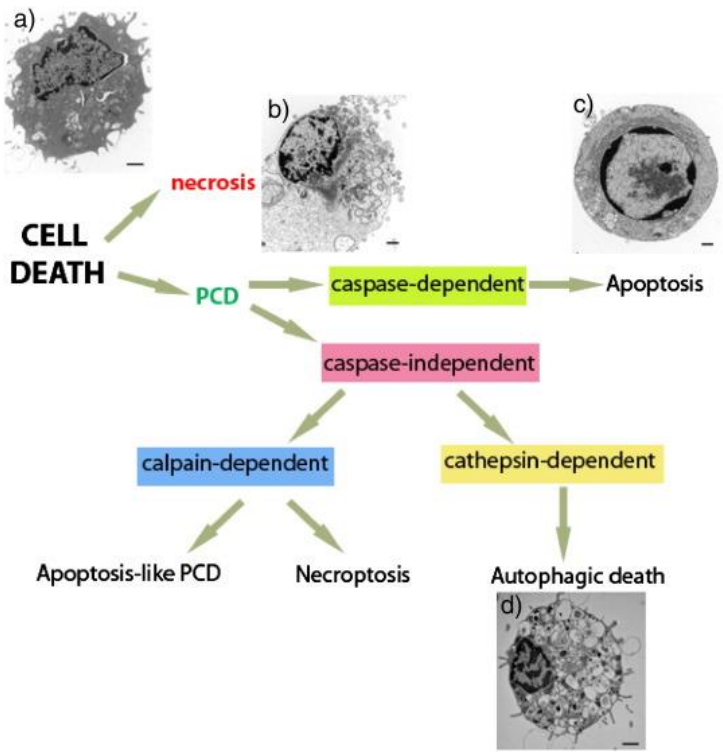

Figure 1.2. Types of cell death and their morphological hallmarks. Diagrammatic classification of different types of cell death. PCD: programmed cell death. Morphological features of a) a healthy cell, b) a necrotic cell, c) an apoptotic cell and d) an autophagic cell. Adapted from [19].

Previously, it was thought that multiple signalling pathways independently control different types of cell death (Fig. 1.2). It is now known that there is cross-talk between the different signalling pathways and that they can operate in parallel in cells in response to stress [19,20]. Several death initiator and effector molecules, signalling pathways and subcellular sites have been identified as key mediators in both processes, either by constituting common modules or alternatively by functioning as a switch allowing cells to decide which route to take,

depending on the specific situation [19]. For example, studies have shown that Bcl-2, which is an important regulator of apoptosis, also plays a key role in the autophagy pathway [21].

One of the pivotal features of cell death that the scientific community is attempting to dissect is the point of no return along these nuanced pathways [14]. There are both reversible and irreversible points along each cell death signalling pathway and determining where those transition points lie is of great importance from the standpoint of trying to intervene in the process. Regardless of the type of cell death, once the cell is past the point of no return, death cannot be prevented.

Of the four major types of cell death, autophagy has the highest survival superiority, followed by apoptosis, with necrosis having the lowest survival superiority [14]. In apoptosis, there are several mechanisms in which allows cells to escape apoptotic signals. Given its potential role in many diseases, various studies have been undertaken to develop therapeutic agents targeting autophagy and apoptosis [22]. However, the field faces major challenges because these dynamic processes are difficult to measure and quantify. For example, the accumulation of autophagosomes will not necessarily result in the increase in autophagy by itself [22]. If the three types of cell death are ranked according to their survival superiority, autophagy and apoptosis would be ranked higher than necroptosis (programmed necrosis) and necrosis (Fig. 1.3).

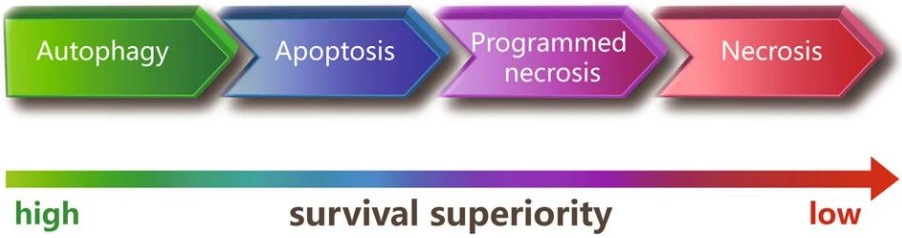

Figure 1.3. Survival superiority among the different types of cell death. Taken from [14].

1.2.1 Apoptosis in the bioreactor

Due to advantages in the production of complex proteins and their manufacturing adaptability CHO-derived cell lines are the preferred host expression systems for production of therapeutic proteins [23]. An estimated 35% of recombinant proteins that are currently approved for human therapeutic use are produced in CHO cells [5]. Apoptosis is reported to be responsible for up to 80% of cell deaths in CHO cell cultures in industrial bioreactors [5] which is not ideal as optimal bioprocessing requires a high titre producing cell culture with minimal apoptotic stress. Thus, monitoring and controlling apoptosis and its mechanism of action is essential for enhancing culture longevity and productivities.

Surprisingly, most mammalian cells can escape late stage apoptosis if cell death stimulus is removed [24]. Partially deformed cells with obvious apoptotic morphologies can repair themselves after passing important checkpoints, including cytochrome c release, caspase activation, DNA damage, nuclear condensation and fragmentation [24]. Hence, the detection of apoptosis at its earliest stages will enable faster interventions to rescue the culture and enhance culture longevity and productivity.

Apoptosis is an important and coordinated form of cell death observed under a variety of physiological and pathological conditions. Apoptosis can be triggered by a diverse array of both internal and external stimuli, all of which involve the activation of a group of cysteine proteases called "caspases" and a complex cascade of events (**Fig. 1.4**) resulting in systematic cell death [25].

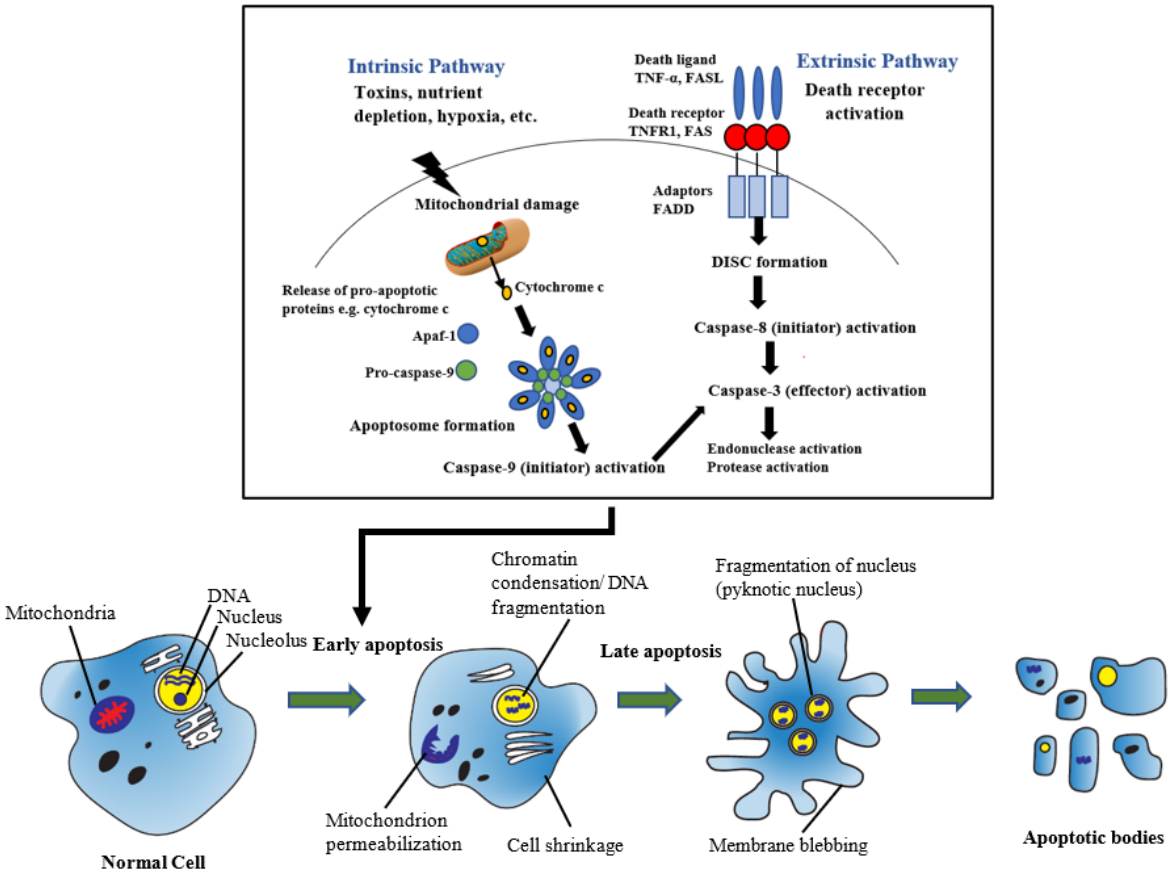

Figure 1.4. Illustration of apoptotic events. Two main pathways of apoptosis are the intrinsic and extrinsic pathways (above). Each pathway activates its own initiator caspase (8, 9) which will in turn activate effector caspase-3. The cascade of molecular events results in characteristic cytomorphological changes (below). These can be viewed on a whole-cell scale using microscopy, and on a molecular scale using biochemical assays.

The two pathways that lead to the activation of caspases, the extrinsic death receptor pathway and the intrinsic mitochondrial pathway have been studied extensively [7,12,26]. The extrinsic

pathway is initiated when ligand associate with their cognate trans-membrane death receptors of the tumour necrosis factor receptor (TNFR) family, activating caspase-8 and subsequently caspase-3 [26]. The intrinsic pathway is triggered by various stresses that result in mitochondrial damage and the release of cytochrome c and other proteins from the mitochondria into the cytosol, activating caspase-9 and subsequently caspase-3 [7].

The precursor Procaspase-9 is the inactive form of caspase-9. It contains four domains: caspase recruitment domain (CARD), large subunit (p35) , small subunit (p12) and a linker region. CARD is involved in interactions with Apoptotic protease activating factor 1 (Apaf-1). Large subunit contains the active site cysteine and is involved in substrate cleavage. Small subunit assists in the structural integrity of the enzyme and the linker region connects the large and small subunits. The mature caspase-9 is a heterodimer composed of: one large subunit (p35, approximately 35 kDa), one small subunit (p12, approximately 12 kDa). These subunits are generated from the cleavage of procaspase-9.

Figure 1.4 shows the activation process. Upon apoptotic signalling, cytochrome c is released from mitochondria and binds to Apaf-1. This triggers Apaf-1 to oligomerize into a heptameric structure called the apoptosome. Procaspase-9 binds to the apoptosome via its CARD domain. Within the apoptosome, procaspase-9 undergoes autocatalytic cleavage. The linker region is cleaved, resulting in the formation of the active enzyme, caspase-9.

The initiator and effector caspases are particularly good targets for detecting apoptosis in cells. These ubiquitous enzymes exist as inactive zymogens in cells and are cleaved before forming active heterotetramers that drive apoptotic events. Caspases with long pro-domains such as caspase-2, -8 and -9 act upstream as initiating caspases, these activate effector caspases through proteolytic cleavage and as a result their catalytic activity is enhanced by several orders of magnitude [27]. Caspase-3, -6, and -7 are effectors have shorter pro-domains than initiators and act by activating cytoplasmic endonucleases and proteases [28]. These degrade nuclear material and cytoskeletal protein, respectively, leading to characteristic morphological changes such as blebbing, fragmented nuclei, and eventually apoptotic body formation. These are hallmarks of late-stage apoptosis [29].

Proteomic studies demonstrated that both extrinsic and intrinsic pathways play important roles in the apoptotic cell death in batch and fed-batch cultures [7]. The intrinsic mitochondrial pathway is believed to be the most relevant apoptotic driver in non-induced (without pro-apoptotic agents) CHO cell cultures, evidenced by data showing over 70% of the culture expressing active caspase-9 compared to only 15% expression of caspase-8 and caspase-3 [30]. Although death receptor-mediated cell death in some cell lines might engage a crosstalk with the mitochondrial pathway, a dominant expression of caspase-9 most likely corresponds to the stresses exerted on the mitochondria or the endoplasmic reticulum [30]. This can be directly linked to the operating conditions of a bioreactor rendering it important in bioprocessing as it can be triggered by nutrient limitation, temperature or pH shifts, high osmolality etc. Moreover, expression of recombinant protein in cell cultures can overload the endoplasmic reticulum folding system and lead to endoplasmic reticulum apoptotic cell death.

1.3 Methods of detecting apoptosis

As previously mentioned, during sever and sustainable stress, the cells are led to their death by one of the two mechanisms; passive cell death (necrosis) and programmed cell death (apoptosis and autophagy). The leading cause of cell death is apoptosis,[5]. Consequently, the analysis of apoptosis is of great interest from a mammalian cell bioprocessing perspective. An overview of the most common methods used to detect apoptosis is provided below.

The presence of apoptosis was initially established with morphological techniques such as electron microscopy, light microscopy and flow cytometric detection [28,31,32]. As the biochemical and cell signalling events involved in the apoptotic cascade have been revealed, new tools for the analysis of apoptosis have emerged. Table 1.1 shows the key morphological and biochemical characteristics and the detection methods associated with these methods.

Table 1.1. The main types of cell death, morphological and molecular characteristics of cells and the methods used for its detection.

	Morphological features	Morphological and biochemical features
Morphological and molecular characteristics of apoptosis	1. Condensation of nucleus and nuclear chromatin. 2. Nuclear fragmentation (karyohexis) 3. Shrinkage of the cell 4. Condensation of the cytoplasm 5. Formation of Apoptotic bodies	1. Phosphatidylserine (PS) exposure 2. DNA fragmentation 3. Chromatin condensation 4. Mitochondrial membrane permeabilization (Cytochrome c release 5. Activation of proapoptotic Bcl-2 proteins 6. Activation of caspases

Methods of apoptosis detection successfully used in cited research	1 – 5. Microscopic methods/Fluorescence activated cell sorting (FACS) [33] 1 – 5. Scanning electron microscopy (SEM) [34] 1 – 5. Transmission electron microscopy (TEM) [34]. 1 and 2. DNA dyes- Hoechst, 4′,6-diamidino-2-phenylindole (DAPI) [35], Ethidium bromide, Propidium iodide 3. Exclusion dyes – Trypan Blue, eosin 4. Organelle dyes - Rhodamine 123 [33]	1. Fluorescence microscopy/FACS - Annexin V viability assay [36] 2. Polymerase chain reaction (PCR) [37,38] 2. a) TUNEL assay [33,39] 2. b) Electron microscopy [34] 3. Microscopy/FACS – DAPI staining [35] 4. Fluorescence microscopy [40] 5. Mass spectroscopy [41] 6. Colorimetric/fluorescence caspase activity assays [42]

1.3.1 Study of cell morphology in apoptosis

Traditionally, electron microscopy was considered the "gold standard" for the identification of apoptotic cells [43]. In 1972, Kerr et al.[13] established the characteristic ultrastructural features of apoptosis using transmission electron microscopy. These features include 1) cytoplasmic and nuclear condensation, 2) nuclear fragmentation, 3) morphological appearance of cytoplasmic organelles. TEM allows simultaneous identification of cells undergoing apoptosis and the cell type. However, this technique is no longer routinely used as an apoptotic assay due to the cost associated with performing electron microscopy, the specialized equipment, the time consuming nature of the process and the requirement for technical expertise [34].

In more recent years, evaluation of cells and tissues for apoptosis has evolved towards staining for light microscopic and flow cytometric analysis. Morphological changes of

apoptosis are characterized by the shrinkage of cells, loss of cell–cell contacts, aggregation of chromatin into dense, often crescent-shaped masses under the nuclear membrane, features of which can be structurally recognised with light microscopy (Fig. 1.5). However, the light microscopy technique is prone to human errors, heterologous cell states in different regions of the bioreactor can result in different conclusions, and image analysis can be challenging to perform for high density cultures and suspension cultures.

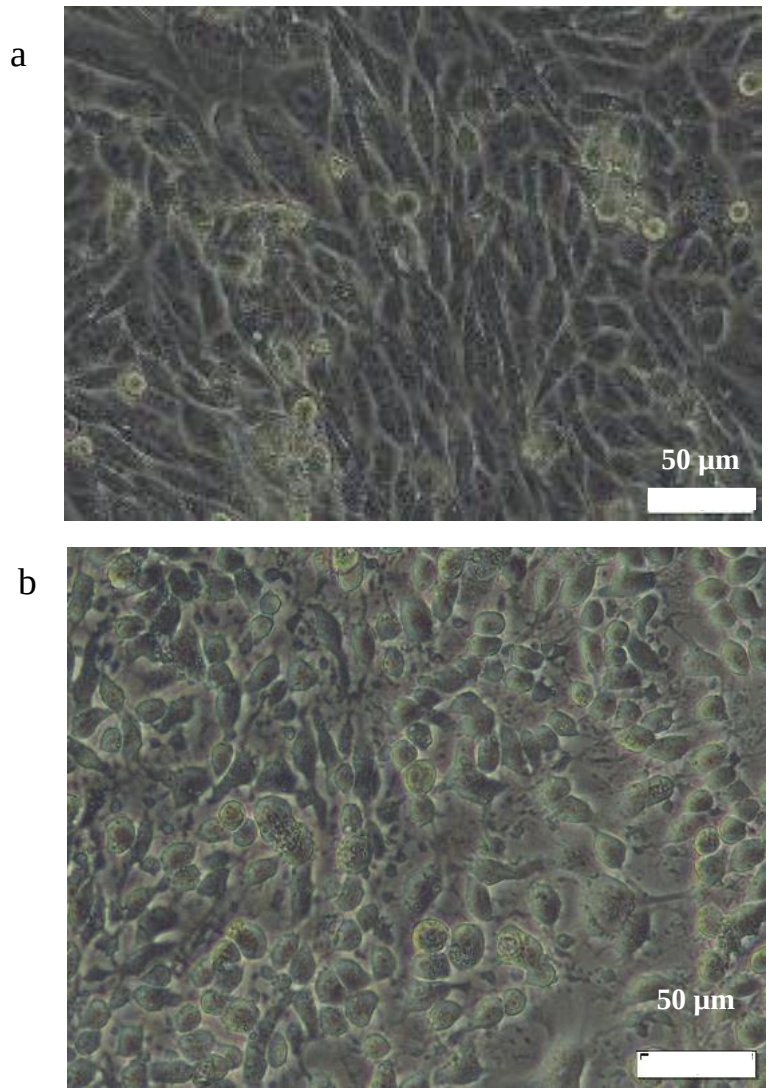

Figure 1.5. (a) Bright field microscope images of healthy CHO-K1 cell incubated for 6 hours at 37ºC. (b) Images of CHO-K1 cell treated with 1 µM staurosporine for 6 hours at 37ºC.

Useful information on cell health can be obtained by determining the viability of cultivated cells [41]. This is performed by the assessing the integrity of the cellular membrane by the dye exclusion test. Live cells with intact cell membranes exclude certain dyes such as trypan blue, whilst dead cells are stained by these dyes. The trypan blue exclusion assay is a standard, inexpensive and fast method for the assessment of cell viability [44]. However, the loss of outer membrane integrity signals the late stages of cell death. Whereas earlier signs of apoptosis such as cell shrinkage and nuclear condensation is not necessarily seen by this method. Organelle staining in live cells can help researchers to confirm the identity of specific proteins or targets within the cells and provide a better understanding of the cellular process. Rhodamine 123 is a cell-permeant, green-fluorescent dye that is readily sequestered by active mitochondria without cytotoxic effects [33]. This dye has been used to assay for mitochondria membrane potential in populations of apoptotic cells [33]. Early detection of cellular stress i.e. at the onset of apoptosis, using signals from within the cultured cells would offer predictive power and be much preferred.

.

1.3.2 Biochemical methods of apoptosis detection

Biochemical detection, which refers to the detection of biomarkers related to the molecular mechanism of apoptosis have been increasingly employed in the past decade. Many researchers combine morphological and biochemical changes to make the identification of apoptosis more objective and quantitative [45]. Flow cytometry, nucleic assay kits, biosensors, and enzymatic assays have been widely used for biomarker detection [46]. The primary biomarkers detected can be categorized into three levels: DNA, RNA, and proteins. The detection of these biomarkers can make apoptosis identification more accurate and at the

same time distinguish between different forms of cell death and provide insights on the specific regulatory pathways involved.

For quantification of messenger RNA (mRNA) and circulating free DNA (cfDNA), quantitative polymerase chain reaction (qPCR) is a useful and convenient technique. It has been widely applied in cell death studies to quantify the abundance and expression of taxonomic and functional gene markers in a given sample. Multiplexing of PCR expands its detection capability as more than one target gene is simultaneously amplified and detected. For example, Yu *et al*. customised a PCR array with 53 genes, including several important apoptosis-related genes involved in Alzheimer's disease [37]. Expression of certain genes such as NFκB1 were significantly increased, whilst some well-known apoptosis genes, such as the caspases, Bcl-2 did not show changes in expression levels [37]. One major disadvantage of qPCR-based approaches is the difficulty of extracting intact mRNA from a sample, as RNA is a labile molecule with a short half-life. Other variables such as, contamination, DNA polymerase error rate, the quality of the primers and quantification of the standard curve template can limit the benefits of its use in comparative studies.

Various signature proteins involved in apoptosis have been reported and researchers make use of these proteins in cell death assays. Depending on where the content exists and how the content is extracted, the molecular biomarkers used in regulated cell death (RCD) detection are divided into three types: cell surface markers acting at the plasma membrane (e.g., Phosphatidylserine (PS) [47]), intracellular markers (e.g., Bcl-2, caspases [30]), and soluble extracellular markers released from the cell (e.g., lactate dehydrogenase [48]).

For protein detection, western blots are regarded as a classic technique. The western blot allows for specific identification and characterization of proteins, in particular to detect specific proteins involved in the apoptotic process. This method uses specific antibodies to target the proteins of interests and protein concentration can be quantified using fluorescent agents. For example, the expression and phosphorylation status of members of the Bcl-2 protein family have been analysed by western blotting with specific antibodies. The detection of the phosphorylation of Bcl-xL at serine residue 62 is indicative of activation of the intrinsic apoptotic pathway [49].

Another antibody-based approach for the detection of protein biomarkers is the enzyme-linked immunosorbent assay (ELISA). The ELISA is a sensitive, cost-effective and practical option for the detection and quantitative analysis of apoptosis-related proteins such as caspase-3/7 [45]. The high specificity and sensitivity are a result of the antigen-antibody interaction. There are still some constraints that cause concern, such as antibody instability, labour-intensive procedure and the high possibility of false positives due to insufficient blocking of surface.

Mass spectrometry is an analytical technique in which samples are ionized into charge molecules and the mass-to-charge ratio of one or more molecules can be measured [50]. In recent years matrix assisted laser desorption ionization-time of flight mass spectrometry (MALDI-TOF MS) has emerged as a potential tool for cell identification and diagnosis [50]. MALDI offers the ability to generate ions from intact molecules without fragmentation of the analyte. MALDI-TOS MS has been reported for several purposes including microbial identification, detection of water-borne pathogens and detection of antibiotic resistance etc [51].

This technique requires small sample volume, minimal sample preparation and can be automated readily [50]. The main disadvantages include the high initial cost of the MALDI-TOF equipment and its inability to distinguish between phyletically related (genetically similar) microorganisms [51].

Over the last two decades, there has been a significant increase in apoptosis studies and the discovery of novel biomarkers. Additionally, incredible improvements have been made in the detection methods such as sensitivity, detection limit, selectivity, ease of use and cost. The potential application of biosensors in apoptosis detection will be addressed below.

1.4 Biosensors

The term "biosensor" refers to an analytical device involving biological sensing element. They are utilised in a wide range of application areas, including, drug discovery, disease diagnosis, biomedicine, food safety and processing and environmental monitoring [52]. The purpose of these analytical devices is to rapidly provide accurate and reliable information about an analyte of interest.

Generally, biosensors are composed of three main components, as depicted in **Figure 1.6**. These are a biological recognition element, physicochemical detector or transducer and a signal processing system [53]. Biological recognition elements are used to interact with the analyte of interest to generate a measureable change. Recognition elements commonly include materials such as antibodies, aptamers, nucleic acids, cell receptors, enzymes, organelles and microorganisms. This interaction between recognition elements and analyte is

then transformed to an electrical or optical signal via the transducer. The signal processing system modifies (usually including amplification) and analyses the signal to produce a measurable output signal [54].

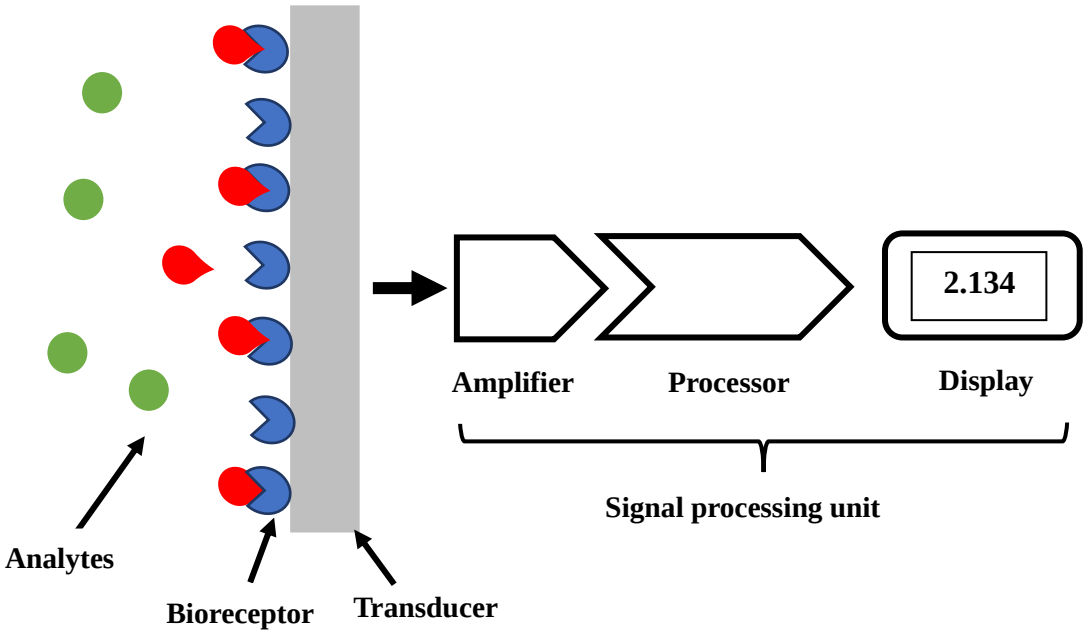

Figure 1.6. Basic schematic of a biosensor.

1.4.1 Important characteristics of biosensors

Several important performance characteristics must be considered when a biosensor is designed.

Sensitivity is the relationship between the change in analyte concentration and the intensity of the signal generated from the transducer.

Selectivity refers to the ability of the biosensor to selectively bind to only the target analyte, in the presence of other molecules.

Stability This feature determines the ability of the biosensor device to maintain its sensing performance over time even under external stress. These can be in the form of temperature, humidity or other environmental conditions. Such external factors can lead to inaccuracies in the output signal during measurement, thereby affecting the accuracy and precision of the device.

Limit of Detection The minimum amount of analyte that can be detected, typically defined as when signal is greater than three standard deviation of the control.

Limit of Quantification The signal is greater than ten times the standard deviation of the control.

Reproducibility refers to the ability of the biosensor device to produce replicable results in multiple experimental runs.

Precision is a measure of how close a series of measurements are to one another. Precise measurements are highly reproducible, even if measurements are not close to the correct value.

Accuracy is a measure of how close a measurement is to the correct value.

Response time determines the time it takes for the biosensor to generate a signal following the biorecognition event.

1.5 Classification of biosensors

Biosensors can be classified according to their biological receptors or transducer elements. Figure 1.7 displays a flowchart showing the different types of biosensors based on their biological receptors and transducer elements. Some of the biosensors shown in the figure will be discussed further in subsequent sections.

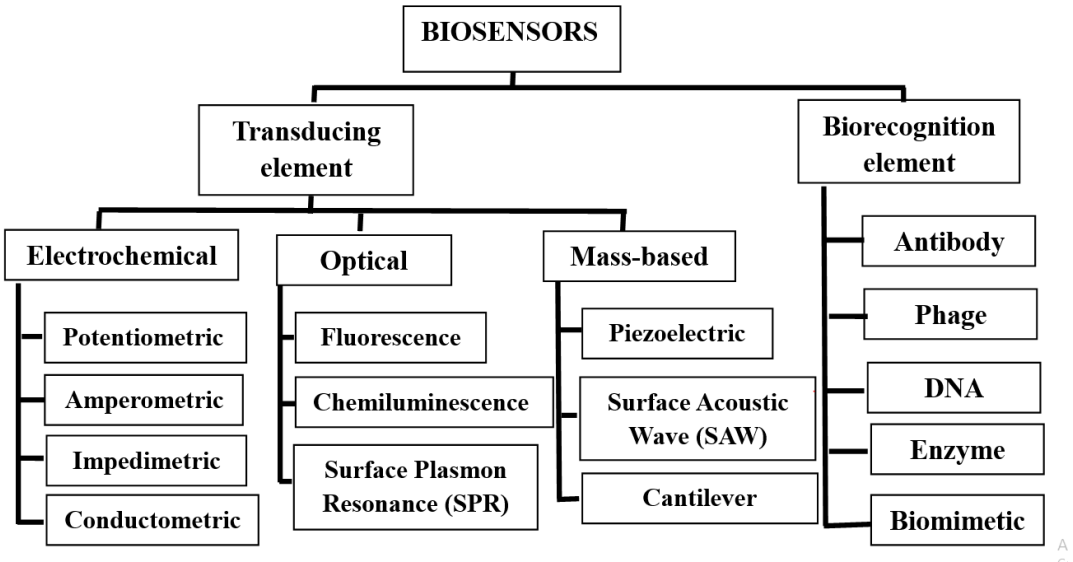

Figure 1.7. Flow chart illustrating the various types of biosensors grouped based on their transducing elements and biological recognition elements. Adapted from Tetyana [54].

1.5.1 Bioreceptors

The most reported type of biosensor uses an enzyme as the bioreceptor and is particularly suitable for monitoring rapid changes in metabolite levels in real-time. The enzymatic glucose biosensors are the most common devices commercially available and have been widely studied over many decades. The glucose biosensor, which was developed by Clark

and Lyons [55], is made up of glucose oxidase immobilized within a dialysis membrane which is integrated inside oxygen electrodes. The measured compound here is hydrogen peroxide, the concentration of which changes with enzymatic activity. The basic concept of the glucose biosensor is based on the fact that glucose oxidase catalyzes the oxidation of glucose producing gluconic acid and hydrogen peroxide [55]. The hydrogen peroxide is oxidized at the platinum anode, and this electron flow between the anode and cathode generates a current which is proportional to the number of glucose molecules in the sample [55]. The main advantages of enzymatic biosensors are the prolonged use and reusability due to the fact that enzymes cannot be consumed. However, the main drawback is that they are only suitable for a limited number of analytes [52].

DNA biosensors, which used nucleic acids at biorecognition elements, detect proteins and non-macromolecular compounds that interact with certain DNA fragments known as DNA probes or DNA primers [54]. These receptors form stable hydrogen bonds with their complementary nucleic acid strands. The functionality, selectivity and sensitivity of the capture oligonucleotides strongly depend on the design of the capture probe [56]. Nucleic acid-based biosensors are commonly used to detect a wide range of targets containing DNA, such as bacteria and viruses. However, their applications are somewhat limited due to the nucleic acids being prone to environmental stresses such as temperature, pH, enzymatic cleavage and these methods require additional DNA extractions steps [57].

1.5.2 Antibody based sensors

Antibody-based sensors (Immunosensors) are sensors that utilize antibodies as the recognition component. The antibody, also known as immunoglobulin, has a Y shape conformation with paratopes on each tip that can specifically recognize the epitopes on an antigen. Therefore, this type of biosensor utilizes the antibody-antigen interaction to bind specific targets, enabling antigen concentration quantification. Antibody-based biosensors are extremely adaptable, and can be tailored to detect a wide range of analytes. There are thousands of examples of antibody-based biosensors in the literature spanning a wide range of applications. For example, Kaushik's group developed an immunosensing chip for the diagnosis of Zika-virus infection [58]. The device has ZIKV-envelop protein antibody immobilized onto the gold electrode using a self-assembled monolayer to capture the Zika virus specifically with high affinity. The sensing chip exhibited a detection limit of 10 pM with high sensitivity [58]. This sensor exhibits the potential for use in rapid disease diagnosis and therapy monitoring as a point-of-care device [58]. Tuteja's group developed a label-free immunosensor based on electrochemical impedance spectroscopy for the sensitive detection of a cardiac biomarker, myoglobin. They achieved a limit of detection of 0.01 ng/mL which is comparable to standard ELISA techniques[59]. Epidermal growth factor receptor 2 (ErbB2), a key breast cancer biomarker, was measured using an antibody-based biosensor based on high-density silicon microneedle arrays [60]. The sensor demonstrated a linear range from 50 to 250 ng/mL and a detection limit of 25 ng/mL [60]. A wide range of methods, both classical and modern, have been demonstrated. Antibodies are able meet most of the requirements imposed on biorecognition molecules, including high specificity and stability. For this reason, many biosensors utilise antibodies.

Antibody-based biosensors can be classified as (i) labelled and (ii) non-labelled. Direct immunosensors, in other words label free immunosensors, are capable of detecting the physical or chemical changes arising directly from the immune antigen-antibody complex formation without needing to label.

Due to the fact that biological analytes are often hard to detect purely on basis of their intrinsic physical properties, biosensors often require labels such as enzymes and fluorescent or radioactive molecules attached to a analyte. In the case of a labelled antibody-based sensors, a "tag" or "label" is used to detect a particular biorecognition event and hence analyte concentration. Fluorescence [61–65], chemiluminescence [66–69]and radioactive [70,71] are three popular label types for biosensor applications. The principles behind labelled biosensors is that a secondary antibody with a labelled reagent, e.g. fluorophores, are covalently bound to an antibody. The capture antibody binds to antigens, and the secondary labelled antibody binds to the antigen generating a measurable output signal. One advantage of labelled biosensors is the enhanced sensitivity due to the indirect measurement of the label rather than the analyte. However, the drawbacks of labelling a biomolecule include: loss of sample or functionality during the labelling process, fluorescent probes are prone to photobleaching, sensitivity to the environmental factors such as pH and overall, it is more complicated and time consuming [70].

Non-labelled immunosensors are constructed to specifically determine the antigen–antibody complex by estimating the physical changes caused by the development of the complex. They utilize physical properties of the analytes, such as molecular weight, size, charge, electrical impedance, dielectric permittivity or refractive index, to detect their presence in the sample. For example, in the context of a label-free electrochemical immunosensor, the steric

hindrance produced from the formation of immunocomplexes can prevent electrons from reaching the surface of the electrode and generating an increase in resistance, which can be quantified for a given antigen concentration [72]. The main advantage of label-free biosensors is that the biological interaction can be directly measured and information can be gathered on the selectivity and affinity. The label-free detection field as a whole has been undergoing great progress in recent years.

In this PhD study, a simple adsorption method was used to immobilise antibody on ZnO/CuO surfaces through strong electrostatic interactions. This biosensor utilises label-free, non-faradaic impedimetric sensing approaches. This leads to the advantages of less sample preparation and no requirement for a redox probe (further discussed in chapter 2).

1.5.3 Immobilization techniques in biosensors

To design the biorecognition part of a biosensor, immobilization of biological elements on the surface of the transducer is necessary. The selection of the appropriate immobilization technique is an important aspect of sensor preparation. This is because the biorecognition element/molecule must be able to preserve their structure, function, and biological activity during biosensor use. For antibody-based biosensors, assay sensitivity is dependent on immobilization of the capture antibodies onto a solid support with a sufficient surface density, a conformation that is representative of their native, solution-phase state, and an orientation that maximizes their antigen capture potential [73].

There are two main approaches to antibody immobilisation: physical adsorption and covalent immobilisation. Physical adsorption of antibodies onto sensor surface typically occurs via

hydrophobic and electrostatic interactions [74]. While this is the simplest method for the immobilisation of antibodies to solid supports, it is uncontrollable as the antibodies are immobilised in a randomly oriented manner. Random orientation can lead to antibody instability and is typically associated with poor binding and denaturation [73].

Covalent immobilisation of the antibody involves the formation of covalent bonds through the chemical reactions between functional groups on the antibody and the surface. One of the most popular methods is the N-Ethyl-N'-(3-dimethylamino-propyl) carbodiimide hydrochloride (EDC)/N-hydroxysuccinimide (NHS) coupling reaction. Amine and carboxyl groups are ubiquitous throughout an antibody's structure and are commonly found on the antibody's surface due to their polar nature [75]. Amine and carboxyl coupling is achieved with carbodiimide chemistry (such as EDC) combined with succinimidyl esters (such as NHS) [75]. Due to the prevalence of amino and carboxyl group on the antibody, site-directed covalent antibody immobilization targeting these groups is difficult and unfavourable random orientation can occur. Another disadvantage of these crosslinkers is that the secondary antibodies can bind to the vacant binding sites on the crosslinkers, which can lead to higher background signal and nonspecific binding. Ideally, antibodies should be immobilized in their native form, without the need for additional functional groups, oriented in a way such that antigen binding sites are exposed to maximise antigen binding.

In applications where electrical properties on the sensor surface are important variables, the additional distance introduced by SAMs and crosslinkers may push the antibody-antigen interaction outside of the electrical double layer (discussed in chapter 2), thus resulting in a decrease in sensor performance [76].

Despite a potential loss in antigen binding sites, the simple physical adsorption immobilisation method has been used many times in the biosensor applications. Justino *et al.* [77] immobilised antibodies on carbon nanotubes, and demonstrated excellent sensor performance, with a limit of detection of 0.1 ng/mL for C reactive protein (CRP) with only 1 µg of anti-CRP antibodies. Another group compared the performance of the random and orientated antibody for the detection of prostate specific antigen [78]. With the end-on immobilised antibody, a detection limit of 10 pg/mL was achieved, which was 100 times lower than that of detection limit for random immobilisation (1 ng/mL) [78].

A way of overcoming the challenges associated with non-covalent immobilisation is to introduce nanomaterials such as zinc oxide (ZnO) and copper oxide (CuO) to the immobilisation procedure. For example, many glucose biosensors use ZnO nanorod to bind glucose oxidase enzyme (GOD) [79,80]. One advantage of ZnO nanorods is the high surface-to-volume ratio which provides a large specific surface area for the GOD adsorption, and thus comparatively more active sites for catalysis. Utilization of metal oxide nanomaterials in antibody-based biosensors have also been widely reported. For example, Dominguez *et al.* developed a strategy for antibody immobilisation on ZnO thin film transistors and they demonstrated antibody functionality was maintained [81]. Safavipour *et al.* [82] developed a aptamer-based sensor for the detection of breast cancer cell, by immobilising aptamers on titanium dioxide (TiO_2) nanotubes. TiO_2 nanomaterials have attracted much attention thanks to their high surface to volume ratio, good charge electric transfer and biocompatibility [82].

The immobilisation strategy in this study was to use simple physical adsorption method to attach antibodies on ZnO/CuO surfaces via electrostatic forces. ZnO provide an important role as the active sites where biological interactions occur. This allows the antibody/antigen interaction to occur as close to the sensor surface as possible. This approach was chosen over complex covalent immobilisation methods in the final protocol due to the simplicity and ease of use. Covalent immobilisation approaches such as, protein G based methods were explored in the preliminary experiments and performances were compared.

1.5.4. Substrates

Successful attachment of antibody to the sensor surface is strongly influenced by the selection of substrate. This is especially important for physical adsorption techniques. Important attributes of a sensor surface are that it should be biocompatible and the chemical constituents of the material should not interfere with the attached protein.

Physical adsorption is the simplest method for the immobilization of antibodies to immunoassay solid supports, such as microtiter plates. Polymers such as polystyrene, polypropylene, polyethylene, and cyclic olefin copolymer blends are often used in microtiter plates for their increased hydrophilicity [73]. The hydrophilicity can be increased further through surface medication methods, such as plasma treatment, self-assembled monolayers and siliconization [73]. The increase in hydrophilicity can increase antibody binding (density) and decrease the amount of denatured protein [73]. Overall, polymer substrates are commonly used as the immobilisation platform for immunoassays as they provide a cheap, stable, reproducible substrate that is easy to manufacture [73].

Glass is another commonly used substrate as it possesses several advantages including: biocompatibility, optical transparency, good binding properties through charges on the surface, high temperature tolerance and also it is a versatile material [73]. Glass substrates are commonly used in optical sensors. Nath *et al.*[83] developed a surface plasmon resonance (SPR) biosensor, by the chemisorption of gold nanoparticles on glass substrate. They demonstrated the surface density of immobilised particles on glass increases linearly with the nanoparticle's concentration [83]. Glass substrate has also been used in fluorescence imaging applications. Tanak *et al.* [84] used fluorescent probes to quantify the amount of crosslinker binding on the glass substrate. The major disadvantage of glass compared to plastic materials is that the substrates are rigid and fragile.

Paper is a versatile, flexible, porous, and low-cost substrate that is utilized in the fabrication of diagnostic devices and biosensors. Nitrocellulose (NC) membrane is a common polymer use for lateral flow strips and membrane-based biosensors mainly because of its high porosity, large pore sizes (the range is 0.45 – 15 μm), fast flow rate, low surface area and high mechanical strength [85]. The microstructure of porous membranes offers larger specific surface area and better adsorption ability compared to 2D surfaces.

There are two views on the adsorption principle of NC membrane. Some researchers have reported that the surface of the NC membrane contains hydrophobic regions of protein and carbon-containing nitrocellulose, which can facilitate the binding of biomolecules through hydrophobic interactions [85]. Others researchers showed that biomolecules were directly

attracted to the surface of NC membrane through electrostatic interactions between biomolecules and nitrate groups of the nitrocellulose [85].

Nitrocellulose membrane is the preferred paper-substrate for biosensor applications due to two of its properties: low flow rate and excellent biochemical molecular binding capacity. Low flow rate can delay the reaction time between chemical reagents and excellent molecular binding capacity can offer good immobilisation of biomolecules. Improvements in flow rates are offered by various membranes, for example, HF (High Flow) 180 and HF 135 NC membranes used to prepare nucleic acid lateral flow assays (LFA) [86]and protein based LFA [85]. Several modification technologies have been used to further enhance the sensitivity of LFAs. For instance, cellulose nanofiber has been used in NC membranes to increase porosity, reduce pore size and provide additional surface functional groups for enhanced binding capacity of biomolecules [87]. This method can improve the sensitivity of protein LFAs about 36% compared to conventional LFAs [87]. Another material used is chitosan, which has been shown to increase sensitivity of LFAs by up to 10-fold by increase porosity and binding capacity of proteins [88].

Recently, there has been an increase in interest in paper-based substrates in biosensor applications. The capacity for antibody attachment can be increased using 3D porous membrane materials instead of convention 2D surfaces by increasing the surface density of immobilised antibodies [89]. The modification of NC membrane with metal oxides has also been reported. Cao *et al.* [89] fabricated a nano-ZnO/CuO nitrocellulose membrane biosensor using a simple sonication technique. The sonication force assisted the loading of nanoparticles into the lower layer of the membrane. The addition of CuO nanoparticles in

nano-ZnO/CuO nitrocellulose membrane biosensors showed enhancement of performance on impedance spectroscopy [89].

The biosensor developed in this study is based on a non-faradaic impedimetric detection approach. Here, the biorecognition layer is built on top of a 2D glass substrate. The thin glass substrate is also impermeable to water which prevents the direct contact between the electrolyte solution and the electrode surface.

1.6 Biosensor categorisation based on their transduction element

The most commonly applied classification of biosensors is based on the type of transducer used in the sensor. These sensors are classified into three main categories, known as electrochemical biosensors, mass-based biosensors and optical-based biosensors. The working principles of each of the three biosensors are distinct and can be implemented in variety of applications. Below is a brief description of the different types of biosensors and their working mechanisms.

1.6.1 Electrochemical sensors

Electrochemical biosensors are the most widely investigated and commercially used. Their operation relies on the electrochemical properties of the analyte and transducer. In this biosensor, an electrochemical reaction occurs on the transducer surface between the bioreceptor and the analyte producing detectable changes in electrochemical signals, such as voltage, current, impedance, and capacitance [90]. **Figure 1.8** shows the schematic

representations of the main transduction principles: (a) amperometric, (b) potentiometric, (c) conductometric and (d) impedimetric biosensors.

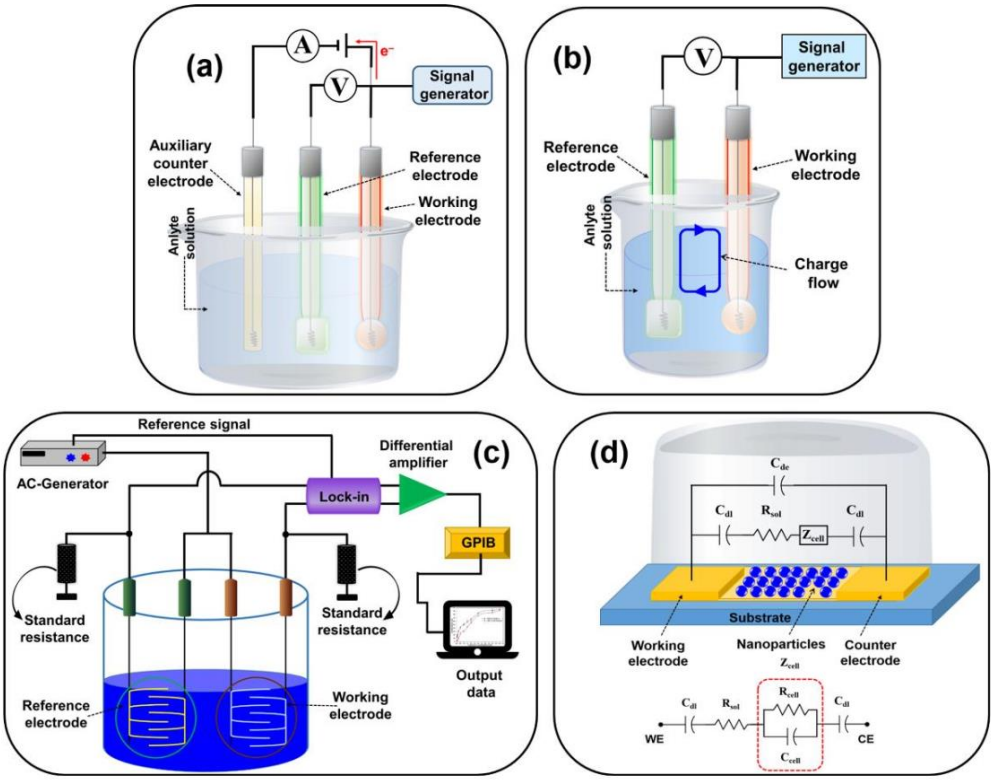

Figure 1.8. Schematic diagram of (a) amperometric/voltammetric, (b) potentiometric, (c) conductometric biosensors, and (d) impedimetric sensors (where C_{dl} = double layer capacitance, R_{sol} = solution resistance, C_{de} = electrode capacitance and Z_{cell} = impedance introduced by bound particles.) Taken from Naresh et al.[90].

(a) Amperometric biosensors measure the current change that result from oxidation or reduction of an electroactive species in a biochemical reaction. The simplest form of this is the Clark oxygen electrodes, where a current is produced in proportion to the oxygen concentration. This is measured by the reduction of oxygen at a platinum working electrode, with reference to a Ag/AgCl reference electrode at a constant potential [93]. The peak value of the current measured over a linear potential range is directly proportional to the bulk concentration of the analyte [92].

(b) Potentiometric biosensors measure the accumulation of charge potential at the working electrode compared to the reference electrode in an electrochemical cell under zero current. This provides information on the ion activity in an electrochemical reaction [91]. Thus, potentiometry has become the standard technique in the clinical analysis of ions, particularly the determination of the biologically relevant electrolytes in physiological fluids and in cells, such as Na^+, K^+, Ca^{2+}, and Cl^{-1} [92].

(c) Conductometric biosensors measure the change in conductance between the working and reference electrode induced by an electrochemical reaction (i.e. a change in solution conductivity). These are generally used to monitor metabolic processes in living biological systems [91].

(d) Voltammetric biosensors detects the analyte by varying a potential and then measuring the resulting current. There are many ways to vary the potential. Cyclic voltammetry is one of the most widely used forms and is useful to obtain information about redox potential and electrochemical reaction rates [94]. For example, increasing the concentration of reaction

specific enzymes at a given scan rate will result in a higher current compared to the non-catalysed reaction [94].

(e) Impedimetric biosensors measure the electrical impedance produced at the electrode/electrolyte interface when a small sinusoidal excitation signal is applied [90]. A low amplitude AC voltage is applied at the sensor surface and the magnitude and phase of the current response is measured as a function of frequency [90]. Impedance spectroscopy can be used monitor changes in electrical properties (e.g. capacitance) arising from biorecognition events at the electrode surface.

1.6.2 Optical sensors

In optical biosensors the interaction between bioreceptor and analyte generates an optical signal, which is correlated to the concentration of the analyte of interest. The observed optical signal is based on the measurement of photons involved in the process, rather than electrons, as in the afore mentioned techniques. The most common optical detections methods are based on the measurement of luminescence, fluorescence and absorbance. Optical sensors can be further classified into probing biosensors and reacting biosensors. Probing biosensors base their activity on the binding interaction between the analyte and the recognition element, which is determined by affinities [95]. Whereas, reacting biosensors rely on chemical processes, such as catalytic reactions, chemisorptions or formation of new bonds to generate optical changes [95].

Of all the optical biosensors, fluorescence-based detection is the most widely used method of detecting and quantifying biological compounds due to their ease of use, capacity to

screening multiple compounds in a single device and remote sensing capability. To detect analytes, fluorescent labelled antibody bind with analytes by a covalent interaction through any reactive group such as hydroxyl, carboxyl, amino, or sulfhydryl groups. If the analyte is present the fluorescence signal can be measured with the fluorescence detector. Fluorescence-based biosensors have been widely reported in the literature. For example, Zhang *et al.* [96] reported a fluorescent-based biosensor for the detection of caspase-3, they created a chimeric fluorescent protein substrate whose fluorescent function was only switched on by caspase-3 cleavage [96]. This chimeric protein enables real-time monitoring of apoptosis in individual cells within a population, reducing the need for sample damage and sophisticated techniques or instruments. [96]. The appearance of phosphatidylserine (PS) on the cell surface is one of the hallmarks of the early/intermediate stages of cell apoptosis [97]. A common method of detecting PS on a cell surface is to use the PS-binding protein annexin V, this protein is typically labelled with a fluorescent probe such as fluorescein [97]. The disadvantage of label-based biosensors is the additional complexity to the measurement process.

Absorbance-based biosensing techniques are simple, and the results can be easily observed by the naked eye, requiring no sophisticated instruments. Pan *et al.* [98] reported on a colorimetric assay for the detection of caspase-3 activity using gold nanoparticles (AuNPs). Following the cleavage of AuNP labelled caspase-3 specific substrate, the AuNP is released, which results in the aggregation of AuNPs [98]. This corresponds to a colour change from red to violet, which can be detected with a standard UV-Vis spectrophotometer [98]. Compared to the fluorescent techniques mentioned earlier, this colorimetric method is label-free and requires less processing stages.

SPR sensors detect changes in the refractive index near a sensor surface, which occurs when molecules bind to the surface. This detection is based on the phenomenon of surface plasmon resonance, which involves the excitation of surface plasmons—coherent electron oscillations—by incident light at the interface between a metal (typically gold) and a dielectric (e.g., a glass prism).

When light hits the metal film at a specific angle, it induces the surface plasmons, resulting in a reduction of reflected light intensity at that angle. This angle is sensitive to changes in the refractive index near the surface, allowing the sensor to detect biomolecular interactions in real-time without the need for labels or extensive sample preparation.

1.6.3 Mass-based biosensors

Mass-based biosensors or gravimetric biosensors are sensors that respond to a small change in the mass binding material, such as proteins or antibodies on the surface, producing a measurable signal [90]. Piezoelectric-based biosensors, e.g. the quartz crystal microbalance (QCM) are most commonly used for gravimetric transduction. Piezoelectric biosensors consist of crystals which are covered with a biorecognition layer. These crystals undergo elastic deformation when a current is applied at a specific frequency, also known as the resonant frequency. If an analyte is adsorbed or desorbed on the surface the crystal via biomolecular interaction, the resonant frequency changes and this indicates the occurrence of binding [99]. Tong *et al.* [100] demonstrated a piezoelectric biosensor using indium tin oxide as the transducer for the label-free, real time assessment of cell cytotoxicity. The developed device could accurately monitor the growth process of cells, with a linear range of 0.1×10^4 to 10×10^4 cells/mL [100]. QCM sensors consist of a thin disk of quartz crystal sandwiched between

two electrodes and the resonating frequency of the crystal changes in response to a change in mass at the surface due to analyte binding [90]. Hewa *et al.* [101] reported a QCM-based sensor modified with antibodies that target the matrix protein of influenza virus. Protein A layer was used to orientate the antibodies for maximal binding of antigens [101]. The resultant biosensor had a detection range of 10^3 – 10^7 PFU/mL and had higher sensitivity compared to the conventional diagnostic techniques, such as cell culture and ELISA [101]. The advantages of mass-based sensors include high sensitivity, label-free detection, and low cost operation [101]. However, the main drawback is that the measurement can be time consuming.

1.6.4 Impedimetric biosensors

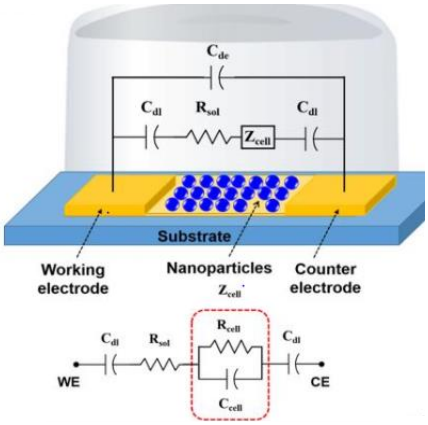

Figure 1.9. Schematic diagram of a typical impedimetric sensor and its equivalent circuit model. Taken from Naresh et al [90].

Electrical Impedance spectroscopy (EIS) is a commonly applied electrochemical technique used for the analysis of interfacial properties related to bio-recognition events occurring on an electrode surface. EIS can be used to explore mass-transfer, charge-transfer, and diffusion processes. Thus, it has the ability to monitor changes in the resistance and/or capacitance of

the electrochemical system. Impedance, Z, is a complex quantity composed of a real part and an imaginary part. The resistance, R, is used to represent its real part and reactance, X, is used to represent the imaginary part. In the Cartesian form, the impedance can be defined as:

$$Z = R + jX$$

The impedimetric measurement principles can be better understood with the help of appropriate equivalent circuits that fit to the sensor design and experimental dependencies. **Figure 1.9** highlights some of the circuit components described in common impedimetric measurement systems. EIS offers several advantages over the other electrochemical techniques including the fact that EIS is able to probe signal relaxations over a wide range of applied frequencies, from 1 Hz to 100 MHz, using commercially available potentiostats [102]. The EIS biosensors have gained increased interest in scientific research due to their facile manipulation, rapid response, ease of miniaturization and ability to detect low concentrations [102,103]. The following sections provide a brief introduction to the applications of faradaic and non-faradaic EIS. A more detailed overview of the EIS technique and the theory behind the proposed biosensor will be discussed in Chapter 2.

Previous studies have used standard faradaic methods to detect biomolecules, where the biorecognition molecules are immobilised directly onto the electrode surface [[104,105]]. Faradaic methods have been used to detect a wide range of analytes. Ohno et al. [106] reported a sensitive EIS-based biosensor for the detection of human immunoglobulin A (IgA). EIS measurements showed that the specific binding of IgA onto the immobilised anti-IgA give rise to a linear increase in the interfacial charge transfer resistance (R_{ct}) between the concentration range of 0.01 – 100 ng/mL [106]. *Xia et al.*[104] immobilised a biotinylated caspase-3 specific substrate on gold electrode surface. Once the substrate is cleaved by caspase-3, the

biotin tag is detached from the surface leading to a decrease in electron transfer resistance, achieving a detection limit of 1 pg/mL. Hung *et al.*[107] presented a EIS-based biosensor for the analysis of caspase-3 activity using screen-printed gold electrodes (SPGE) functionalised with caspase-3 specific peptides. The proteolytic activity of caspase-3 can be detected by apparent changes in charge transfer resistances [107]. The biosensors mentioned above [106,107] were faradaic sensors using ferro/ferricyanide ($[Fe(CN_6)]^{3-/4-}$) redox probes to allow for efficient heterogeneous charge transfer across electrodes.

Electrochemical impedance spectroscopy has also been used in the non-faradaic mode for biosensing applications. In the non-faradaic technique, the biological interaction between the surface receptor and analyte gives rise to dielectric changes at the electrode surface, which can be assessed with impedance spectroscopy. In contrast to faradaic EIS, non-faradaic impedance measurements can be done without the use of redox probes. And, the capacitance of the electrode–electrolyte interface can be considered as the main indicator of biomolecular interaction [108]. Lin *et al.* [109] developed a non-specific cell-based sensor and used non-faradaic EIS for the non-invasive time-course monitoring of the adhesion, growth and induced death of rat adrenal pheochromocytoma cells. The measured signals of non-Faradaic EIS are attributed to the insulating effects of cell membranes of cells that grow on or attach to the sensing surface [109]. The impedance was found to increase during cell growth, indicating increasing dominance of capacitance attributed shielding effects of the cell layer or coupling of the negatively charged cell membrane with the device [110]. The changes in the impedance can be associated with the morphological changes of cells and cell death was found to restore the initial impedance values [109]. Cao *et al.* [89,111] explored the application of non-faradaic impedance spectroscopy for the sensing of CRP in buffer, and these sensors were able to detect sub-ng/mL concentrations of CRP within ten minutes. The biosensor comprised of an

electrode, insulating layer and a biorecognition layer . Nanomaterials such as zinc oxide and copper oxide were deposited on the biorecognition layer to improve sensor sensitivity, similar to the methods used in this study. The application of this type of sensor for caspase detection and apoptosis monitoring in complex cell culture has not yet been investigated.

Both faradaic and non-faradaic EIS present relevant advantages as transduction methods over other types of transducers including low cost, low power requirement and high sensitivity with minimal hardware demand [108]. Despite being the less sensitive method of two, the non-faradaic method does not require the presence of redox couples, and, consequently, no reference electrode is necessary because no DC potential is required [108]. These features make this group of sensors more amenable to miniaturization and to online/real-time applications. In the non-faradaic method, the capacitance is generally the most important transducer term to interpret the recognition of the analyte. The capacitance can be measured through an insulating layer, as a result, the sensor surface can be decoupled from the electrodes. Thus, disposable sensor surfaces can be used to increase the lifetime of the sensor itself. It is for these reasons that a non-faradaic impedimetric approach was used in this research study.

Table 1.2 Advantages and disadvantages of different transducer types

Transducer type	Advantages	Disadvantages
Faradaic electrochemical (e.g. Amperometric/voltametric)	• High sensitivity and specificity. • Wide linear range. • Low cost and simple instrumentation.	• Susceptible to interference from other electroactive species. • Limited to analytes that can undergo redox reactions. • Potential for electrode fouling. • Often requires complex surface modification of electrodes.
Non-Faradaic Electrochemical (e.g. Electrical impedance spectroscopy in this thesis)	• Minimal interference from electroactive species. • Suitable for a broader range of analytes, including non-redox-active species. • Reduced risk of electrode fouling. • Typically simpler surface chemistry requirements.	• Generally lower sensitivity compared to Faradaic methods. • Often requires high-frequency measurements and sophisticated instrumentation. • Can be more susceptible to noise from capacitive or dielectric changes. • Limited to analytes that induce changes in dielectric properties.
Label-Free Optical (e.g. Surface plasmon resonance)	• Label-Free Detection. • Real-time monitoring of binding interactions. • High sensitivity and specificity. • The technique is non-destructive to the sample.	• High cost of SPR instruments. • Complex data interpretation. • Can be sensitive to changes in temperature, pH and other envoirnmental conditions. • Non-specific binding and fouling of the sensor surface can occur.
Piezoelectric	• Label-free detection. • High sensitivity as sensors are sensitive to changes in mass. • Real-time monitoring. • Sensitivity to environmental conditions. • Direct mass measurements.	• Sensitive to environmental conditions. • Surface fouling. • Calibration of the sensor can be complex and time-consuming. • Piezoelectric materials used in these sensors can degrade over time.

1.7 Performance comparison between biosensors and bioassays

Many of the established methods for the detection of protein biomarkers are based on antibody recognition. To date, the most widely used immunoassay for the detection of biomarkers is the enzyme-linked immunosorbent assay (ELISA). The sandwich ELISA is the most commonly used format. In a sandwich ELISA, the capture antibody is first immobilised on the surface of the well plate in order to facilitate the immobilisation of the antigen. The secondary detection antibody is conjugated with a molecule amenable for detection such as an enzyme or a fluorophore. ELISA-based methods exhibits high specificity and sensitivity due to the antibody-antigen interaction. However, there are several drawbacks to this method which prevents its use as a rapid diagnostic. Firstly, the method is labour intensive and expensive reagents are required [112]. Secondly, the method generally requires specialised laboratory equipment, long preparation times and large volumes of reagent [112]. Lastly, the need for labelling can lead to other problems including: loss of sample or functionality during the labelling process, fluorescent probes are prone to photobleaching, and sensitivity to pH changes [112]. As a consequence, there has been an increasing effort in the development of new biosensing techniques that can either avoid or solve some of the common drawbacks associated with ELISA-based techniques.

Table 1.3 shows a selection of biosensors based on their transduction methods, bioreceptors and antibody immobilisation methods. Key characteristics to consider when comparing the performances of different biosensors are their sensitivity, limits of detections and response time. As it can be seen from the table, the biosensors with the shortest response times are generally electrochemical sensors, particularly impedimetric sensors. The table also shows the detection limits across different sensing platforms, with electrochemical biosensors

exhibiting detection limits in the pg/mL to ng/mL range compared with detection limits in the µg/mL to mg/mL range for optical sensors. Another observation is the increasing prevalence of the use of metal oxides and nanoparticles in the electrochemical sensors, which in some cases is responsible for the enhanced sensitivity of these biosensors. Vabinna *et al.* [113] presented a highly sensitive, selective, and label-free electrochemical biosensor for cortisol detection using antibody-decorated ZnO nanoflakes. Anti-cab (antibody) loading and sensing performance were increased through the greater surface charge density and favourable catalytic activity of the ZnO [113]. The performance of the biosensor was evaluated on human saliva samples and measured a low detection limit of 1 pM, which is 100 times greater than conventional ELISA [113]. The benefits of nanomaterials have also been realised in non-faradaic impedimetric sensors. Cao *et al.* [89] presented a nano-ZnO/CuO membrane-based biosensor for the detection of CRP. The addition of CuO to the membrane resulted in a increase in detection limit from 27 pg/mL to 16 pg/mL [89]. The role of nanomaterials and nanoparticles in biosensors will be explored in the following sections.

Table 1.3 A selection of biosensors and bioassays described in the literature, with their properties and sensing performance.

Transducer type	Biological recognition element	Sensing surface/ Layer	Antigen/ Tested range	Incubation time / Time for analysis	Sensitivity / Detection limit	Ref
Optical ELISA Colorimetric	Capture antibody - LGl1–2 mAb Detection antibody - PL2–3 (physical adosorption via hydrophobic interactions)	Polyvinylchloride microtiter plates	histone H2B within the cell cytoplasm 3×10^4 to 8×10^2 cell per ELISA well	4 hours preparation (1 hour analysis)	3×10^4 cells per ELISA well	[114]
Optical Lateral flow assay with fluorescence-based detection	Anti-CRP (Covalent immobilisation on carboxylic groups to red fluorescent nanoparticles	Nitrocellulose membrane	CRP 0.1 – 160 mg/L	3-hour preparation time (3 minutes analysis time)	0.091 mg/L	[117]
Optical Whispering-gallery mode biosensors optical frequency shifts	Anti-cytochrome c (covalent immobilisation via biotin-streptavidin interaction)	Biotin-dextran modification of microbeads	Cytochrome c 3 nM – 30 nM	30 minutes incubation time (5 min analysis time)	6.8 nM	[115]
Optical Fluorescence imaging	Genetically modified enhanced green fluorescence protein (EGFP) to caspase-3 specific cleavage linker	Glass coverslip	Caspase-3 in total protein solutions extracted from HeLa Cell	No preparation time required. Live cells were monitored.	Fluorescence increase can be detected 32 minutes post-induction of 1 μm STS at 398 nm	[116]
Mass-based Piezoelectric	Indium tin oxide	Gold quartz crystals	Osteosarcoma MG63 cells 0.1×10^4 to 10×10^4 cell/mL	No analysis time reported	2.06×10^3 cell/mL	[100]
Mass-based QCM	Antibody Anti-M1 protein (covalent immobilsation via protein A)	Gold quartz crystals	Influenza virus A 1×10^3–1×10^8 pfu/mL	No analysis time reported	1×10^4 pfu/mL with stock QCM preparation 1×10^3 pfu/mL with gold nanoparticle signal amplification	[101]
Electrochemical Non-faradaic impedance spectroscopy	Poly-D-lysine (covalent immobilisation via APTMS as linker molecule)	silicon nanowire field-effect transistor	Rat adrenal pheochromocytoma cells 1×10^7 cells/mL	No analysis time reported	1×10^7 cells/mL	[109]
Electrochemical Cyclic voltammetry	Caspase-3 substrate (covalent immobilisation via π-stacking	Graphene deposited on glassy carbon electrode	Caspase-3 0.5 pg/mL to 10 ng/mL	15 min incubation time (3 minutes analysis	0.2 pg/mL	[105]

	interactions			time)		
Electrochemical Non-faradaic impedance spectroscopy	Anti-CRP antibody (physical adsorption via electrostatic interactions)	ZnO-CuO nanocomposite film deposited on PET substrate	C-reactive protein 1 and 10 ng/mL	10 min incubation time (3 minutes analysis time)	1 ng/mL	[111]
Electrochemical Amperometry	DEVD-pMA (caspase-3 specific substrate)	Oxidation of pMA released from DEVD-pMA by caspase-3 leads to increased amperometric currents	Caspase-3 0 – 2.5 x 10^{-2} units/mL	1-hour incubation time (no analysis time reported)	2.0×10^{-4} units/mL	[118]
Electrochemical Cyclic voltammetry	M13 phage peptide libraries (Ph.D.-C7C) (Covalent immobilisation via EDC/NHS chemistry)	11-mercaptoundecanoic acid (11-MUA) SAM on Gold electrodes	Caspase-3 0–1.2 μM	1-hour incubation time (3 minutes analysis time)	0.39 μM	[119]
Electrochemical Non-faradaic impedance spectroscopy	Anti-procalcitonin (PCT) Anti-CRP (covalent immobilisation via dithiobis (succinimidyl propionate) DSP crosslinker	100 nm ZnO thin film deposited on gold interdigitated electrodes using RF-magnetron sputtering	0.01 ng mL^{-1} to 10 ng mL^{-1} for PCT 0.01 μg mL^{-1} to 20 μg mL^{-1} for CRP	15 minutes incubation period (3 minutes analysis time)	0.10 ng mL^{-1} for PCT and 0.10 μg mL^{-1} for CRP	[84]
Electrical Non-faradaic impedance spectroscopy	Anti-CRP (Non-covalent immobilisation on ZnO/CuO nanoparticles)	ZnO/CuO nanoparticles embedded in nitrocellulose membrane	CRP 0.1 – 15 ng/mL	10 minutes incubation time (3 minutes analysis time)	16 pg/mL	[89]
Electrical Non-faradaic impedance spectroscopy	N/A	12 well Polystyrene plates	cell line ECV304 2×10^5 cells/well	3 minutes analysis time	Detected change in cell size five hours post DMSO treatment	[120]
Electrical biosensor Indium–Gallium–Zinc Oxide thin film transistor	Anti-epidermal growth factor receptor (EGFR) (physical adsorption)	Indium-Gallium-Zinc oxide thin film transistor on glass substrate	0.1 ng/mL EGFR in the total protein solution extracted from Hs58 cell line	8 minutes preparation time (3 min analysis time)	36.2 fM from the total 0.1 ng/mL solution	[121]

1.8 Nanomaterials

As evidenced in section 1.7, many electrochemical biosensors are based on various modified surfaces that increase the number of bioreceptors on the sensor surface, and consequently improving the performance of antibody-based biosensors [122]. The use of nanomaterials with large surface area to volume ratios and high conductivity can increase the loading number of peptides or substrates on the electrode surface resulting in amplification of the electrical signal [105].

1.8.1 Zinc oxide nanoparticles

In order to achieve low detection limits and high sensitivity the immobilizing matrix used in immunosensors should have high surface functionality, high biomolecule loading and small resistance to electron transport with high electron transfer rate [113]. Zinc oxide (ZnO) is a n-type semiconducting material that satisfy these conditions and has been used for many biosensing applications [113,123–126]. For example, ZnO nanorods (< 100 nm) boast high surface-to-volume ratio allowing for a high loading density of proteins [127]. ZnO also provides excellent functional and morphological properties including biocompatibility, chemical stability in physiological environments, low toxicity and a high isoelectric point (IEP) of about 9.5 [123]. The high ionic strength and pH stability makes ZnO a suitable choice for biosensing in biological fluids where a reasonable lifetime is required [124,128]. In a biosensor designed to detect negatively charged biomolecules, maintaining the ZnO surface at a pH of around 7 (slightly acidic) will ensure a strong positive charge, enhancing the capture and detection efficiency of the sensor [238].

From a structural perspective, ZnO can crystallise both in cubic (sphalerite) and in hexagonal (wurtzite) forms [129]. The wurtzite structure is most commonly used as it has the highest stability under normal working conditions. This is due to the tetrahedral stacking of Zn^{2+} and O^{2-} ions along the c-axis [130]. Native ZnO intrinsically has n-type conductivity due to the presence of oxygen vacancies and zinc interstitials [130]. ZnO also possesses other favourable properties such as near UV emission and transparency in the visible region, piezoelectricity and pyroelectricity, however these features are not relevant in electrochemical sensors [123].

When an electrolyte interfaces with a semiconducting material, an electrical double layer (EDL) is formed due to the polarization of charges on the sensing surface [131]. This electrical double layer is described in more detail in Chapter 2. The charge accumulation of ionic liquid and ZnO associated with am EDL can be measured using EIS. This phenomenon is discussed in more detail in further sections. At physiological pH values, ZnO's high isoelectric point (IEP~9.5) enables stable immobilization of biomolecules with lower IEP through electrostatic interaction, this allows the biosensor to retain biological activity on its surface [84]. ZnO nanostructures have high surface to volume ratio which results in improved biosensor sensitivity. Due to its increasing number of applications and research interest, pure ZnO can now be synthesised with large scale and cost-effective methods [132]. This combination of properties makes ZnO nanoparticles particularly attractive as a nanomaterial for biosensor development.

1.8.2 Copper oxide

To further enhance the biosensing capabilities of metal oxide-based sensors, efforts have been made to improve the optical or electrical properties by incorporating other nanomaterials or elements within the ZnO matrix. For example, modification of ZnO with metal oxide nanomaterials can further improve the features of ZnO for the sensing of biomolecules as metal oxide nanomaterials make excellent catalysts due to their high surface ratio of atoms with free valences of the total atoms in the cluster[133]. Therefore, the integration of ZnO with other metal oxides can provide new avenues for the development of highly sensitive and specific biosensors. With regard to the material aspect of design choice, various metal oxide nanomaterials have been utilized for biosensing applications such as iron oxide, cerium oxide, magnesium oxide, and titanium oxide [89,111,134–136]

Recently, p-type materials such as copper oxide (CuO) have also been suggested to provide enhanced functionalities as counterparts of n-type materials through the formation of p-n junctions [89,137]. The addition of copper oxide (CuO) to ZnO has been shown to improve sensitivity by enhancing the redox property and electron transfer [67]. Lee *et al.* [137]presented a ZnO-CuO chemiresistive acetone sensor that comprised CuO nanocubes attached to ZnO nanospheres and showed higher sensitivity and lower detection limits than other acetone sensors. The interparticle p-n junctions resulted in increased resistance in response to reducing gases compared to p-p junctions alone. Other structural factors, such as small grain size and large surface area of each domain also enhance the surface gas adsorption [111]. Composites of ZnO-CuO have also been used in protein sensing applications [89,111,125]. Batra *et al.* [125] deposited a ZnO-CuO composite matrix on to ITO coated glass substrate. The inclusion of the ZnO-CuO matrix facilitated faster electron transfer from the redox enzyme to

the electrode surface [125]. The modification of NC membrane with CuO has also been reported. Cao *et al.* [89] fabricated a nano-ZnO/CuO NC membrane biosensor using a simple sonication technique. The sonication force assisted the loading of nanoparticles into the lower layer of the membrane. The addition of CuO nanoparticles to form a nano-ZnO/CuO NC membrane biosensor resulted in enhancement performance of the impedimetric biosensor [89].

1.8.3 Fabrication of ZnO and CuO nano-surfaces

Various methods are used to deposit ZnO and CuO thin films, and other types of nanostructures, on to substrates for biosensors, such as magnetron sputtering techniques [138], sol gel processes [139], pulsed laser deposition [130], chemical vapor deposition [140] and hydrothermal methods [141]. Some of these studies have used methods such as hydrothermal and vapour deposition processes to gain a high density ZnO structures. However, in one example in which ZnO was deposited on gold electrode surfaces, it was reported that the electrical properties of ZnO were very sensitive to both temperature and stress and achieving high quality reproducible thin films was a technological challenge [142].

Drop-casting method is a quick and simple method for fabrication of ZnO nanostructures and even on a large scale, it could be low cost [143]. Drop-casting is the formation of a thin solid film by dropping a solution onto a flat surface followed by evaporation of the solvent to leave behind the solid film. Morfa *et al.* [144] fabricated ZnO thin films using a simple drop-casting technique. The ZnO nanofilm formed exhibited consistent physical and electrical properties such as particle size, monodispersity, film porosity and resistivity [144]. Anusha *et al.* [145] presented an enzymatic glucose biosensor with the aid of ZnO nanostructures on glass

substrate by simple drop casting technique. The biosensor showed good analytical performances with high sensitivity (62.14 μA mM^{-1} cm^{-2}) in a wide linear range and low detection limit (16.6 μM glucose) [145]. The drawback of this technique is the lack of control over the film thickness, however the method is quick and simple and can be implemented without the need of expensive equipment. Another drawback of this drop-casting approach is the potential aggregation of particles due to the electrostatic attraction. Therefore, it is important to ensure the nanoparticle suspension is homogenous. A simple method of achieving a dispersed nanoparticle suspension is using sonication.

1.8.4 Dispersion of nanoparticles

Nanoparticles, such as ZnO, are inorganic compounds and although they are insoluble in water, they can be homogenously dispersed in dilute acids and bases [146]. Cao *et al.* [147] synthesized a ZnO nanoparticle suspension in ethanol without using any surfactants. Moreover, ZnO nanoparticles possesses small size with large surface area. This often led to agglomeration of particles and formation of sediments at the bottom of dispersion containers [146]. To overcome this problem, researchers have tried to modify the nanoparticles with organic compounds or polymers to reduce the attraction between particles [147]. One way to achieve this is by altering the surface charges so that the particles repel each other; this is known as electrostatic stabilization[146]. Another way to achieve this is through steric stabilization, which used hinderance of large molecules to keep particles away from each other [146]. A commonly used dispersing agent is sodium dodecyl sulfate (SDS). It contains strong negative charge which can effectively stabilize the dispersion. Anand et al. [148] compared the role of different surfactants on stability and particle size of ZnO in water. The quality of dispersion was improved by adding SDS, with a larger number of particles retained

in the nanosize range [148]. Sonication in the presence of SDS further enhanced the share of lower-sized particles [148].

Sonication is a widely used technique for the dispersion of nanoparticles in a fluid. This method relies on the use of ultrasound to fragment large agglomerates and avoid subsequent particle aggregation. In an ultrasonic system, the probe transfers energy into the fluid in the form of pressure waves which fragments the agglomerates and excess energy heats up the surrounding fluid. Chung *et al.* [149] compared the characteristics of ZnO nanoparticles in water prepared in either an ultrasonic bath or with a probe. Their findings suggest that using a probe immersed in the suspension was more effective than bath immersion for the dispersion of ZnO nanoparticles in aqueous solution [149]. Lee et al. [150] used a simple ultrasonication technique to form a thin layer of ZnO nanopillar arrays while maintaining its nanostructures with minimum damage to the nano-features during the synthesis. Ultrasonic techniques have also been used to achieve colloidal dispersion of other metal oxide nanomaterials. Bertel *et al.* [136] presented an electrochemical DNA sensor based on titanium dioxide (TiO_2)-coated carbon electrodes. Titanium dioxide hollow microsphere colloid powder was sonicated in an aqueous solution to produce a well-dispersed colloidal suspension [136].

Overall, ultrasonication techniques offer a simple, cost-effectiveness method for nanoparticle dispersion. This can be used in combination with drop-casting method to produce homogenous nanoparticle films or surfaces without the need for expensive equipment, harsh chemicals, or extreme temperatures. Due to these advantages, these techniques were chosen in this study to fabricate ZnO/CuO nanocrystal films for the sensor surface.

1.9 Summary

It is known that morphological hallmarks of apoptosis often lag behind the biochemical changes. During apoptosis, caspases are activated and cause a cascade of events that eventually lead to cell destruction. Caspase-9 is an enzyme involved in the intrinsic apoptosis pathway, which has been shown to the dominant pathway in CHO cell cultures. Therefore, the detection of caspase-9 early in the apoptosis process is of great importance as it will enable faster responses or pharmaceutical interventions to rescue the culture and enhance culture longevity and productivity. In this chapter, the significance of caspase-9 in apoptosis and the need for apoptosis monitoring in industrial cell lines have been addressed. Issues with the current techniques for apoptosis detection have also been discussed.

In this chapter, the basic components of a biosensor have been described and various biosensing approaches have been identified from the literature. These methods were compared and benefits associated approach used in this research study were highlighted.

Of the biosensing approaches, antibody-based impedimetric biosensors can offer very high specificity and selectivity. Within the impedance spectroscopy modes, the non-faradaic mode does not require the presence of redox probes and thus is more amenable to miniaturization and to online/real time application. However, the application of this type of sensor for caspase detection and apoptosis monitoring in CHO-K1 culture samples has not yet been investigated. Nanomaterials, such as ZnO and CuO, has been shown to improve the sensitivity of biosensors and can act as effective platforms for immobilisation of antibodies

through non-covalent interactions. Ultrasonication is a simple and convenient method of dispersing nanoparticles in fluid.

1.10 Objectives and structure of the thesis

Building on work presented in the literature the goal of the research presented in this thesis is to develop a simple, sensitive, impedimetric biosensor using ZnO/CuO nanoparticles for the detection of apoptosis in CHO cell through the measurement of caspase-9 released into the cell culture media.

The research objectives are:

1. To design and fabricate a sensitive caspase-9 biosensor surface through an investigation of critical parameters, in particular, the ratio of ZnO:CuO and antibody loading associated with functionalisation.
2. To demonstrate a working ZnO/CuO impedimetric biosensor to caspase-9, with high sensitivity, selectivity and reproducibility.
3. To develop a cell model for apoptosis in CHO cells, using apoptotic agents, which can be validated using optical and enzymatic methods.
4. To demonstrate that the impedimetric biosensor can measure increasing caspase-9 concentrations with higher levels of apoptosis in cell culture media from the CHO cell model.
5. To develop a theoretical model of a non-faradaic impedimetric, ZnO/CuO biosensor.

To deliver these objectives the thesis is structured as follows. Chapter 2 presents the basic terms and general principles surrounding impedance spectroscopy. Impedance spectroscopy processes can be categorised into two classes: faradaic and non-faradaic. This chapter also

provides brief details of relevant physical principles such as the electrical double layer and the Debye length. A simple electrical circuit model based on the Randles model was developed to help understand the non-faradaic ZnO-CuO sensor's operation. Chapter 3 focuses on the development of the ZnO/CuO composite sensor surface for the detection of caspase-9. The surface is characterised by morphological and biochemical analysis via SEM and ELISA, respectively. Impedance spectroscopy was used to measure the binding interaction between caspase-9 and antibody. Optimal antigen incubation times were determined with by measuring the change in output signal over time. The impedance spectra and impedance changes were compared surfaces functionalised with different antibody concentrations to determine the optimal antibody loading concentrations. In chapter 4, a cell model was developed for apoptosis detection in CHO cells, an apoptotic agent was used to accelerate the apoptotic process and enable the detection of apoptosis in a reasonable time frame. The cell model was then validated against an optical method using nuclear staining and an enzymatic method which measured caspase activity linked with apoptosis progression. The impedimetric biosensor was tested using increasing concentrations of caspase-9 which is associated with higher levels of apoptosis in CHO cells. In addition, an equivalent circuit model was fitted to better understand the biomolecular events occurring at the sensor surface. Chapter 5 then investigates how the sensor could be used in a bioreactor setting, with potential adaptation to allow for continuous *in situ* monitoring of apoptosis.

Chapter 2
Impedance Spectroscopy

Impedance spectroscopy is a sensitive technique which can be used for the analysis of the interfacial properties related to biorecognition events, such as reactions catalysed by enzymes or biomolecular recognition events of specific binding proteins, receptors, nucleic acids, whole cells, antibodies or antibody-related substances, occurring at a sensor surface. Many studies on impedimetric biosensors are focused on immunosensors. In impedimetric immunosensors, the binding interaction between antibody and antigen complex leads to the formation of an immunocomplex and this results in a change in the interfacial electrical properties at the sensing surface.

Impedimetric biosensors measure the changes in resistive and capacitive properties at the sensor surface as selective binding of the target occurs. An impedance spectrum is obtained by varying the frequency of the input voltage signal over a defined range so that the resistive and capacitive elements of the system can be determined from the real and imaginary parts of the current responses. In this PhD project, impedance spectroscopy was used to detect immunological binding events between an antibody and the analyte occurring on the sensing surface of the biosensor, and thus quantifying the analyte concentration delivered to the zinc oxide/copper oxide (ZnO/CuO) nano-surfaces.

This chapter presents the basic terms and concepts associated with impedance spectroscopy. Impedance spectroscopy processes can be categorised into two classes: faradaic and non-faradaic. The sensing principles and the applications of both classes in biosensing are discussed. This chapter also provides brief details of relevant physical principles, e.g. electrical double layer. The methods of analysing impedance spectroscopy data are also discussed.

Finally, in this chapter a simple electrical circuit model of the non-faradaic impedimetric ZnO/CuO nano-crystal sensor used in this PhD project is presented. The model is based on the generalised Randles model and adapted for the unique properties associated with the non-faradaic sensors studied in this work. This biosensor had a glass insulating layer between the electrodes and the active ZnO/CuO sensor surface and impedance spectroscopy was used to measure the varying concentrations of caspase-9. The aim of creating this model is to enhance understanding of the biosensor operation and thus aid future biosensor development.

2.1 Comparison between faradaic and non-faradaic processes

Electrochemical Impedance Spectroscopy (EIS) is a powerful tool for investigating the interfacial properties related to bio-recognition events. The impedance can be measured in the presence or absence of a redox couple, which is referred to as faradaic and non-faradaic impedance measurement, respectively. In faradaic processes, charge (electrons) is transferred across an interface [151]. In the case of non-faradaic, transient currents can flow without charge transfer (e.g., charging a capacitor). In faradaic impedance spectroscopy, a redox probe is alternatively oxidised and reduced by the transfer of electrons to and from the electrode [151]. In contrast, no additional reagent is required for non-faradaic impedance spectroscopy, rendering non-faradaic techniques more amenable to miniaturisation and point-of-care applications [89,111,152,153].

In the case of faradaic impedance spectroscopy, the electrode surface is partially or fully covered with a non-insulating layer or with an isolating layer able to catalyse a redox probe [151]. Faradaic electrochemical impedance spectroscopy generally uses a low, constant sinusoidal AC voltage applied to a three-electrode cell containing an electrolyte solution (such as potassium ferricyanide) [154]. In this configuration there is a working electrode, counter electrode and an independent reference electrode, each can be made from a wide variety of materials (carbon, gold, platinum, etc.), depending on the specific application. When the AC potential is applied to the cell, current is transferred between the counter and working electrodes, and the potential between the working and reference electrodes is monitored [154]. The faradaic process occurs at the working electrode, where the redox probe is alternatively oxidized and reduced by the transfer of an electron to and from the electrode [154].

The binding of biomolecules on the electrode surface typically results in a detectable increase in the charge transfer resistance.

In the non-faradaic approach, the redox probe is missing, the impedance depends on the conductivity of supporting electrolyte and electrode interfacial properties [151]. Capacitive biosensors are mainly based on the non-faradaic approach because the transient current flows without charge transfer and no redox probe is required [155]. The charge is associated with movement of electrolyte ions, reorientation of solvent dipoles, adsorption/desorption, etc. at the electrode-electrolyte interface [151]. Due to the lack requirement for redox probes, the sample preparation processes of non-faradaic approach are less complex and more suitable for point of care testing.

Table 2.1 shows a small selection of impedimetric biosensors, including faradaic and non-faradaic devices, and it identifies their detection principles and sensitivity/detection limits. The main conclusions drawn from the publications in this table are:

1. Non-faradaic biosensors can provide label free detection without chemical transformations, resulting in simple methods with low sample consumption [89,111,142,156–158].

2. Antibodies are the most widely used affinity element in impedimetric sensors [72,89,106,108,111,155,159,160]. Detection of biomolecules based on enzymatic cleavage is commonly used for enzyme targets [161].

3. Faradaic biosensors based on enzymatic cleavage often require additional labels or nanomaterials to amplify the signal [104,122]. For example, Xia *et al* [104] added a high-molar-mass biomolecule as a signal amplifier to enhance the detection of caspase-3 activity. The sensor was based on the site-specific cleavage of caspase-3 specific substrate which then allowed for the access of redox couple to the electrode surface. The addition of Streptavidin-biotin-phenylalanine network was able to hamper the access of the negatively charged $[Fe(CN)_6]^{3-/4-}$ redox couple to the electrode surface more effectively resulting in increase in resistance [104].

4. In order to present information about surfaces, layers, or membranes after the immobilization of biomolecules, EIS experimental data is often analyzed using an equivalent circuit of an electrochemical cell. The Randles circuit is a frequently used for modelling the electrical components that determine the total impedance [151]. A faradaic sensor comprises the resistance of the electrolyte (R_s) in series with the capacitance of the electrical double layer (Cdl) in parallel with the charge transfer resistance (R_{ct}) and the Warburg impedance (Z_w), which describes diffusion phenomenon taking place due to chemical redox process. In the non-faradaic sensor model, there is no charge transfer across the electrode, therefore Z_w and R_{ct} can be neglected [151].

5. For faradaic sensors, the charge transfer resistance (R_{ct}) can be extracted from the Nyquist plot and changes in R_{ct} are dependent on the binding of antigen on the electrode surface. Bode plots are often used to analyse non-faradaic sensors as the dose response is frequency dependent. Low frequencies are usually selected, due to significant changes in impedance between the different doses of antigen being observed at frequencies below 1000 Hz [89,111,162].

6. Faradaic approaches typically operate in a three electrode setup, comprised of a working electrode, a counter electrode and a reference electrode. Contrary to the faradaic EIS, the non-faradaic method does not demand the use of redox couples and, consequently, no reference electrode is necessary, because no DC potential is required [108]. These features make this kind of sensors more amenable to miniaturization and to online/real-time applications.

7. Capacitive biosensors are a sub-category of impedance biosensors. They operate by measuring the dielectric changes due to the binding of the target analyte to the sensor surface/conductive substrate.

8. In some cases, faradaic sensors may offer lower detection limits compared to non-faradaic sensors due to their ability to directly participate in redox reactions and electron transfer processes, which can lead to more sensitive detection of certain analytes. For instance, Park *et al* [162]compared the two types of sensors for the detection of amyloid beta and the overall impedance change was greater for the faradaic approach due to the presence of charge transfer resistance.

Table 2.1 Comparisons of faradaic and non-faradaic biosensors

Sensor	Faradaic or non-faradaic	Sensing principle	Biological recognition element	Sensing surface/ Layer	Detection Limit	Data analysis	Ref
EIS detection of cytochrome c and caspase-9 in Hela cells	Faradaic	Antibody-antigen binding results inhibited electron transfer and increase impedance value.	Anti-cytochrome c and anti-caspase-9 (physical immobolisation through electrostatic interactions)	Dopamine and gold nanoparticle functionalised glassy carbon electrodes.	0.03 µM for cyt c 0.08 µM for caspase-9	Nyquist plots, cyclic voltamograms, calibration curves.	[160]
Impedimetric urea biosensor based on reactive RF magnetron sputtered ZnO thin films	Faradaic	Current measured by varying the potential across the film.	Urease enzyme (non-covalent immobilisation via physical adsorption)	Sputtering of ZnO nanoporous thin film on conductive fluorinated-tin oxide (FTO) layer.	0.83– 23.24 mM Detection limit of 0.4 mM	Current-Voltage curves	[163]
Impedimetric biosensor for the monitoring of caspase-3 activity using biotin-phenylalanine as signal enhancer	Faradaic	Charge transfer resistance decrease due to the cleavage of caspase-3 specific substrate.	Caspase-3 specific substrate (covalent attachment through Au-S interaction)	Gold electrodes modified with streptavidin and biotin-phenylalanine	1 pg/mL	Nyquist plots, correlation between charge transfer resistance and concentration	[104]
Detection of Insulin Using Electrochemical Impedance Spectroscopy	Faradaic	The imaginary impedance was correlated to insulin concentration on a gold disk electrode with insulin antibody immobilized	Anti-insulin antibody (covalent immobolisation using EDC-NHS chemistry)	Antibody immobilised on gold disk electrodes through self-assembled monolayer formed using 16-mercaptohexadecanoic acid	Limit of detection 2.64 pM	Nyquist plot, correlation of charge transfer resistance to target concentration	[157]
Amyloid beta detection by faradaic impedance spectroscopy using interdigitated microelectrodes	Faradaic	Protein binding results in the suppression of charge transfer process by the redox probe.	Anti-Amyloid beta antibody (covalent immobolisation using 3-amino-propyl triethoxysilane (APTES)	Antibody immobilised on SiO_2 layer.	10 fold increase in sensitivity compared to the non-faradaic version.	Bode plots, % change in impedance was compared	[162]

Impedimetric biosensor using silicon nanowire field-effect transistors for the monitoring of neuronal cell growth	Non-faradaic	Changes in the impedance were caused by the negatively charged cell membrane at the cell/SiNW interface.	Poly-D-lysine (covalent immobilisation via APTMS as linker molecule)	silicon nanowire field-effect transistor	1×10^7 cells/mL	Bode plots	[109]
Electrochemical impedimetric profiling of procalcitonin and C-reactive protein as a dual marker biosensor	Non-faradaic	Antibody-antigen binding results in changes in imaginary impedance.	Anti-procalcitonin (PCT) Anti-CRP (covalent immobilisation via dithiobis (succinimidyl propionate) DSP crosslinker	100 nm ZnO thin film deposited on gold interdigitated electrodes using RF-magnetron sputtering	0.10 ng mL^{-1} for PCT and 0.10 µg mL^{-1} for CRP	Nyquist plots and Bode plots	[84]
Impedimetric biosensor using CuO/ZnO nanofilm to detect CRP	Non-faradaic	Impedance measurement of antibody-antigen binding at the sensor surface.	Anti-CRP antibody (physical adsorption via electrostatic interactions)	ZnO-CuO nanocomposite film deposited on PET substrate	1 ng/mL	Bode plots	[111]
Impedimetric biosensor using CuO/ZnO embedded in nitrocellulose membrane to detect CRP	Non-faradaic	Impedance measurement of antibody-antigen binding.	Anti-CRP (Non-covalent immobilisation on ZnO/CuO nanoparticles)	ZnO/CuO nanoparticles embedded in nitrocellulose membrane	16 pg/mL	Bode plots	[89]
Nanoporous silica-based sensor for enhanced electrochemical detection of CRP and MPO	Non-faradaic	Protein binding results in a increase in capacitance in the electrical double layer	Anti-CRP and Anti-myeloperoxidase (MPO) (Covalent immobilisation via streptavidin interaction)	Polylysine-coated gold electrodes	1 pg/ml for CRP and MPO on diatom membranes 1 ng/mL on planar gold electrodes	Bode plots, impedance change were compared	[164]
Label-free detection of thrombin using EIS of aptmer functionalised MOS_2	Non-faradaic	Thrombin binding to thrombin aptamer on the electrode surface results in impedance changes.	Thrombin aptamer (covalent attachment via 5'-thiol modification)	Molybdenum disulphide (MOS_2) nanosheets deposited onto platinum electrodes.	267 fM in PBS buffer 53 pM in human serum samples	Bode plots, Change in impedance against thrombin concentration	[156]

2.2 Impedance Spectroscopy Theory

2.2.1 Mathematical Theory of EIS

Electrical impedance is the measure of total opposition that a circuit presents to electric current of a single frequency. Impedance includes both resistance and reactance. The resistance component arises from collisions of current-carrying charge particles with the internal structure of the conductor [165]. The reactance component is an additional opposition to the movement of electric charge that arises from the changing magnetic and electric fields in circuits carrying alternative current[165].

For impedance measurements, sine waves are frequently used because of their ease of representation. In its most basic form, the relationship between voltage and current, as a function of time (t), is:

$$V = I_0 \sin(\omega t) \times Z$$

(2.1)

Where I_0 is the peak current, ω is the angular frequency and Z is the impedance. Angular frequency is related to the frequency, by:

$$\omega = 2\pi f$$

(2.2)

The electrical impedance Z(ω) at an angular frequency ω, is the ratio of the applied AC potential difference V(ω) to the AC current I(ω). The impedance has a real Z'(ω) and an imaginary Z"(ω) part according to the below formula, where j is the operator that signifies the imaginary component.

$$Z(\omega) = \frac{\mathrm{V}(\omega)}{\mathrm{I}(\omega)} = \mathrm{Z}'(\omega) + j\mathrm{Z}''(\omega)$$

For an input voltage, V, at time t giving a current, I, the impedance across a capacitor (C) is calculated from the following (where Vo is the peak current).

$$Z = \frac{V}{I} = \frac{V_0 \sin(\omega t)}{C \times \omega V_0 \cos(\omega t)} = \frac{1}{\omega C} \times \frac{\sin(\omega t)}{\cos(\omega t)}$$

(2.3)

For a fixed capacitance, as angular frequency increases, the reactance of a capacitor decreases. This is because the higher the frequency, the larger the amplitude of the current through the capacitor. This is because the AC current through the capacitor will increase with higher frequency and hence its impedance will be less.

The reactance (X) expresses a component's resistance to AC, whereas impedance (Z) indicates a component's resistance to both AC and DC. Total impedance can be expressed by the following equation:

$$Z = R + jX$$

(2.4)

The impedance of an ideal resistor is the equivalent of its resistance. Under such conditions, the real part of the impedance is the resistance and the imaginary part is zero. The impedance of a capacitor can be derived from its capacitance values (C) and the frequency of the signal passing through it (f). The following formula can be used to calculate the reactance:

$$X_c = \frac{-j}{\omega \mathrm{C}} = \frac{-j}{2\pi f C}$$

(2.5)

In order to calculated an impedance vector from real and imaginary parts, the reactance value of a capacitor is multiplied by *-j*. In this context, the -j term represents a 90-degree phase shift that occurs between current and voltage in the purely capacitive circuit. The impedance of a capacitor is given by following formula:

$$X_c = \frac{-j}{\omega C}$$

(2.6)

A capacitor's capacitance is directly proportional to the surface area of its plates and inversely proportional to the separation between these plates [166]. However, net capacitance also depends on the dielectric constant of the substance separating the plates [166].

For a capacitance/resistance combination, the magnitude (modulus) of the impedance, |Z| can be calculated as follows:

$$Z^2 = R^2 + {X_C}^2 \;\therefore\; |Z| = \sqrt{R^2 + {X_C}^2}$$

(2.7)

2.2.2 Electrical Double Layer

The electrical double layer (EDL) is described as an interfacial layer formed when a conductor/semiconductor material comes into contact with an electrolyte (ionic liquid). In particular, the EDL formed at a metal/electrolyte interface is central in electrochemistry, with a plethora of applications ranging for capacitive coating, corrosion batteries and biosensors [167]. This double layer is formed as ions from the solution adsorb onto the electrode surface [168]. The charged electrode surface is separated from the charged ions by an insulating space, often in the order of angstroms [151]. Charges separated by an insulator form a capacitor so measuring the capacitance changes in the EDL can provide insights on the concentration of bio-molecular binding at or near the interface [167,169]. A diagram representing the formation of an EDL at the surface of zinc oxide (ZnO) thin film is shown in **Figure 2.1**. An EDL is created when the buffer solution containing antigen is brought into contact with an antibody-functionalised ZnO nano-surface. In the diagram, the distribution of positive and negative ions on the surface is depicted. The first and simplest model of an EDL was proposed by Helmholtz in 1879 [165]. In the Helmholtz model, at the interface of a charged surface and electrolyte, there is a layer of "adsorbed", solvated ions of the opposite charge [165]. The separation of opposite charges can be compared to the behaviour of a capacitor in an electrical circuit.

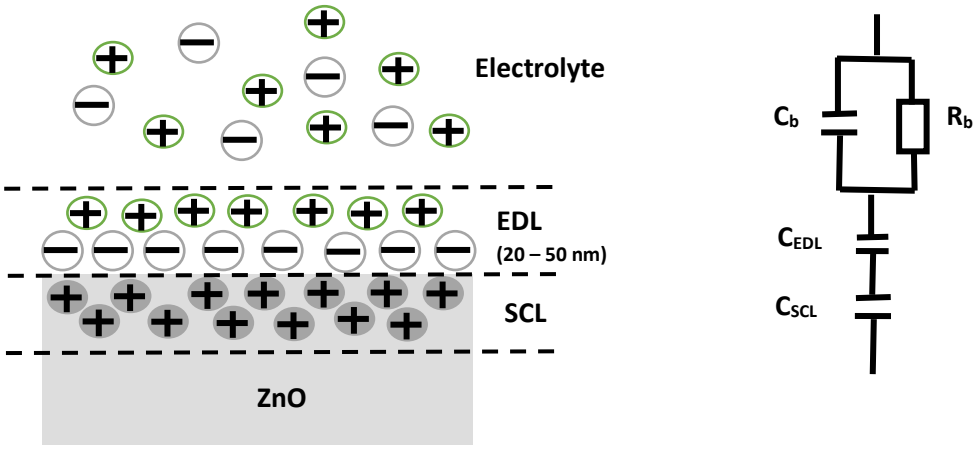

Figure 2.1 A diagram of charge distribution at the ZnO surface and a simple equivalent circuit model of each layer.

The structure can be divided into three planes, i.e., the space charge layer (SCL), electrical double layer and the diffuse layer (**Figure 2.1**). The SCL is occupied by immobile charge carriers within the semiconductor [124]. Zinc oxide, is an n-type semiconductor, which, upon contact with an electrolyte, will result in the transfer of charge (electrons) from the electrode into the solution. Under physiological conditions, ZnO possess an isoelectric point (IEP) of 9.5, which is much higher than the IEP of most biomolecules. Thus, the diagram depicts a SCL comprised of positive charges which has a thickness of several nanometers [124]. The next region is the characteristic electrical double layer which consists of the inner Helmholtz plane (IHP) formed by adsorbed ions and solvent species and the outer Helmholtz place (OHP) formed by the attraction of ions of opposite charge, via Coulomb force [124]. The third region extended into the bulk of the electrolyte constituted by concentration profile of solvated ions

that formed the diffuse layer [124]. Beyond the Debye length which is considered as the approximate thickness of the EDL, the attraction of counterions to the electrode is reduced [166].

A number of authors have adapted the Randles model to create equivalent electrical circuits in order to better understand the influence of EDL capacitance associated with ZnO biosensors [124,166,170,171]. Eveness *et al* [170] created an equivalent circuit model to quantify charge modulations arising due to biomolecular binding of C-reactive protein within the EDL formed at the ZnO-PBS interface. Tanak *et al* [84] fitted a Randles equivalent circuit to the impedance spectra of interdigitated gold electrodes fabricated on a flexible polyimide substrate coated with a thin film of ZnO. The increase in capacitance of the EDL with increasing dose concentrations was attributed to the capacitive binding effect at the electrode interface occurring due to antibody/antigen interaction [84]. Selvam *et al* [172] adapted the Randles model for interpretation of the impedance data from their ZnO-based biosensor. The measured impedance was dominated by the capacitance of the EDL formed at the sensing electrode-fluid interface [172]. The predominantly capacitive nature of the sensor is indicated by the 60 degree phase lag in the output impedance spectra [172].

2.2.3 Debye's Length

In electrolytes, the Debye length is a measure of a charge carrier's net electrostatic effect in solution and how far its electrostatic effect extends. In the context of a sensor surface, this defines the length-scale at which a charged analyte can be electrically probed at the detector interface [173]. If a charge resides at the distance further than the Debye length, it can be shielded by the ions of the electrolyte solution [173]. Debye length scale inversely with ionic strength, according to equation (2.10) [174].

$$\lambda = \left(\frac{\varepsilon_r \varepsilon_0 k_B T}{\Sigma_i \, C_i e^2 z_i^2}\right)^{\frac{1}{2}}$$

(2.10)

where C_i is the molar concentration (M) of ion i, ε_r is dielectric constant, ε_0 is the permittivity of free space, T is the temperature, k_B (=1.381 × 10^{-23} JK^{-1}) is the Boltzmann constant, e (=1.6021 × 10^{-19} C) is the elementary charge and z_i^2 is the ion valency [174]. Thus, according to the Poisson-Boltzmann model, a high concentration of ions leads to a screening of an electrostatic potential over short distances, while low ion concentrations allow the electric potential to decay over longer distances and thus the electric field can act over greater distances [174]. For example, a 1 x 10^{-3} M solution of NaCl in water at 25°C has a Debye length of λ_D = 9.6 nm, whereas a 0.1 M solution of NaCl has a Debye length of λ_D = 0.96 nm [174].

Ionic strength, I, is a measure of the concentration of electrically charged species in solution

$$I = \frac{1}{2}\sum_{i=1}^{n} C_i \, Z_i^2$$

(2.11)

Where C_i is the molar concentration of ion i of charge Z_i. For a simple 1:1 electrolyte solution such as sodium chloride (NaCl), where each ion is singly-charged, the ionic strength is equivalent to the concentration of the solution. The Debye length, δ, can be simplified as equation (2.12), where $Z_i = 1$, C is the molar concentration and N_a is the Avogadro number [175].

$$\delta = \left[\frac{\varepsilon kT}{e^2 N_a 2C}\right]^{\frac{1}{2}}$$

(2.12)

In this PhD study, the total ion concentration of the phosphate-buffered saline (PBS) solution was approximately 0.165 M, consisting of 0.01 M phosphate buffer, 0.137 M of the sodium chloride (NaCl) and 0.003 M of potassium chloride (KCl), giving a final pH of 7.4. Total ion concentration was defined as the sum of the concentrations of all the components in the solution.

The Debye length can be approximated using equations (2.10) and (2.12), where e is the charge of the electron and ε is the permittivity ($\varepsilon = \varepsilon_r \varepsilon_0$). The relative permittivity, ε_r of PBS is 80 and ε_r value of 3.2 is used for caspase-9. This number was derived from average protein permittivity values of more than 150,000 proteins [176]. T is the temperature with the unit of K. Room temperature of 293.15 K is assumed. Consequently, Debye length is calculated by to be approximately 1.06 - 2.37 nm in 0.5× PBS electrolyte. However, other variables such as the molecule's shape and roughness of the surface may alter the Debye length.

Caspase-9 is a 47 kDa protein, which is a stable heterotetramer that consists of two anti-parallel arranged heterodimers, each one formed by a 35 kDa (p35) and a 12 kDa (p12) subunit [177]. The large subunit houses the active site responsible for enzymatic cleavage; therefore, the antibody used in this study is specific to the p35 subunit, indicating it detects

active caspase-9 rather than procaspase-9. Assuming the protein has the simplest shape, a sphere, the estimated minimum radius for a 50 kDa protein is 2.4 nm [178]. The antibody used in this study is of the IgG isotype, which has a molecular weight of 151 kDa and dimensions of 16 x 5 x 5 nm [178]. Consequently, the binding reaction falls outside the Debye length calculated above.

Until recently it was considered that high sensitivity biosensors could not be created where the binding interaction occurred beyond the Debye length (calculated through 2.12), due to charge screening limitations. However, newer thinking recognises that the Debye length rule is a simplification and the limitations can be overcome through (at least) two techniques. Limiting screening through surface engineering and disrupting the double layer through electronic perturbation [179]. In this PhD study, these two methods have been utilised by employing a nanostructured sensor surface and by utilising impedance spectroscopy to create a dynamic double layer.

The Debye length under physiological conditions is around 1 nm; in contrast, the length of an antibody is on the order of 10–15 nm. Due to the mismatch in dimensions between the charge screening effects and size of biomolecules, many researchers recognise the charge screening issues and also have utilised impedance spectroscopy and the dynamic double layer scenario to perform sensitive measurements [179]. The impedance of the system is affected by the electrical double layer at the electrode-electrolyte interface, but the frequency dependence of the impedance allows for the separation of the effects of the EDL from those of the bulk electrolyte [170]. Widderhoven *et al* [180] demonstrated that high frequency impedance spectroscopy can enable the capacitive sensors to measure well beyond the Debye length.

They deposited microsphere on top of their microelectrode array and analyzed them at various frequencies[181]. At low frequencies, these beads were subject to screening and the sphere can only be detected as a change in capacitance where it contacts the array [181]. As the measurement frequency increases (up to 50 MHz), ion screening is perturbed, and the electrodes detect the microsphere [181].

2.2.4 Data presentation

Impedance data obtained from non-faradaic impedance spectroscopy experiments is typically presented as plots of impedance magnitude and phase as a function of frequency. The two most widely used plots are the Nyquist plot and the Bode plot. In the Nyquist plot, the real and imaginary components of impedance are plotted on the x and y axes respectively. **Figure 2.2** shows an example Nyquist plot for a circuit that contains a resistor and capacitor in parallel.

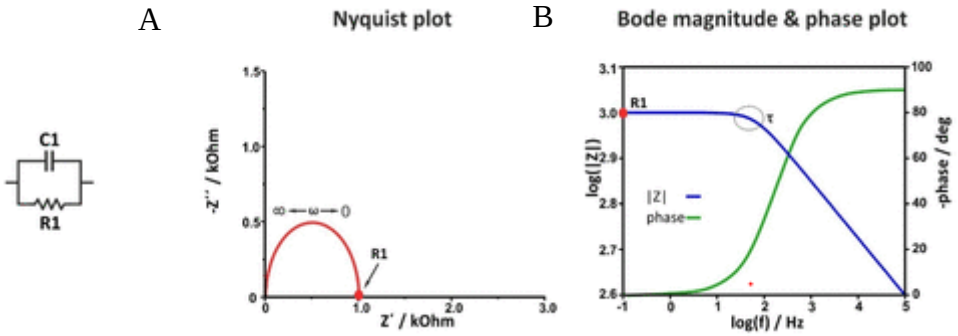

Figure 2.2. (A) Nyquist, (B) Bode magnitude, and phase angle plots of some model circuits.

In the bode plot, the impedance magnitude is usually presented on the y-axis of the plot and represents the absolute value of the impedance, which can be a combination of resistive and capacitive or inductive components. The impedance magnitude is typically plotted on a logarithmic scale to cover a wide range of values and to better visualize the behaviour of the system at different frequency ranges [169]. The impedance phase is usually presented on the x-axis of the plot and represents the phase angle between the applied alternating current or voltage and the resulting current or voltage response. The phase angle provides information about the nature of the electrical components of the system, such as the capacitive or inductive behaviour.

The Bode plot is another way to represent impedance data that shows the magnitude and phase of impedance versus the logarithm of frequency. The Bode plot is often used to analyze the frequency response of a system, particularly when there is a resonance or dominant frequency in the system [108].

The majority of studies on impedimetric biosensors in the literature use the impedance spectrum to identify the optimum frequency (or frequency range) at which the analysis should be performed. A similar approached was used in this work to identify frequencies at which the signal is stable and distinct differences in impedance can be observed between samples. Explanations for the frequencies selected are given in the subsequent chapters.

The dose response curves illustrate the relationship between the concentration of an analyte and the corresponding biosensor signal, offering a comprehensive understanding of sensitivity, detection limits, and dynamic range. By systematically varying analyte concentrations and

monitoring the resultant biosensor outputs, these curves provide valuable insights into the sensor's performance characteristics, such as its sensitivity and specificity. This analytical approach has deployed in various studies to evaluate sensing performance and other essential metrics [84,89,111,143,160].

2.3 Equivalent circuit models of Impedimetric biosensors

2.3.1 Randles model

To understand the operation and predict performance of EIS biosensors, electrical equivalent circuit (EEC) models are frequently used. The Randles equivalent circuit is the most frequently used model for describing the impedance response of electrochemical systems, including impedimetric biosensors [182].

The Randles model describes the impedance of such an electrode as a function of the frequency of an applied sinusoidal voltage [183]. The circuit model, shown in **Fig. 2.3**, is comprised of four elements: the ohmic resistance of the electrolyte solution (R_s); constant phase element (CPE) is a generalized capacitance element that can account for non-ideal capacitive behaviour of the biosensor, such as surface roughness or heterogeneous charge distribution; the Warburg impedance (W) due to the diffusion of the chemical reactants in the solution; and the faradaic charge transfer resistance (R_p). The CPE is a generalization of a capacitor that takes into account non-ideal behaviours of the electrode surface, such as surface roughness or incomplete coverage of the bio-recognition element. The charge transfer resistance and Warburgs impedance are used to represent the impedance of a faradaic reaction and therefore not included in the Randles model for a non-faradaic impedimetric biosensor.

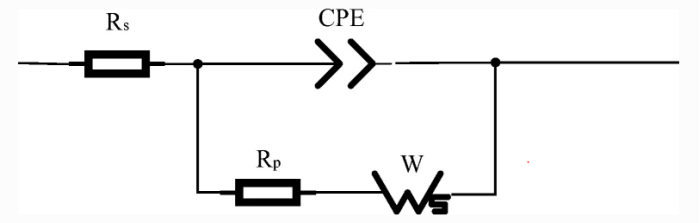

Figure 2.3. A Randles equivalent circuit model.

The basic Randles model can be adapted for a non-faradaic impedance biosensor by the inclusion only of circuit elements that account for the specific behaviour of the biosensor.
The electrical double layer element C_{dl} is often used to describe the capacitive behaviour between the electrode and electrolyte solution interface. This can be further expanded to show the contribution of the individual immunoassay elements, such as a linker molecule, receptor molecule and target antigen [184].

In previous literature, a number of authors have adapted the Randles model to decouple the faradaic and non-faradaic responses by producing distributed resistor and capacitor equivalent circuits. For example, Jacobs *et al* [171] developed a model in which they compared the electrical properties of two types of sputter-deposited ZnO thin films, to help understand the influence of ZnO electrical parameters on the sensor's performance. Tanak *et al* [84] fitted a modified Randles equivalent circuit to study the nature of the impedance spectra of interdigitated gold electrodes fabricated on a ZnO thin film. This showed an increase in double layer capacitance with increasing concentration of the antigen due the capacitive binding effect at the electrode surface caused by the interaction between antibody and antigen binding [84].

2.3.2 Equivalent electrical circuit of the 1% ZnO/CuO nanoparticle biosensor

The modelling work described in this study considers the development of an EEC model of a biosensor structured as borosilicate glass layer separating the electrodes from a ZnO biocompatible sensing surface. The modelling approach involved the adaptation of the Randles equivalent circuit to provide a detailed representation of the structure of the nanoparticle based impedimetric sensor. In this modelling approach, the EEC model was built up in relation to the layers of the sensor structure as this provided a deeper understanding of the sensor operation and the sensor's layer-by-layer impedance contribution.

The biosensor structure comprises of the following layers (1) co-planar copper electrodes on a PCB substrate, (2) borosilicate glass layer, (3) a ZnO nanoparticle layer and (d) antibody layer on the ZnO nano-surface in contact with the buffer solution. Caspase-9 protein was chosen the antigen to evaluate the sensor's performance. The resistor and capacitor equivalent circuit, including the associated electrical components of the biosensor, provided a complete circuit model at 6 MHz, as show in **Figure 2.4**. Further details can be found in on biosensor construction can be found in Chapter 3.

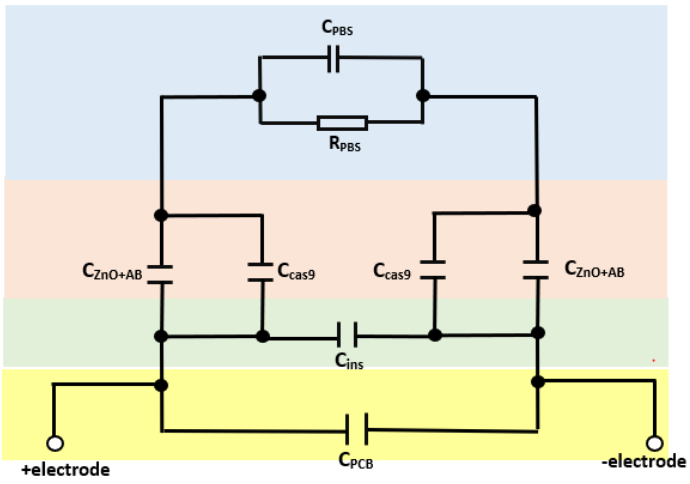

Figure 2.4. Equivalent circuit model for the ZnO-based impedimetric biosensor.

For modelling purposes a symmetrical system is assumed. The model includes the key elements of the Randles model for a non-Faradaic biosensor including the capacitance of the electrical double layer, which includes the capacitance of ZnO-Antibody layer (C_{ZnO+AB}) and capacitance of capase-9 (C_{cas9}) plus the resistance (R_{pbs}) and the capacitance (C_{pbs}) of the solution. The ZnO-Antibody interfacial impedance is modelled as a series connection with the PBS electrolyte impedance. The bulk PBS impedance is calculated and modelled as a parallel connected R_{pbs} and C_{pbs}. This part of the model is consistent with other studies regarding insulated biosensors [170,182,185]. The glass substrate placed between the two electrodes forms a parallel capacitance connection to that of the PCB substrate capacitance. The PCB FR4 and glass substrate are considered as dielectric materials with a relative permittivity, ϵ_r, of 4.7 and 5.5 respectively [186]. And with both substrates being dielectric, they would have a very high intrinsic resistance (greater than 10^6 Ω) thus the intrinsic capacitance of this material would be dominant over the frequency ranges tested in this study. Finally, the effect of antigen binding is represented as a parallel capacitance connected to the ZnO-

Antibody interfacial capacitance, as larger concentrations of target antigen in a sample will result in a greater biomolecular interaction on the interface, resulting in greater changes in relative dielectric permittivity, and thus contributing to a increase in interfacial capacitance [170]. The total interfacial capacitance can be written as:

$$C_{total} = C_{ZnO+AB} + C_{Cas9}$$

The resistive and capacitive components of the model were determined by the analysis of the real and imaginary parts of the measured impedance of the constituent layers of the biosensor, i.e. PCB, glass, ZnO nanoparticles, antibody functionalised ZnO in contact with PBS and finally, caspase-9 antigen. The model and experimental results show that the capacitive reactance (imaginary) was the dominant component from the impedance magnitude. The resistive (real) component of impedance magnitude was found to provide a negligible contribution to the impedance magnitude and thus was removed from the EEC model. Component analysis of the major contributors to the impedance output can be found in Chapter 4.

2.4 Summary

In this chapter, faradaic and non-faradaic impedimetric biosensors have been compared. Faradaic impedimetric biosensors rely on the transfer of electrons or ions between the electrode and the biomolecule of interest, resulting in changes in the electrical properties of the system that can be detected as a change in impedance. Non-faradaic impedimetric biosensors, on the other hand, detect changes in the dielectric properties of the electrode-electrolyte interface that result from the binding or interaction of the biomolecule with the electrode surface.

Additionally, the basic principles of impedance spectroscopy were also outlined, including the mathematical theory of impedance, Debye length, components within the electrical double layer and data analysis methods used for biosensor setups. An equivalent circuit model specific to the non-faradaic impedimetric sensor developed in this PhD has been presented. The modelling approach involved the adaptation of the Randles equivalent circuit to provide a detailed representation of the sensing approach and to show the capacitances and resistances associated with the constituent elements of the biosensor. The impedance behaviours of biochemical binding of capase-9 could be analysed using electrical equivalent circuit to quantify the concentration of caspase-9 in a capacitive non-faradaic sensing system.

In the following experimental chapters, an investigation to study the relationship between the impedance responses of sensor surface interactions and caspase-9 concentration is described. It includes the fabrication of ZnO/CuO nano-surfaces via colloidal dispersion using sonication, for caspase-9 detection. This investigation informs the design of experiments for the detection of caspase-9 from live CHO cell cultures using the ZnO/CuO based nano-surface sensor.

Chapter 3

Nanocrystal Bio-surface Fabrication

This chapter focuses on the development of the ZnO/CuO composite sensor surface for the detection of caspase-9 using non-faradaic impedance spectroscopy. The ZnO/CuO nanoparticle suspension was prepared using a simple sonication method to achieve colloidal dispersion and cast on to borosilicate glass cover slips. The morphology of the nanocrystal surface and thickness of the surface were characterised via scanning electron microscopy. Anti-caspase-9 antibodies were immobilised onto the sensing area via physical adsorption. In order to determine the successful functionalisation of the sensor surface, an ELISA-based colorimetric assay was used to biochemically characterise antibody binding on the sensor surface. Impedance spectroscopy was used to measure the binding interaction between active caspase-9 and antibody. Anti-cleaved caspase-9 antibody was used to functionalise the biosensor surface to detect the active caspase-9 rather than other types of caspase-9. Optimal antigen incubation times were determined by measuring the change in output signal over time. The impedance spectra and impedance changes were compared for surfaces functionalised with different antibody concentrations to determine the optimal antibody loading concentrations. This chapter provides details of the optimisation process and initial testing of the nanocrystal biosensor and a justification for the methods used in the subsequent chapter.

3.1 Introduction

The benefits of metal oxide nanomaterials and their applications in biosensing were highlighted in chapter 1. For the caspase-9 sensor developed in this research work, zinc oxide was used due to its low cost, chemical stability, protein binding ability, surface area to volume ratio and semiconductor properties [133].Furthermore, the biocompatible nature of ZnO nanostructures makes it a suitable choice for surface functionalization and interfacing with chemical/biological compounds at various temperature and pH levels [133] Copper oxide was added to improve sensor performance as counterparts of n-type ZnO through the formation of p-n junctions [89,137].

Biosensor development includes the deposition of nanoparticles onto the sensing surface, which is a crucial step for obtaining not only improved performance from the constructed biosensor, but also improved stability, reproducibility and ease of mass production. Various deposition methods have been used to create a successful uniform and precise layer of ZnO and ZnO/CuO nanoparticles on the biosensor surface, including physical deposition [143], chemical deposition [140] and hydrothermal methods [133]. The thermal evaporation technique is the most frequently used method for depositing thin films, as it has low contamination rates and a well-controlled deposition rate [187]. However, this technique is disadvantageous for large scale manufacture as the process is expensive due the requirement for high temperature and high vacuum conditions [187].

As mentioned in chapter 1, the proposed biosensor contains an insulating glass layer sandwiched between the sensing layer and the electrode surface. This physical separation

between the biorecognition layer and the electrode surface allows the extraction of non-faradaic impedance measurements independently since the charge transfer of electrons due to redox reactions at the electrode surface is prevented. From a practicality perspective, this insulating layer can be removed after use and replaced with another fully functionalised sensing layer. This is advantageous, as the original electrode surface is not exposed to the analyte solution and can be re-used without the need for electrochemical cleaning or other cleaning methods required for faradaic sensors [188]. Due to the replaceable nature of the insulating surface, two inexpensive and simple deposition methods were explored in this study; spin coating and drop casting.

Both spin coating and drop casting are excellent techniques for the deposition of high solubility polymers that can form homogenous films, which are important for obtaining large coverage areas and reproducible devices [187]. However, the ZnO and ZnO/CuO nanoparticles used in this study is insoluble in water and is only soluble under very acid conditions [143]. This means the ZnO and ZnO/CuO nanocrystals tend to aggregate and precipitate in water. Thonglerth *et al.* [189] attempted to stabilize ZnO nanoparticles as water-based dispersions using dispersion agents such as oleic acid and polyvinyl alcohol. The results revealed that 1% w/v content of modified ZnO nanoparticles with sonication at 30 minutes produced the highest dispersion stability, whereas higher concentrations and extended sonication led to precipitation and re-agglomeration [189]. This finding is consistent with the results from previous study that compared different concentrations of ZnO dispersions in water to produce ZnO-polyester composite surfaces [190]. Rimbu et al. [190] demonstrated that larger concentrations of ZnO (above 3%) led to agglomerations and diminished surface coating quality. This problem of aggregation could be mitigated through sonication and vigorous shaking. For example, ultrasonication is very effective in breaking particle agglomerates as

the shock force breaks the nanoparticle clusters yielding a dispersed mixture of nanoparticles [191]. The need for nanoparticle synthesis and characterisation can be removed by purchasing ZnO nanoparticles of predefined sizes and shapes. Colloidal dispersion techniques, such as ultrasonication and sonication, can ensure well characterised and homogenous surfaces are created in an inexpensive manner.

In this chapter, preliminary results are presented of a biosensor that is fabricated using a colloidal dispersion technique, incorporating sonication, to create a ZnO/CuO composite nanocrystal surface. Both drop-casting and spin coating techniques were tested and compared to determine the optimal deposition method. Surface morphology and biosensing performance of ZnO/CuO composite surfaces and ZnO only surfaces were compared. Impedance spectroscopy was used to measure antigen-antibody binding on the surface.

3.2 Materials and methods

The following materials were used in the preparation of the biosensors:

- Zinc oxide nanoparticles (99.9 +%, 80-200 nm) and CuO nanoparticles (99.5 +%, width: 10-30 nm, length: 200-800 nm) from US Research Nanomaterials Inc. Houston, TX, USA).
- polyclonal Rabbit anti-cleaved caspase-9 IgG (ab2324, Abcam Ltd. UK),
- monoclonal mouse anti-caspase-9 IgG (sc-56073, Santa Cruz Biotechnology, Inc., USA), caspase-9 (CC120, Sigma-Aldrich),
- Goat anti-mouse IgG:HRP (Bio-Rad Laboratories Ltd, UK).

Phosphate buffered saline (PBS, pH 7.3 ± 0.2 at 25 ^{o}C) was purchased from Merck. The PBS buffer was diluted to 0.01 M adjusting the pH to 7.4.

3.2.1 Nano-surface preparation

Accurately weighed quantities of ZnO nanocrystals and CuO nanocrystals were added to double deionised water to make a range of concentrations (g/mL) of ZnO/CuO suspensions: 1% ZnO (made by adding 1 g of ZnO to 100 g of water), 2% ZnO/1% CuO, 1% ZnO/1% CuO, 1% ZnO/2% CuO. The suspensions were stirred at room temperature for 1 hour and then ultra-sonicated in pulsing mode (20s off/20s on) for 5 minutes using a 13 mm probe (Sonics & Materials. Inc.) at 100 watts. The sonication process generates heat and thus the suspensions are place in beakers of ice to allow the fluid to cool down between cycles. Compared to Cao's methods, this method has a lower "off" time of 20 seconds compared to 4 minutes which should decrease the likelihood of the nanoparticles re-agglomerating. Glass substrates were initially cleaned via sonication in ethanol for 10 minutes. 250 µL drops of the suspension were cast onto clean glass coverslips (width: 22 mm, length: 22 mm, thickness: 0.13-0.17 mm, Cole-Palmer, UK) to make ZnO/CuO nano-surfaces. Finally, they were dried in an oven at 50^{o}C for 4 hours, then stored in a dry atmosphere with silica gel for up to 2 days.

3.2.2 Morphological characterisation of sensor surface

The ZnO/CuO nanocrystal surfaces were examined using a FEI Quanta FEG 650 field emission scanning electron microscope (ESEM) with a Low vacuum Secondary Electron (LFD) Detector operating in low vacuum mode. The surface morphology of ZnO coated nano-films and ZnO/CuO coated nano-films were analysed. To perform the SEM analysis,

samples were mounted on an aluminium stud and coated with a thin layer of Au using an Emscope SC500 Gold sputter unit prior to analysis. The cross-sections of the nanofilm were also examined using an Everhart-Thornley Detector (ETD), operating in high vacuum mode. A grayscale profile of each image was created using ImageJ software. (A grayscale value (0 - 255) is a single number that represents the brightness of the pixel.) The light areas indicate charge on the surface in the SEM with higher points reflecting electrons and accumulating charge more easily. This means that "deeper" areas do not reflect or accumulate charge as readily and consequently have lower values. Grayscale value plots derived from the images of SEM results were plotted by placing a diagonal line across the image using ImageJ software. Image surface areas were compared within a 3 µm by 3 µm scan area using the ImageJ surface plot plugin. The total surface area and mean roughness (R_a) within the scan region for different nano-surfaces were compared.

3.2.3 Caspase-9 sensor fabrication

Rabbit anti-cleaved caspase-9 IgG (ab2324) was stored and diluted in 0.01 M PBS buffer. The sensing area (10 mm x 4 mm) of each ZnO-CuO nano-surface on glass was defined by tape. Subsequently, 50 µL (2 µg/mL) of antibody solution was dropped on to the sensing area and incubated for 3 hours at room temperature. Surfaces were washed three times with PBS buffer before the addition of 40 µL of 5% non-fat milk to block the surface and inhibit nonspecific interactions. The biosensor was then dried in a vacuum desiccator with silica gel at 4^{o}C overnight for 18 hours. A simplified diagram of the steps of the fabrication and measurement method are shown in **Fig. 3.1a**. A cross-sectional illustration of the biosensor components as the sensing surface is shown in **Fig. 3.1b**.

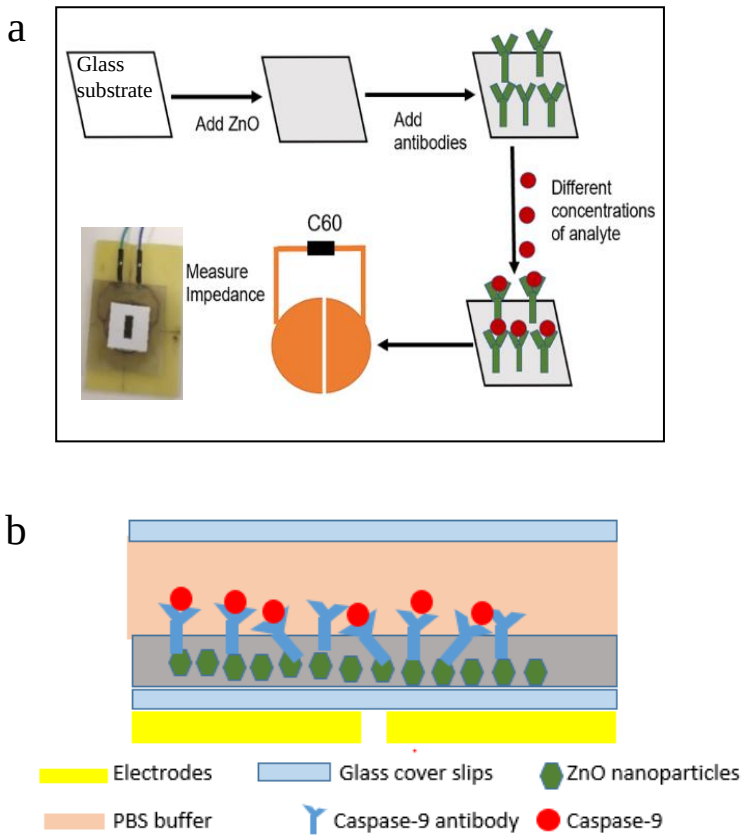

Figure 3.1. (a) Schematic illustration of biosensor fabrication and sensing: The ZnO/CuO nanoparticles were cast onto the glass substrate, then the antibody were added to the ZnO/CuO surfaces and dried at 4 ^{o}C overnight. Different concentrations of caspase-9 were prepared and added to the immobilised antibody on the nanocrystal surface. Sensors were placed on the electrode and impedance was measured. **(b)** Cross-sectional illustration of the biosensing surface and the biorecognition interactions between anti-cas9 and caspase-9.

3.2.4 Surface uptake of antibody

Antibody uptake on ZnO-CuO nano-surfaces was quantified using an enzyme based immuno-assay (**Figure 3.2**) . Using the ZnO-CuO nano-surfaces prepared as described previously, 50 µL (2 µg/mL) drops of mouse anti-cas9 IgG (sc-56073) were cast onto the defined sensing

area. The surfaces were then incubated for 3 hours and then washed to remove unbound antibodies. The surfaces were incubated with 5% non-fat milk for 1 hour and washed again. The sensor was allowed to dry in a desiccator overnight. Following a thorough wash to remove any unbound antibody, 100 µL (1 µg/mL) of Goat anti-mouse IgG:HRP was added to the surface and left for 1 hour at 25^{o}C. Then, the surfaces were washed three times with PBS buffer to remove any unbound antibody. 200 µL of TMB (tetramethylbenzidine, Alfa Aesar) solution was added as the enzyme substrate to generate a coloured product. Finally, 100 µL of the TMB solution were extracted from the sensor surface and mixed with 100 µL of TMB stop solution (Merck) inside 96 well plates. The intensity of the coloured product was read at 450 nm using a microplate reader (SpectraMax ID5, Molecular Devices). The relative amounts of surface bound antibody were defined by the optical density of the tests of the different sensor surfaces.

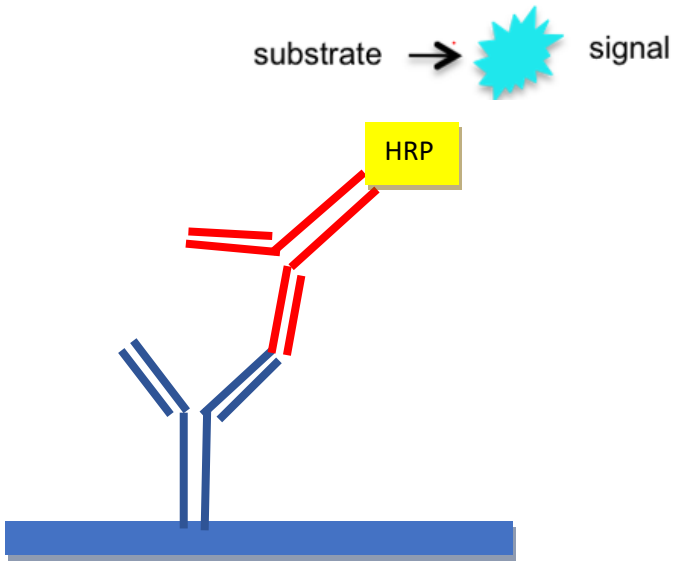

Figure 3.2. Schematic illustration of the ELISA-based assay. 1) Coating the sensor surface with mouse IgG. 2) Add the secondary antibody conjugated to enzyme (rabbit anti-mouse). 3) Add the substrate which is then converted to a measurable luminescent signal.

3.2.5 Impedimetric sensing of caspase-9

The nano-surface biosensors (fabricated as described in **Section 3.2.3)** were positioned above a pair of D-shaped copper electrodes (22 mm length, 10 mm width each), with an inter-electrode gap of 0.1 mm (**Fig. 3.3a**), which were fabricated on a printed circuit board (PCB) to perform impedance measurements. The sensor was aligned in a way that the rectangular sensing area (10 mm x 4 mm) is positioned directly above the gap (**Fig. 3.3a**). A cross section of the biosensor is illustrated in **Fig. 3.1**.

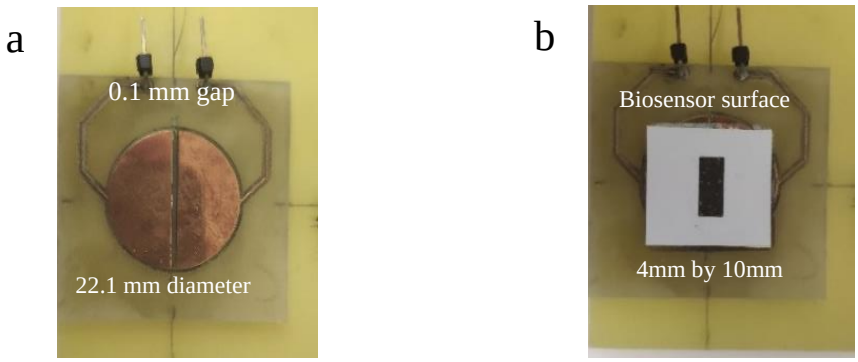

Figure 3.3. Electrode setup and schematic of the biosensor (a) pair of D-shaped copper electrodes (22.1 mm diameter for each electrode). (b) Sensor setup showing this sensing area (10 mm x 4 mm) defined by white tape.

A Cypher Instruments C60 Impedance-Amplitude-Phase Analyser was used to measure the impedance of the nano-crystal surfaces (**Figure 3.1**). The frequency was scanned from 10 Hz to 4 MHz at a voltage of 2 Vpp and a DC offset of 0.9 mV, with 300 test points. The impedance plots were analysed by Cypher Graph V1.21.0, Impedance Amplitude and Phase Analyser graphing application software. Impedance spectra of ZnO nano-surfaces were acquired on 10 independent measurements at each of the three concentrations (g/100 mL) of ZnO/CuO used to prepare the surface.

Caspase-9 was prepared at a range of concentrations: 0 (PBS only), 0.1, 0.25, 0.5, 1, and 2 U/mL. In terms of caspase activity, 1 U/mL equates to the amount of protein in the solution that will give 1 unit of activity. According to the manufacturer's technical specification state one unit of activity contains approximately 0.135 – 0.4 µg (0.27 µg on average) of caspase-9. The molecular weight of caspase-9 is 35 kDa. Therefore, the concentrations tested in this study ranges from: 0, 1 nM, 2 nM, 4 nM, 8 nM and 16 nM. 75 µL of each concentration of antigen was added to the biosensor without wash. Following set incubation times, the impedance was measured without wash. Impedance measurements were also made at each stage of the assay process, namely: (1) On the nano-crystal surfaces with dry antibody; (2) Immediately after adding 50 µL of different concentrations of antigen and (3) at 5-minute intervals until 20-minute incubation time had passed. In order to plot logarithmic concentrations of caspase-9, the measurement of PBS buffer only with no caspase-9 (control), was defined as 0.01 U/mL caspase-9 (rather than 0 U/mL). The difference in impedance was derived by subtracting the impedance value of controls for each impedance measurement of the caspase-9 assay at the various concentrations. The calibration curve was plotted based on impedance change versus logarithmic concentrations of detection caspase-9.

3.3 Results and Discussion

3.3.1 Surface morphology characterisation

Initial experiments involved the imaging of the surface morphology and validation of surface chemistry. Scanning Electron Microscopy (SEM) was used to analyse the surface morphology. From the SEM images, the 2% ZnO/1% CuO suspension (**Fig 3.4a**) produced a more complete covering of the glass surface compared to the 1% ZnO/1% CuO suspension (**Fig 3.4b**). This was to be expected since larger mass of ZnO was applied. At 40000 x magnification, smaller flake-like structures (width 30-40 nm) can be observed surrounding ZnO particles (**Fig 3.4c**). The columnar wurtzite structure of ZnO nanoparticles (width 80-200 nm) can observed in **Figure 3.4e**. Several voids can be observed within this structure which can serve as additional sites for biomolecular interaction.

The film-forming technique used in this study to produce the nanocrystal films was drop-casting. The dispersed colloidal nanoparticle mixture was cast on the glass substrate to allow the evaporation of the solvent. This method was deemed more suitable and effective compared to the spinning coating technique for the following reasons: 1) It is simple as it does not require specific equipment, 2) spin coating leads to significant wastage as the majority of mixture (around 95- 98%) is flung of into the bowl and not used [192], and 3) whilst spin-coating can cover the entire surface evenly, it was not required to cover the glass substrate completely in this study as only the central region was functionalised [193].

The cross-sectional images of the 2% ZnO/1% CuO nanocrystal film, shown in **Figure 3.4d**, revealed an average film thickness of around 10.5 μm. The 1% ZnO/1% CuO film measured

an average film thickness of around 9.5 µm (**Fig. 3.4f**). In all samples, the surface is rough as evidenced by the presence of peaks and valleys throughout the structure. The results are consistent with previous study from Cao *et al.*[111], in which a ZnO/CuO oxide composite surface for use in an impedimetric biosensor was studies. The nano-surfaces were prepared with a simple colloidal dispersion technique involving sonication [111]. The simple colloidal dispersion technique has been shown to produce highly ordered and homogeneous ZnO/CuO nano-surfaces, after characterisation by SEM and atomic force microscopy (AFM) [111].

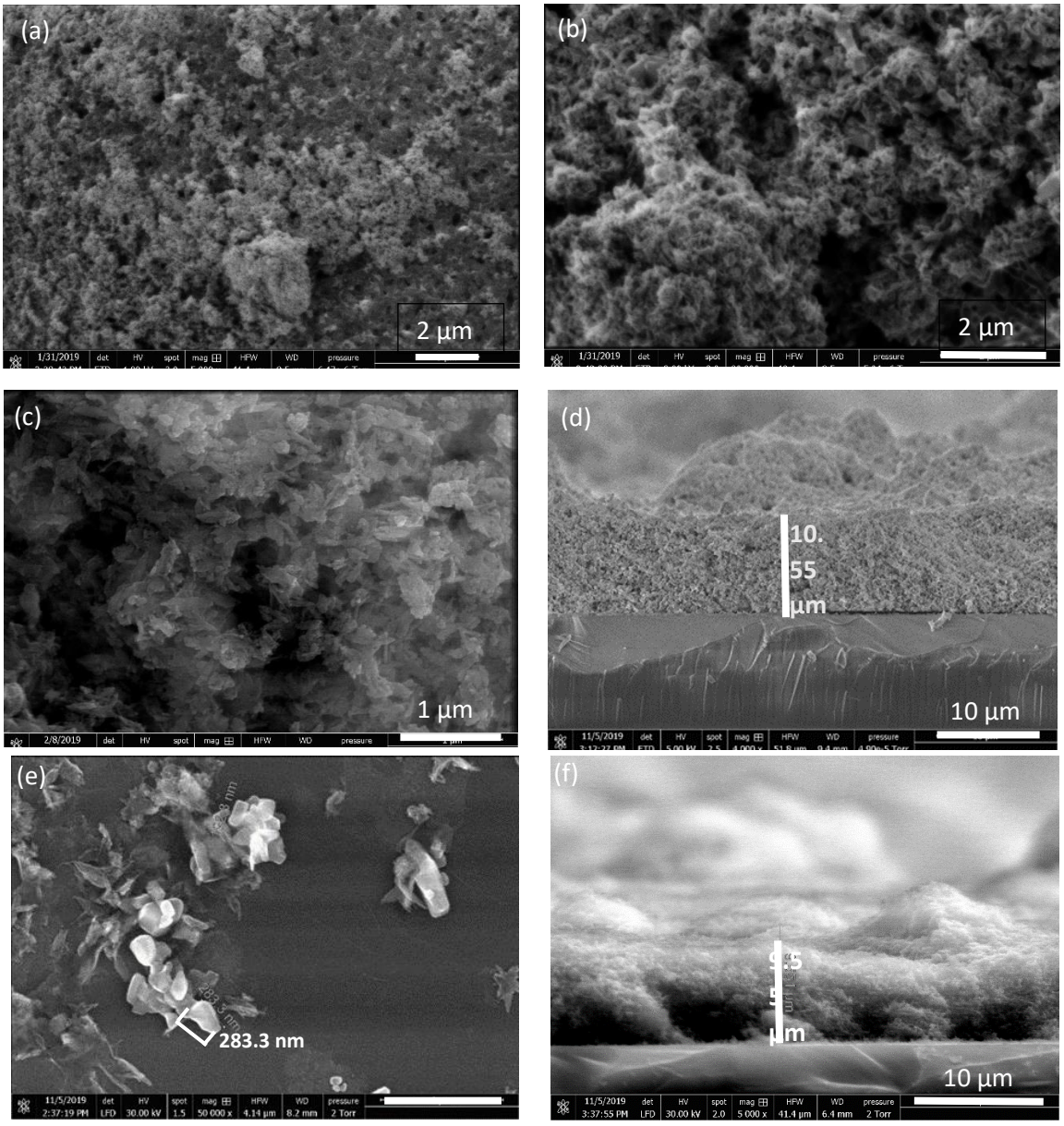

Figure 3.4. SEM images for ZnO/CuO nano-surfaces on glass via suspensions at different concentrations (g/100 mL) of ZnO/CuO nanoparticles: (a) 2% ZnO/1% CuO; (b) 1% ZnO/1% CuO. (c) 1% ZnO/1% CuO at 40000 x magnification. (d) cross sectional image capture using ETD detector capturing the thickness and surface roughness of the 2% ZnO/1% CuO nano-surface. (e) 1-1 ZnO-CuO at 50000 x magnification. (f) cross-sectional image of the 1% ZnO/1% CuO nano-surface. Nanofilm height is estimated.

3.3.2 Surface roughness characterisation

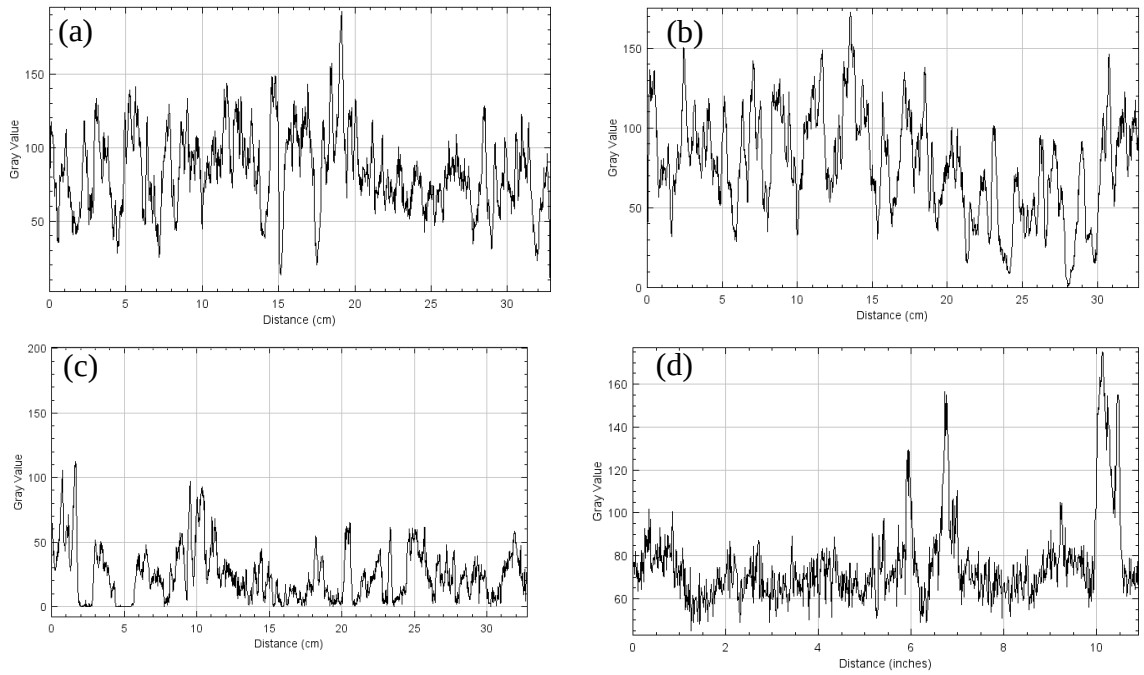

Figure 3.5. Plots of grayscale profiles along a diagonal line within images (5000 x magnification) for nano-surfaces made using three different combinations of ZnO and CuO: (a) 2% ZnO/1% CuO; (b) 1% ZnO/1% CuO; (c) 1% ZnO; (d) 1% ZnO/2% CuO.

A grayscale profile was generated for each SEM image using ImageJ software. The lower values of grayscale represent darker regions in the image which is caused by holes or voids within the nanocrystal film. Whilst, the higher grayscale values represent lighter areas with an abundance of ZnO/CuO nanocrystals. The grayscale profile plot of 2% ZnO/1% CuO (**Fig. 3.5a**) and 1% ZnO/1% CuO (**Fig. 3.5b**) show a large amount of fluctuations in grayscale values between low and high values, indicating that the surface is rough, with many voids and peaks across the nanocrystal surface. In comparison, the profile plot of 1% ZnO (**Fig.**

3.5c) shows a narrower range of grayscale values, indicating that the surface is smoother, with less valleys and peaks across the surface. The lower grayscale values and in some areas where the grayscale was close to zero is reflective of a lower density nanocrystal covering of the surface with areas of incomplete coverage of glass substrate (**Fig 3.5c**).

The surface area (μm^2) and mean roughness (R_a) of the different nano-surfaces are shown in **Table 3.1**. The 1% ZnO/1% CuO and 2% ZnO/1% CuO composite surface shows the largest surface area. This is expected as CuO nanoparticles are smaller than ZnO nanoparticles and they exist as flake-like structures with very high surface area [194]. Interestingly, the 1% ZnO/2% CuO nano-surface displayed similar surface area and roughness values (**Table 3.1**). This finding is consistent with results from previous work from Cao *et al.*[111], showing the smaller CuO flakes filling in the voids between ZnO nanoparticles, reducing the overall surface area[111]. It was speculated that this was due to the charge-based attraction between ZnO (n-type) and CuO (p-type) nanomaterials [111].

Table 3.1. Image surface area comparisons of various nanosurfaces, analysed by ImageJ Software.

Type of nano-surface	Image surface area (μm^2) of 3 μm scan size	Mean Roughness (Ra) (nm)
1% ZnO	13.2	85.3
1% ZnO/1% CuO	14.8	94.2
2% ZnO/1% CuO	14.5	95.5
1% ZnO/2% CuO	12.9	83.4

A simple mathematical approach was used estimate the surface area of the 1% ZnO nano-surface. The volume of the nanofilm was calculated using $V = \frac{1}{4}\pi d^2 h$, where d is the diameter and h is the height of the film. This volume is associated with the film formed from drop-casting 200 μl of 1% ZnO suspension. Therefore, each film surface contained approximately 2 mg of ZnO. The specific surface area (SSA) of ZnO nanoparticles is s= 4.8 - 6.8 m^2/g (information provided by the manufacturer). The SEM scan range x^2 = 3 and mean roughness R_a = 85.3 nm were derived from ImageJ analysis software (from **Table 3.1**). The SEM detection volume was calculated by $v = x^2 \cdot R_a$, which assumes the ZnO nanoparticles were evenly distributed among the film. Using the values explained above, the surface area of the nanoparticles could be approximated using the following equation:

$$SSA = M \cdot s \cdot \frac{4x^2 R_a}{\pi d^2 h} \tag{3.1}$$

Using this equation, the approximate surface area on the SEM detection volume is between 12.25 – 18.78 μm^2. This matches the results derived from the software at 13.2, providing evidence that nanoparticles are distributed evenly throughout the film and majority of the nanoparticles remained on the surface throughout the fabrication process.

Previous authors have shown that greater surface roughness is beneficial to the performance of biosensors. For example, Perry et al.[195] artificially introduced microcavities onto platinum electrode surface. This increases the electrode surface area, providing additional binding sites, which in turn provide faster rates of redox reactions relative to the smooth crystal faces [195]. Kang et al.[196] found the introduction of nanocavities on electrodes led to improved sensing performance through the amplification of the electrochemical signal. They found that redox rate increased significantly where the molecules are confined within nanoscale cavities of the electrode, and this is known as the nanoconfinement effect [196].

In conclusion, the addition of CuO has contributed to increased roughness, thus increased surface area for biological binding and reduced the detrimental charge screening effects, whilst ensuring minimal regions with exposed glass substrate. However, higher concentrations of CuO did not significantly improve the surface area or roughness but instead the CuO appeared to lay flat on the ZnO. This was speculated to be due to the Coulomb attraction between the two materials. Based on the surface area and surface values, the 1% ZnO/1% CuO nano-surface was selected as the final concentration going forward as the additional ZnO in the 2% ZnO/ 1% CuO provided a minimal improvement in the surface roughness and displayed slightly worse total surface area.

3.3.3 Antibody functionalisation and validation

To validate the immobilisation of proteins on the ZnO-CuO nano-surfaces, an enzyme linked immunosorbent assay (ELISA) was performed (Section 3.2.4). Here, 200 ng (50 µL of 4 µg/mL) of anti-cas9 (mouse IgG) was added to the ZnO-CuO composite surfaces and a secondary antibody conjugated with horse radish peroxidase (HRP) was used to detect the specific protein binding on the nano-surfaces. The binding events between mouse anti-CRP IgG and HRP-labelled rabbit anti-mouse IgG were quantified by measuring the absorbance signal. As it is shown in **Figure 3.6**, there was an approximately fourfold difference in absorbance in samples incubated with the primary antibody compared to samples that were not. A higher absorbance value corresponds to the conversion of 3,3′,5,5′-Tetramethylbenzidine (TMB) to coloured product catalysed by the HRP conjugated to the secondary antibody and indicates the primary antibody is correctly immobilised onto the sensor surface. In addition, the 1% ZnO/1% CuO and 2% ZnO/1% CuO nano-surfaces displayed slightly higher absorbance signals compared to the 1% ZnO surface, further evidencing the increased surface area for biological binding made possible with the addition of CuO. The absorbance values associated with 2:1 ZnO/CuO surface were higher than the 1:1 ZnO/CuO surface, this could be due to the increased surface area on the sensor surface provided by the additional ZnO nanoparticles which forms cavities and ridges for the antibodies to bind to. The test also showed that non-specific absorption can be avoided by blocking the membrane with 5 % non-fat milk because as barely any signal could be observed from samples that did not contain the primary antibody. Thus, the blocking and wash strategy was applied to the construct the final nanocrystal sensor.

The isoelectric point is the pH at which the protein has no net charge. The high isoelectric points of ZnO (IEP~9.5) [197] and CuO (IEP~10) [198] enable stable immobilisation of biomolecules with lower IEP through electrostatic interaction. In contrast, the caspase-9 IgG1 antibodies used in this study typically have a IEP between 6.5 – 8.5 and are negatively charged at physiological pH [199]. Therefore, biomolecules can be readily immobilised on a positively charged ZnO through strong electrostatic interactions.

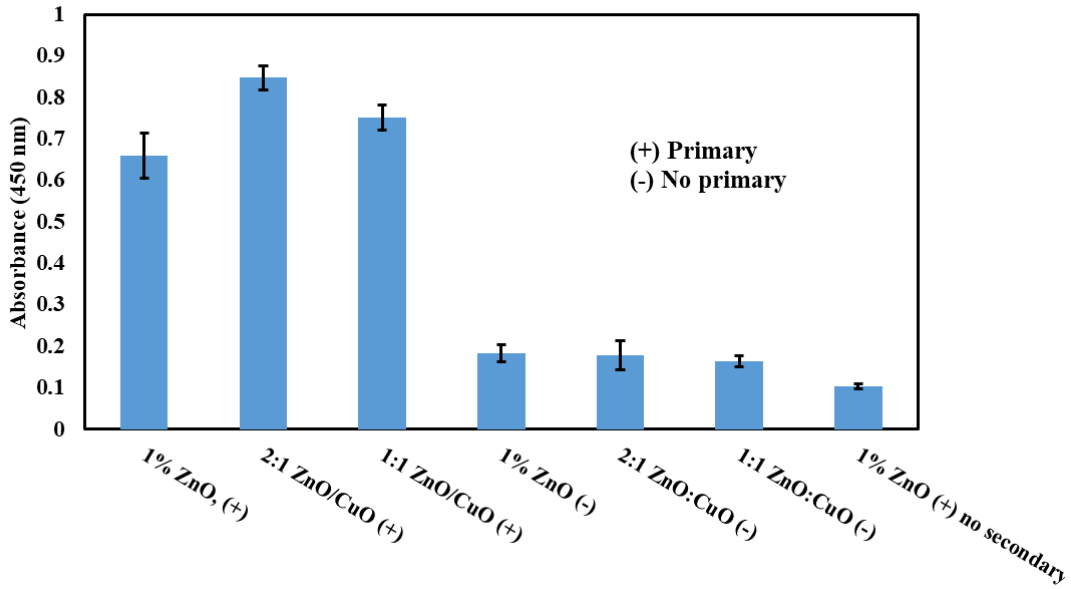

Figure 3.6. Validation of antibody immobilisation. Bar chart of anti-cas9 immobilisation on nano-surfaces expressed by colour formation at 450 nm from HRP-TMB reaction. Standard error bars are shown (n=5).

3.3.4 Detection of caspase-9 using impedance spectroscopy

Following the characterisation of the functionalised sensor surface with SEM and colorimetric assays, the specific binding interactions of caspase-9 were measured with electrical impedance spectroscopy. Impedance spectroscopy is a well-established approach for the analysis of complex biological liquids [200,201]. The sensor detects variations in complex impedance, induced by dielectric constant change. For the biosensor construction investigated in this work, the sensor response is mostly gained from a capacitive component of the complex impedance [201]. This is due to the glass cover slip preventing direct dc current between the electrodes. The capacitance arises when an electrode is immersed in an electrolyte solution and a voltage input in applied to measure the capacitance. In this condition, charged species and dipoles will be oriented on the electrode/solution interface, generating the previously mentioned electrical double layer capacitance, a physically measurable quantity very sensitive to interfacial change [202].

The addition of caspase-9 resulted in the decrease in impedance magnitude as shown in **Figure 3.7**. Caspase-9 protein has a basal isoelectric point (pI) of 5.73. The buffer solution containing salt ions and caspase-9 has a pH of 7.40. In this buffer environment, caspase-9 is dominated by negative charges. Consequently, when binding to the ZnO occurs, through capture by the antibody on the surface, there is an increase in negative charges with increasing caspase-9 loading and a decrease in the absolute impedance value. This observation concurs with previous literature where it is reported that, changes in surface dielectric, charge distribution or local conductance are induced when a protein binds to the bioreceptor displacing the water and ions from the surface [202].

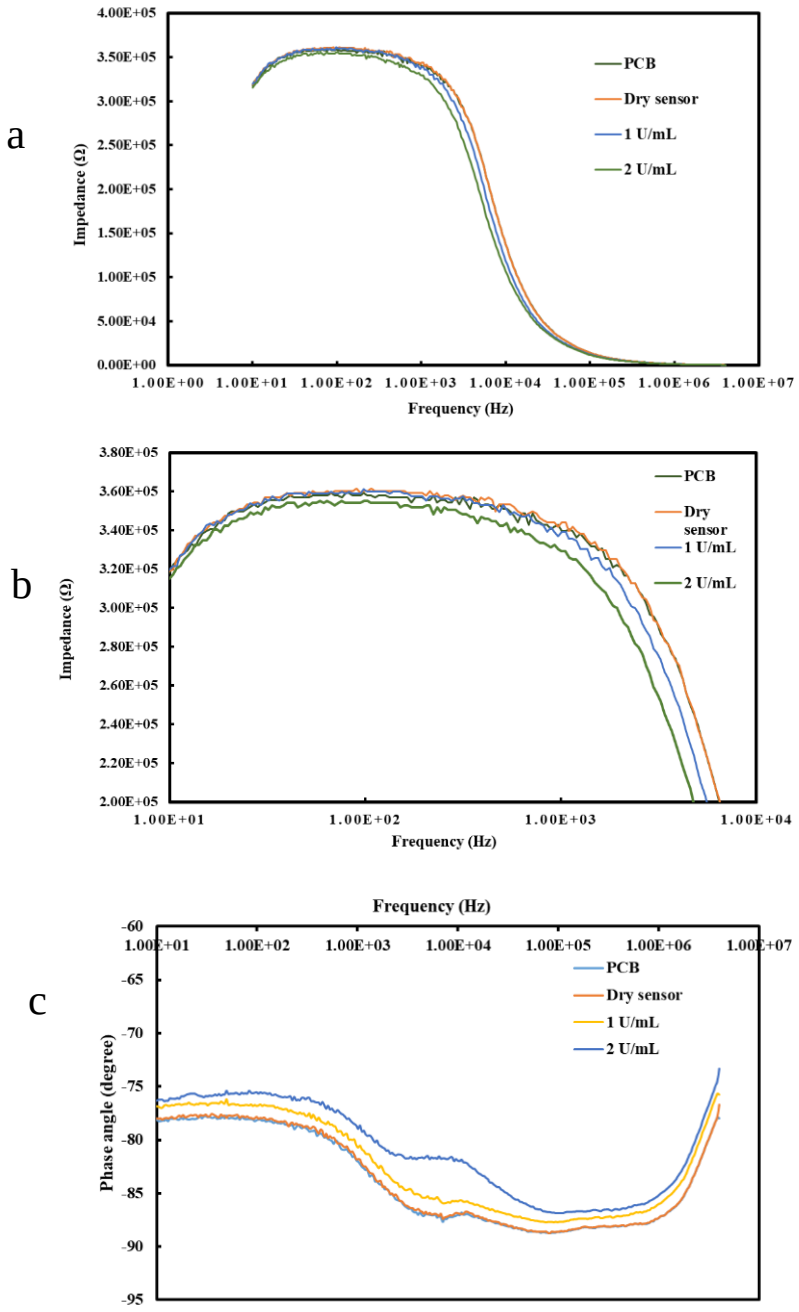

Figure 3.7. Frequency dependent impedance magnitude and phase responses (a) Impedance spectra (10 Hz to 4 MHz) of 1% ZnO/1% CuO surfaces containing 200 ng dry antibody, adding PBS and caspase-9 (1 – 2 U/mL caspase-9) for 10 minutes, (b) magnified impedance – 10 to 1000 Hz and (c) phase of impedance - 10 Hz to 4 MHz.

For the characterisation of the biosensor performance, successive cycles of the immersion of the fixed protein solution and the corresponding impedance magnitude (|Z|), phase and capacitance measurements were performed for each caspase-9 concentration (0.1, 0.25, 0.5, 1 and 2 U/mL). From the Bode plots, the greatest differences in impedance magnitude between the dry sensor, 1 U/mL and 2 U/mL caspase-9 solutions are observed at frequencies below 10000 Hz (**Fig. 3.7b**). This concurs with results from literature. For example, Jacobs et al [171] reported an impedimetric sensor for the detection of troponin-T, using ZnO as the transducer. They measured impedance at frequencies ranging from 100 mHz to 1 MHz, and found that most significant changes occurred around 100 Hz. The R^2 coefficient of determination plot revealed areas of high correlation at frequencies between 10 – 1000 Hz with R^2 scores greater than 0.9, although the correlations tend to be more sporadic at lower frequencies. This is most likely due to the fact that the sensor is a capacitive sensor, so DC and low frequency measurements will be unstable. After 10000 Hz, the R^2 score gradually decreases to 0.7. In the phase angle plots, a large amount of fluctuations in the signal was observed at the lower frequencies thus the correlation of determinations were generally low (~0.5). The sensor displays good capacitive behaviour with phase angles close to 90 degrees especially at the lower frequencies. A frequency of 1010 Hz was selected for the calibration plots, because at this frequency, the signal began to stabilise and a significant statistical difference (2σ) in impedance between the buffer measurement (0 U/mL) and the first sample (0.1 U/mL) was calculated.

3.3.5 Determining the optimal antigen incubation time

To determine the optimal antigen incubation time, measurements were performed on 1% ZnO/1% CuO nano-surfaces functionalised with antibody and incubated for 5, 10, 15, 20 minutes. **Figure 3.8** shows that incubation time beyond 15 minutes does not greatly influence the impedance output, which suggests that the binding interaction between caspase-9 and the antibody occurs relatively rapidly. This finding concurs with the antigen incubation times reported in other immunosensors [143,203]. Some instability in the signal was observed at the highest concentrations of caspase-9 tested after 20 minutes of incubation, this could be due partly to the evaporation of the fluid droplet or nanoparticle degradation in the buffer solution (**Fig. 3.8**). In further parts of the study, 15 minutes was selected as the incubation time to allow for sufficient binding interaction to occur and additionally a glass slide was added after the addition of the sample to the sensor surface to prevent evaporation of the fluid.

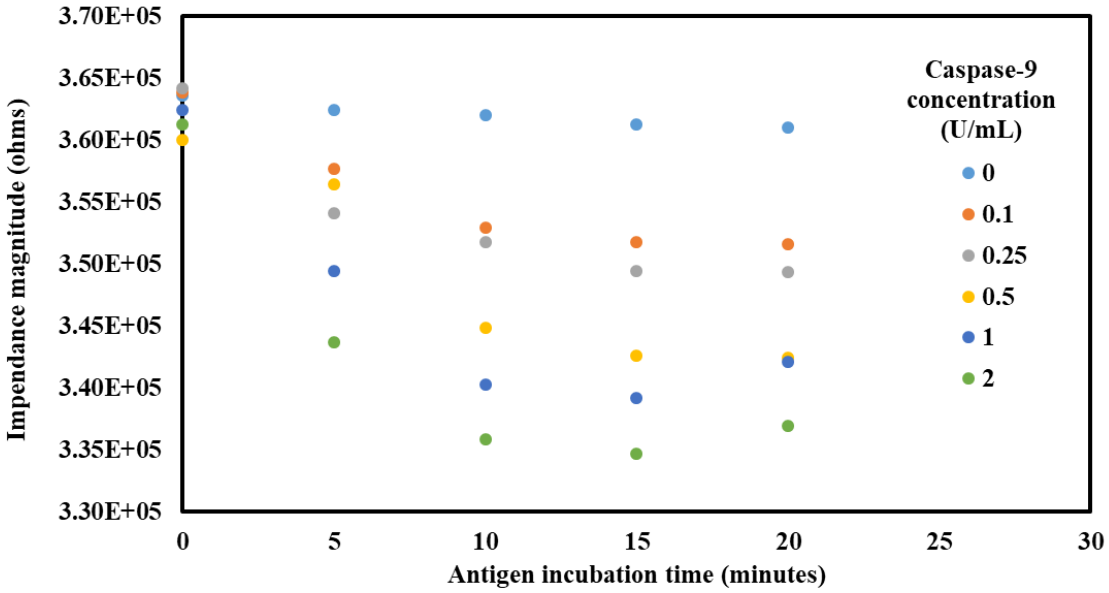

Figure 3.8. Impedance values (at 1010 Hz) from 1% ZnO/1% CuO nano-sensors, functionalised with 200 ng capture antibody with increasing concentrations of antigen: 0 – 2 U/mL for 5, 10, 15 and 20 minute incubation time.

3.3.6 Comparison of antibody loading

The sensing principle of the proposed sensor is based on changes in dielectric properties and/or charge distribution that is brought on by antibody–antigen complex formed on the surface of the sensor. The antibody concentration will affect the recognition capacity of the sensor and sensitivity. Thus, it is important to test and optimise the concentration of the antibody to further improve the analytical performance of the biosensor.

Increasing concentrations of antigen binds to a fixed amount of antibody in a dose dependent manner defined by the binding affinity up to the saturation point. It is speculated that there is increased charge accumulation on the nano-surface due to the bound antigen on the surface compared with the antigen in solution. Impedance comparisons of anti-caspase-9 loading (0 ng, 100 ng, 200 ng and 400 ng) with 2 U/mL caspase-9 on 1% ZnO/1% CuO nano-surfaces are shown in **Figure 3.9**. The results show that 200 ng loading of caspase-9 antibody provided an 80% increase in signal compared the signal produced by 100 ng antibody loading. The 400 ng loading resulted in a 10% increase in signal compared to the 200 ng but this was not statistically significant. The results indicate the signal is generated through the interaction between anti-caspase-9 antibodies and caspase-9 and increased antibody leads to greater number of available binding sites for biomolecular interaction. This result concurs with previous studies on antibody saturation. Lin *et al* [164] investigated the concentration of antibody required to saturate the sensor surface. They showed that an increase in antibody concentration from 1 µg/mL to 5 µg/mL lead to two-fold increase in saturation point [164].

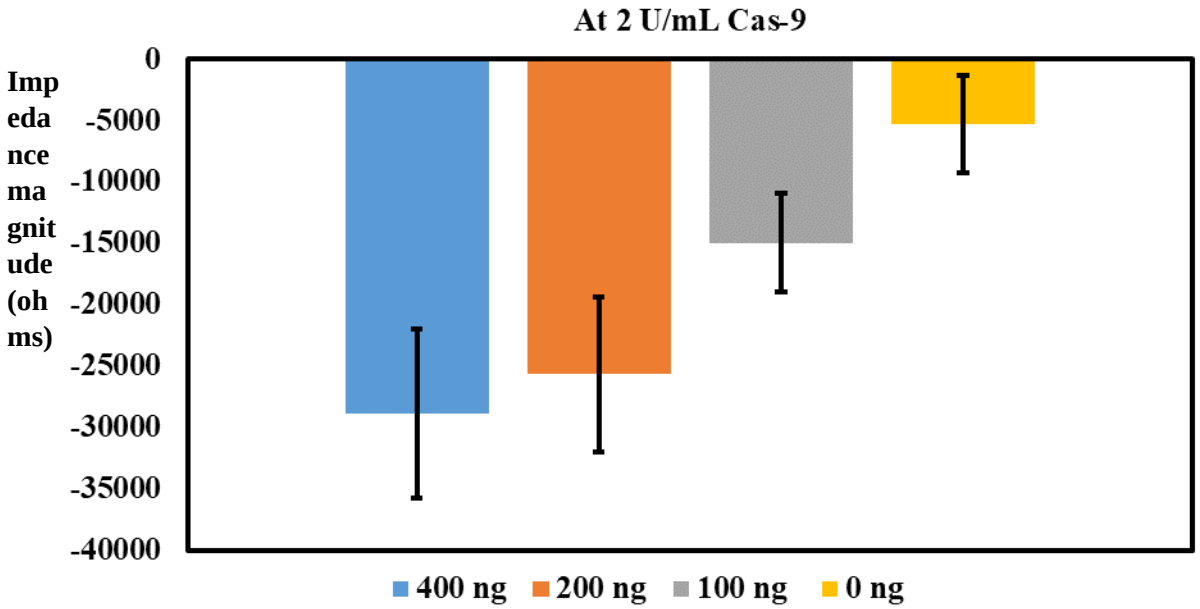

Figure 3.9. Comparison of caspase-9 antibody loading on 1% ZnO/1 % CuO nano-surface (n=3) at the frequency of 1010 Hz for the detection of 2 U/mL caspase-9.

To determine the effect of non-specific binding, impedance measurements of caspase-9 were taken on non-antibody-functionalised surfaces. Even with the addition of milk proteins to block the A small reduction in impedance magnitude can be observed on surface with 0 ng capture antibody when 2 U/mL caspase-9 was added (**Fig. 3.9**). This was likely a result of non-specific interactions at the ZnO/CuO surface-electrolyte interface caused by electrostatic interactions and other physical adsorption processes. However, despite this, the addition of recognition layer resulted in significantly larger signal outputs relative to the control, p = 0.02 (Kruskal-Wallis test). This result concurs with previous studies showing significantly reduced or baseline signals in the absence of capture antibodies [204].

Wen *et al.* [160]measured an increase in EIS value with the increase of antibody concentration until the EIS value reached a steady state. Cao *et al* [111]showed that the functionalisation of the

sensor surface with 200 ng of antibody resulted in a larger output signals compared with sensors loaded with 100 ng of antibody. This can be explained by the increase in available binding sites for antigen capture, resulting in greater protein loading on the surface and thus a greater signal is generated [111].

3.3.7 Sensor response to caspase 9

The modulus of the impedance differences (impedance value minus the blank) was employed to plot a calibration curve as shown in **Figure 3.10**. The impedance plot shows increasing values of the modulus of the impedance difference with increasing concentrations of caspase-9 for the 1% ZnO and 1% ZnO/ 1% CuO nanocrystal surfaces. A trend-line using the logarithmic regression model was applied to the plot and the R^2 values are also shown. The biosensor fabricated using ZnO–CuO showed a three-fold increase in signal for each concentration of caspase-9 compared with the pure ZnO. The ZnO-only biosensor displayed a decrease in impedance change with increasing caspase-9 concentration; however this was not significant up to 0.1 U/mL. In contrast, a significant difference in signal can be seen between 0.1 and 2 U/mL (**Fig. 3.10**). In addition, there was a significant difference between the blank and 0.1 U/mL ($p < 0.01$) (**Fig. 3.10**). A statistical analysis of the impedance values taken at a frequency of 1010 Hz demonstrated a high degree of reproducibility with a interassay %CV of 1.54%.

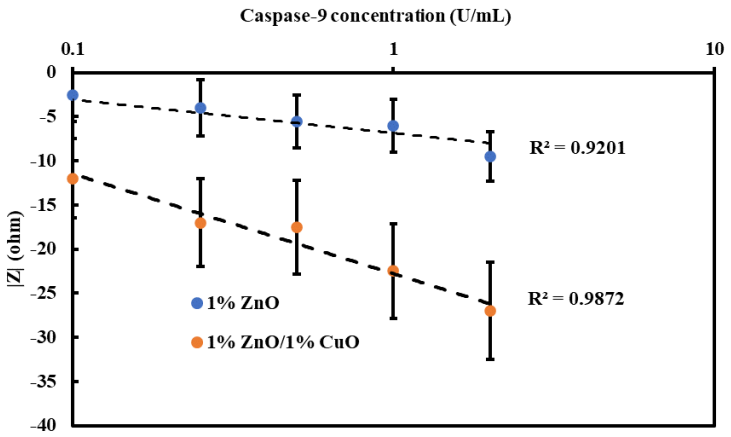

Figure 3.10. Impedance change in response to increasing concentrations of caspase-9 on 1% ZnO and 1% ZnO/ 1% CuO (n=3) with 200 ng of capture antibody. Because of logarithmic scale, the buffer reading is represented at 0.01 U/mL Cas-9 concentration.

Semiconductor materials, such as ZnO and CuO, will readily form an electrical double layer when they interact with the liquid electrolyte, resulting in charge accumulation at the interface region [89]. Furthermore, the binding interaction between the capture antibody and target biomolecule at the electrode surface results in a capacitive increase [200]. Therefore, the decrease in impedance can be interpreted as a result of increase in caspase-9 protein concentration. The sensitivity of the biosensor is influenced by specific capture of biomolecules at the sensor surface and rougher surfaces provide additional surface area for antibody capture and supress the charge screening effects. Surfaces fabricated using the 1% ZnO/1% CuO composite showed the higher roughness compared to the 1% ZnO surface. The slope of the trend-line was calculated to determine the sensitivity. The calibration curve of the composite surface displayed a three-fold enhancement in signal compared to the ZnO-only surface. The lower sensitivity of the ZnO-only surface could be associated with the reduced surface area for antibody immobilisation.

This improvement in the output with the addition of CuO could be attributed to an increase in the efficiency in the charge accumulation on the surface due to increase caspase-9 binding, Sabry *et al.* [205] showed that the enhanced sensitivity and recovery times in their gas sensor is due to the high aspect surface to volume ratio ZnO-CuO flower-like nanostructures which provides many sites to adsorb and desorb gas molecules. The contact of two different types of metal oxide semiconductors results in the formation of p-n junctions at the interface between the CuO and ZnO, leading to the decrease in a decrease in the resistance to the transient currents within the ZnO-CuO composite compared to ZnO only structures [205]. Batra *el al.* [125] demonstrated that the ZnO-CuO composite matrix-based biosensor have better conductivity compared to ZnO-only, which was attributed to the narrow band gap of CuO (1.2 -1.5 eV) and the ability to fill in the voids within the ZnO semi-conductor structure. Wang *et al.* [206] demonstrated increase sensitivity for carbon monoxide detection in the ZnO-CuO composite sensor compared to the ZnO only sensor. The initial resistance of the ZnO-CuO composite was higher due to the high resistance of the CuO phase in the composite and the formation of p-n heterojunctions [206]. When the ZnO-CuO heterostructures comes into contact with the analyte the measured resistance drop was more pronounced, and the recovery time was quicker (for the signal to return to baseline) [205]. Chitralekha *et al.*[207] demonstrated the dielectric constant in ZnO-CuO nanocomposites improved with increasing CuO content.

The detection limit for the ZnO/CuO nano-surface based caspase-9 biosensor was compared with other caspase biosensors (including the one example of caspase-9 detection) described in the literature. The 1% ZnO/1% CuO sensor demonstrated a linear range from 1 – 16 nM, with a limit of detection of 0.33 nM which is more sensitive than the caspase-9 and comparable

against many of the other caspase sensors mentioned in the literature (**Table 3.2**). Wen *et al.* [160] fabricated an immunosensor for the detection cytochrome c and caspase-9 during apoptosis for Hela cells. The caspase-9 biosensor had a linear range from 0.1 – 100 µM, with a detection limit of 0.02 µM [160]. The immunosensor was used for the detection of changed in the expression level of caspase-9 in the cytosol upon curcumin-induced apoptosis. The EIS values measured in the curcumin-induced Hela cells corresponding with the impedance values measured at the lower end of the calibration plots particularly between 0.1 and 5 µM of caspase-9 (3.57 µg/mL – 178.5 µg/mL) [160]. The results presented in this chapter demonstrate the nano-surfaces with ZnO and ZnO/CuO all show the ability for the sensitive detection of caspase-9.

Table 3.2 shows a selection of caspase related electrochemical biosensors reported in the literature. It can be seen that most of antigen detection ranges are in the order of nM or µM. It is worth noting most of the sensors are enzymatic sensors and require longer incubation times of around 1 hour. However, for antibody-based sensors the incubation times are typically shorter, as antibody-antigen interaction can be achieved within 15 – 30 minutes.

Table 3.2. Comparisons of detection ranges of caspase sensors

Detection method	Antigen detection range (concentrations tested)	Detection limit	Incubation time	Ref
Fluorometric and colorimetric biosensor - enzymatic	NA	50 μM caspase-3	Cell culture incubated with the caspase-3 specific substrate for 1 hour.	[208]
Electrochemical biosensor – cyclic voltammetry - enzymatic	0.1 nM – 2.5 nM caspase-3 (0.1 nM, 0.5 nM, 1 nM, 2.5 nM)	100 pM caspase-3	Caspase-3 was incubated with the functionalised HRP-MBDEVD-Au electrode for 1 hour.	[209]
Organic electrochemical sensor	0.1 pM – 100 pM caspase-3 (0.1, 1, 10, 100 pM)	0.1 pM caspase-3	Sample incubated with substrate for 10 hours.	
Surface enhanced Raman spectrum-based biosensor - enzymatic	50 pM – 1 μM caspase-3 (50 pM, 100 pM, 200 pM, 1 nM, 10 nM, 100 nM, and 1 μM)	50 pM caspase-3	Cell electrodes were immersed into the caspase-3 probes for 2 hours.	[210]
M13 phage virus-based electrochemical sensor - enzymatic	0–1.2 μM caspase-3 (0.001, 0.025, 0.05, 0.1, 0.2, 0.4, 1.2 μM in PBS buffer)	0.39 μM caspase-3	One-hour incubation.	[119]
Electrochemical sensor - enzymatic	0 – 250 pg/mL caspase-3 (6, 12.5, 25, 50, 100, 250 pg/mL) (0.19, 0.375, 0.75, 1.5, 3, 7.5 pM)	0.2 pg/mL caspase-3 (0.005 pM)	Substrate was incubated with a given concentration of caspase-3 for 2 hours. Then, the streptavidin-covered electrode was incubated with the sample for 30 minutes.	[211]
Electrochemical immunosensor-differential pulse voltammetry and EIS	0.1–100 μM caspase-9 (0.1, 1, 2.5, 20, 40, 60, 80, 100 μM)	0.08 μM caspase-9	Electrode incubated in the cell lysis buffer for 30 mins.	[160]
Fluorescence resonance energy transfer (FRET) biosensor - enzymatic	0.001 – 1000 nM caspase-8 (0.001, 0.02, 0.1, 0.5 , 1, 10, 100, 1000 nM)	0.7 nM caspase-8	Incubated 22.5 nM of sensor C8A protein with different amounts of caspase-8 for 1 h and measured its FRET effect.	[212]
Electrical impedance spectroscopy – Antibody-based	1 – 16 nM caspase-9	0.33 nM	Incubation with caspase-9 in buffer for 15 minutes	This thesis

3.4 Summary

This chapter presents a simple and low-cost method for the fabrication of zinc oxide/copper oxide composite surfaces using a sonication based-technique. The facile fabrication of nano-surfaces is enabled by the use of commercial ZnO and CuO nanoparticles of defined shape and size thus removing the need to synthesis the nanoparticles from precursors via high temperature or chemical processes. The SEM analysis revealed differences in the surface morphology when three different concentrations of ZnO suspension were applied. The ZnO-only film has a smoother surface with incomplete coverage of the glass substrate. The ZnO/CuO composite film demonstrated complete coverage of the substrate and highest surface roughness. The higher surface roughness contributes to an additional surface area for biological binding when compared to a smooth surface. The combination of 1% ZnO and 1% CuO resulted in the highest image surface area and slightly lower surface roughness compared the 2% ZnO/1% CuO composite surface. This difference was not enough to justify the additional costs associated with sensor fabrication using 2% ZnO/1% CuO composite surface. After the addition of the antibody to the ZnO/CuO nano-surface, an ELISA confirmed the presence of antibody on the surface. The high isoelectric points of ZnO (IEP~9.5) and CuO (IEP~10) enables stable immobilisation of biomolecules with lower IEP through electrostatic interaction.

After the morphological and biochemical characterisation of the sensor surface, the specific caspase-9 binding interaction was measured using non-faradaic electrical impedance spectroscopy. Correlation of determination analysis was used to determine the frequency at which a stable and reproducible trend in the impedance signal could be observed with increasing caspase-9 concentration. At a fixed frequency of 1010 Hz, a dose dependent

response was observed from 0.1 U/mL and 2 U/mL of caspase-9 using the ZnO/CuO composite surface. The calibration curve using the composite surface displayed higher sensitivity with a three-fold enhancement in signal compared to the ZnO-only surface. This improved performance could be explained by the synergistic effect of CuO nanoflakes and ZnO nanorods which offered high surface area for antibody immobilisation and a pitted surface reducing the charge screening effects associated with the electrical double layer. Additionally, the p-type CuO forms a heterocontact interface with the n-type ZnO resulting in increased sensitivity to charge accumulation. The optimal antigen incubation time was determined to be 15 minutes as **Figure 3.8** shows that incubation time beyond 15 minutes does not greatly influence the impedance output. The performance of the biosensors is related to the availability of antibody on the surface to bind caspase-9 when added to the surface. The optimal antibody loading concentration was determined to be 200 ng, as biosensors loaded with 200 ng antibody generated larger output signals compared with sensor fabricated with 100 ng. The 1% ZnO/1% CuO sensor demonstrated a linear range from 1 – 16 nM, with a limit of detection of 0.33 nM, which is superior to the caspase-9 sensor and comparable with many of the other caspase sensors cited in the literature. Finally, the simple and inexpensive method for the fabrication of ZnO/CuO composite surfaces was effectively demonstrated and caspase-9 binding interaction can be characterised with electrical impedance spectroscopy.

The next chapter builds on this work by evaluating the performance of the caspase-9 sensor in a cell culture environment to monitor release of caspase-9 from apoptotic cells in real-time. The performance of the sensor was compared with conventional biochemical and microscopic techniques.

Chapter 4

Impedimetric biosensing of caspase-9 in mammalian cell culture

In the previous chapter, the 1% zinc oxide (ZnO) /1% copper oxide (CuO) composite nano-surface demonstrated excellent performance for the detection of caspase-9 in buffer solution. Enhanced sensitivity is achieved by leveraging the physiochemical properties of ZnO and CuO at the electrode-solution interface. This chapter builds on the results from the previous chapters, to demonstrate the applicability of using this biosensor for caspase-9 detection in CHO culture media. It describes the following elements of experimentation. Biochemical characterisation of the biosensor surface was performed using an enzyme-linked immunosorbent assay. The characteristic biomolecular interactions between the target analyte and specific capture probe of the biosensor are quantified using non-faradaic electrical impedance spectroscopy. Anti-cleaved caspase-9 antibody was used to functionalise the biosensor surface to detect the active caspase-9 rather than other types of caspase-9. Using a luminescence-based assay, the presence of active caspase-9 was detected in the culture media following exposure to a pro-apoptotic agent.

The work presented in this chapter has been mostly published in Chen *et al* [213]. I contributed to the research design and carried out the experimentation including nano-surfaces preparation and fabrication, surface characterisation, immunology assay and impedance test. I also processed the experimental data, discussed the results, and wrote the initial draft of the manuscript.

4.1 Introduction

The significance of monitoring apoptosis in mammalian cell culture in a bioreactor environment was highlighted in Chapter 1. To summarise, lower yields and poorer quality of biopharmaceutical products result from cell death in bioreactors [5]. Such cell death is commonly associated with programmed cell death or apoptosis. The established methods for apoptosis detection include observation of cell morphology and probing of DNA fragmentation [64,68]. These methods focus on the detection of changes that occur late in apoptosis. Nevertheless, detection of apoptosis at the early stages, prior to gross morphological changes, is critical for understanding the entire apoptotic pathway and for offering the possibility to intervene and enhance longevity and productivity of cell cultures used for the production of biologicals. A group of proteases known as caspases act together in a cascade to cleave proteins at aspartic acid residues [7]. This proteolytic cascade amplifies the apoptotic signalling pathway and thus leads to rapid cell death [7]. Hence, the detection of apoptosis at its earliest stages will enable faster responses or pharmaceutical interventions to rescue the culture and enhance culture longevity and productivity.

In the previous experimental chapter, it has been demonstrated that non-faradaic biosensing technology can be created using a ZnO/CuO composite nano-surface on an insulating layer of glass above D-shaped (1 mm gap) electrodes. The biosensor demonstrated linear detection range with low limits of detection for caspase-9 in buffer. In the previous chapter, the methodology describes a two-terminal impedance spectroscopy setup, whilst in this chapter, a four-terminal method was selected over the two terminal method. Each configuration has its own advantages and applications. The main advantage of the four point setup is the elimination of contact resistance. In 4-point measurements, separate pairs of electrodes are

used for current injection and voltage measurement. This configuration effectively eliminates the influence of contact resistance and lead resistance from the measurement, providing more accurate and reliable impedance data.

In the section of work described in this chapter, the biosensor was used to detect caspase-9 from cell lysate extracted from apoptotic cells. The impedimetric biosensor's performance were compared with an enzymatic capase-9 assay and with a morphology-based method under similar experimental conditions, to evaluate the effectiveness of the biosensor as an early detection assay for apoptosis. Microscopic techniques were used to visualize the changes in the cell morphology that occur during apoptosis. The enzymatic capase-9 assay is based on a colorimetric method, which requires the cleavage of a specific substrate that generates a coloured product. The coloured product is detectable by spectrophotometry and the signal is correlated to the concentration of the enzyme in the sample. Together these complementary methods allow us to follow the progression of apoptosis in cells and give us a handle to allow intervention at early stages of apoptosis.

4.1.1 Morphological detection of apoptosis

Prior to the emergence of biochemical assays and biosensors, the presence of apoptosis was commonly established with morphology based-techniques, such as electron microscopy, light microscopy and flow cytometric detection [28,31,32]. Methods such as light microscopy and electron microscopy can provide excellent spatial/morphological information and are used to identify mid-late stage apoptotic cells [28]. Transmission electron microscopy (TEM) is a technique commonly used to detect characteristic changes in the ultrastructural features of apoptosis, such as cytoplasmic condensation, nuclear fragmentation and appearance of

cytoplasmic organelles [34,214]. However, this technique is no longer routinely used as an apoptotic assay due to the cost associated with performing electron microscopy, i.e. the specialized equipment and the time consuming, specialist technical expertise required [34].

In more recent years, evaluation of cells and tissues for apoptosis has evolved towards staining for light microscopic and flow cytometric analysis [34]. Morphological changes, such as cell shrinkage, membrane blebbing, formation of apoptotic bodies can be identified rapidly and accurately by examining stained cells using light microscopy. The Romanowski group of stains are general purpose stains routinely used for the examination of cells [215]. The Romanowski stains are a combination of methylene blue and eosin. The methylene blue is used to stain the nucleus (blue) whilst the eosin stains the cytoplasm and cytoplasmic components [215]. The advantages of this type of microscopy include rapid analysis times, capability of performing tests on living cells, lower cost equipment and a reduced technical complexity [216].

One of the weakness of visual characterization of cell-death related parameters was the difficulty in obtaining quantitative data. Fortunately, this has begun to change in the last decade with the advancement of high-throughput workstations that allow for automated image acquisition from 96-well plates and software-assisted image analysis [216]. Helmy *et al* [217] developed an automated quantitative approach for the assessment of apoptotic progression in Hep2 cell lines. The nuclear area, perimeter and circularity of the nuclei were automatically measured and inputted into a formula to calculate the nuclear area factor (NAF) [217,218]. Lower NAF values were measured for staurosporine-incubated cells compared with the control cells due to their smaller nuclear area and circumference [218].

The decrease in cell nuclei was due to DNA loss and the increase in form factor upon the initiation of apoptosis.

Digital pathology has developed rapidly in recent years. In cell biology applications, machine learning and image recognition methods can increase processing capabilities and objectivity [219]. Machine learning methods facilitate the high-throughput analysis of cell image sets versus tedious and subjective manual processes. However, there are several challenges with objective image quantification that need to be addressed, including image artefacts, batch-to-batch variations such as microscope settings, controlling the extent of cells across different conditions and optimal concentrations and time points [218]. Jin *et al* [219] developed an automated cell death classification method for fibrosarcoma cells using a logistic regression model and achieved a prediction accuracy of 93% within the three classes (control, ferroptosis and apoptosis).

The main advantages of observing general morphological features of apoptosis include the simplicity, convenience, and intuition in the observation. In the present study, a light microscopy method with staining of intracellular components was used to characterise the morphological progression of apoptosis in adherent CHO cells. The nuclear area and NAF were calculated with the assistance of image analysis software ImageJ. The results of the morphological analysis were compared with biochemical and biosensing approaches at specific time points to provide an integrated multimodal approach to the measurement of apoptosis.

4.1.2 Biochemical detection of apoptosis

Biochemical detection, which refers to the detection of biomarkers related to the molecular mechanism of apoptosis have been increasingly employed in the past decade. Molecular biology methods can be used to clarify the mechanism of apoptosis. Fluorescent enzyme immunoassays allow for the detection of apoptosis specific biomarkers related to the apoptotic-related signalling pathways [214]. Under normal circumstances, the intracellular aspartate-specific cysteine proteases (e.g. caspases) and endonucleases exist in the cell nuclei in their inactive form [214]. Caspases are categorized as initiator or effector caspases, based on their position in apoptotic signalling cascades [214]. The activation of caspase-9 is a crucial step in the context of the intrinsic apoptosis as activated caspase-9 cleaves and activates downstream effector caspases, such as caspase-3 [220]. Therefore, the occurrence of apoptosis can be detected by the changes in the concentration of apoptosis-related proteins using specific immunolabelling techniques. Immunolabelling refers to the labelling of antibody or antigen with fluorescein, enzymes or radioisotopes to greatly enhance the sensitivity of the antibody-antigen reaction [214].

One of the most widely used antibody-based methods is the enzyme-linked immunosorbent assay (ELISA) which involves the binding of the target antigen to the capture antibody and a secondary antibody that is conjugated to an enzyme, such as horse radish peroxidase or alkaline phosphatase [221]. The enzyme converts the chromogenic substrate into a coloured product which can be measured using plate reader. Previous literature has reported the use of ELISA for the detection of caspase-1 [222], caspase-6 [223] and caspase-3 [224,225]. This method is suitable for the detection of apoptosis at different stages and can be used to determine the degree of apoptosis by analysing the ratio of cleaved-caspase to pro-caspase [224].

The caspases' enzymatic activity can be leveraged in protease assays to provide sensitive, fast, and high-throughput screening of apoptosis. Traditionally, protease assays use peptide-conjugated fluorophores to generate the fluorescence signal that can be correlated with the concentration of the protease [222]. However, the sensitivity can be limited for several reasons. Residual fluorescence of some peptide-conjugated fluorophores may overlap with their fluorescent products, which can increase background noise and reduce sensitivity [222,226]. Cells also can exhibit autofluorescence, causing increased background noise in cell-based assays. Assays that use luminescent substrates could potentially remove the concerns surrounding autofluorescence and background noise associated with fluorescence [227]. Homogeneous, chemiluminescent protease assays have been previously reported using peptide-conjugated aminoluciferin substrates [222,227]. These studies demonstrated that the luciferase does not produce light until the peptide is cleaved from the aminoluciferin [227]. Upon activation of intracellular caspases and subsequent cleavage of the peptide substrate, the luminescent product is released. This reaction is proportional to caspase activity and thus to the induction of apoptosis [42].

In the present study, an ELISA assay was used to validate the binding of the antibody on the nano-surface of the biosensor. A sandwiched ELISA assay was deployed to evaluate the caspase-9 binding ability of the biosensor recognition layer. The measured absorbance values were correlated with caspase-9 binding on the ZnO/CuO nano surface. Caspase-9 activity was then analysed using a LEHD-based chemiluminescent cell-based assay. LEHD is an amino acid sequence (Leu-Glu-His-Asp) cleaved by caspase-9. The cleavage of this sequence leads to the generation of a "glow type" luminescent signal. This signal is proportional to the

amount of caspase-9 activity present. To overcome background noise and autofluorescence concerns associated with the use of fluorescence-based methods cell cultures, this assay uses a thermostable luciferase which generates a stable signal across a wide variety of assay conditions. Alongside microscopy, protein based assays, measured using different analytical techniques, these combined, complementary methods can offer increased information content with the potential to detect key regulatory proteins involved in apoptosis soon after the induction event [30].

4.2 Methods and materials

The following materials were used in the preparation of the biosensors:

- Zinc oxide nanoparticles (99.9 +%, 80-200 nm) and CuO nanoparticles (99.5 +%, width: 10-30 nm, length: 200-800 nm) from US Research Nanomaterials Inc. Houston, TX, USA).
- polyclonal Rabbit anti-cleaved caspase-9 IgG used for the impedance analysis (ab52298, Abcam Ltd. UK), non-fat milk powder (Tesco).
- monoclonal mouse anti-caspase-9 IgG used for the sandwich ELISA assays (sc-56073, Santa Cruz Biotechnology, Inc., USA), caspase-9 (CC120, Sigma-Aldrich).
- Goat anti-mouse IgG:HRP (Bio-Rad Laboratories Ltd, UK), tetramethylbenzidine (TMB) solution (Alfa Aesar), TMB stop solution (Merck)
- CHO-K1 cell line (ATCC- CCL-61) and F12K media were purchased from ATCC. Fetal bovine serum was purchased from Merck

Phosphate buffered saline (PBS, pH 7.3 ± 0.2 at 25 oC) was purchased from Merck. The PBS buffer was diluted to 0.01 M adjusting the pH to 7.4.

4.2.1 Surface preparation

The sum of 0.3 g ZnO nanoparticles and 0.3 g of CuO nanoparticles was added to 30 mL double de-ionised water. The 1% ZnO/1% CuO suspension was stirred at room temperature for 1 hour and then ultra-sonicated in pulsing mode (20s off/20s on) for 5 minutes using a 13 mm probe (Sonics & Materials. Inc.) at 100 watts. Glass substrates were initially cleaned via sonication in ethanol for 10 minutes. 250 µL drops of the suspension were cast onto clean glass coverslips (width: 22 mm, length: 22 mm, thickness: 0.13-0.17 mm, Cole-Palmer, UK) to form ZnO/CuO nano-surfaces. Finally, they were dried in an oven at 50oC for 4 hours, then stored in a dry atmosphere with silica gel for up to 2 days.

4.2.2 Caspase 9 sensor fabrication

Rabbit anti-cleaved Caspase-9 IgG (ab52298) was stored and diluted in 0.01 M PBS. The sensing area (10 mm x 4 mm) of each ZnO-CuO nano-surface on glass was defined by tape. Subsequently, 40 µL (1 µg/mL) of antibody solution was dropped on to the sensing area and incubated for 3 hours at room temperature. Surfaces were washed three times with PBS buffer before the addition of 40 µL of 5% non-fat milk to block the surface and inhibit nonspecific interactions. The surfaces were left at room temperature for 1 hour and then washed again to remove unbound proteins. The biosensor was then dried in a vacuum desiccator with silica gel at 4^{o}C overnight for 18 hours. The nano-surface biosensors were positioned above a pair of co-planar rectangular-shaped electrodes formed from 35 µm copper on FR4 substrate (printed circuit board PCB). The overall diameter of the co-planar electrode is 22 mm, each electrode has a width of 10 mm and separation distance between the electrodes is 1.0 mm (**Fig. 4.1a**).The sensor was aligned in a way that the rectangular sensing

area (10 mm x 4 mm) is positioned directly above the gap (**Fig. 4.1b**). A cross section of the biosensor is illustrated in **Fig. 4.1c**.

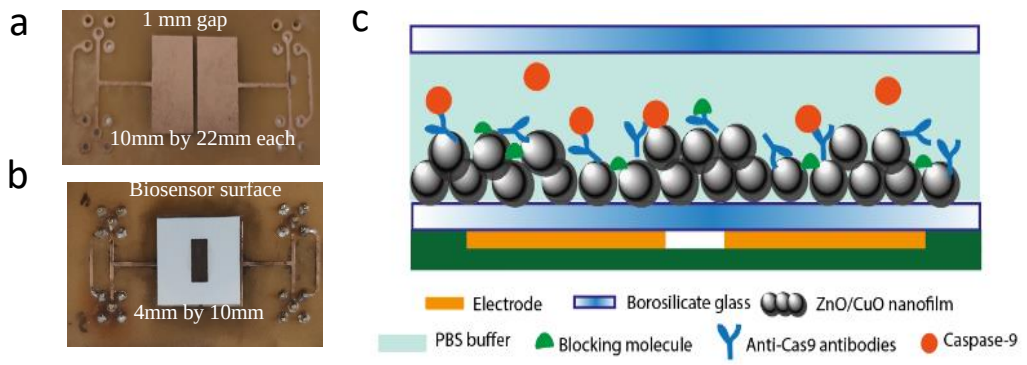

Figure 4.1. Electrode setup and schematic of the biosensor (a) pair of square-shaped copper electrodes 22.1 mm diameter with a 1 mm gap in the middle. (b) Sensor setup showing this sensing area (10 mm x 4 mm) defined by white tape. (c) Cross-sectional illustration of the biosensing surface and the biorecognition interactions between anti-cas9 and caspase-9.

4.2.3 Surface uptake of antibody

Antibody uptake on ZnO-CuO nano-surfaces was quantified using an enzyme based immuno-assay. Using the ZnO-CuO nano-surfaces prepared as described previously in Section 4.2.1, 50 µL (1 µg/mL) drops of mouse anti-cas9 IgG (sc-56073) were cast onto the defined sensing area. The surfaces were then incubated for 3 hours and then washed to remove unbound antibodies. The surfaces were incubated with 5% non-fat milk for 1 hour and washed again. The sensor was allowed to dry in a desiccator overnight. Following a thorough wash to remove any unbound antibody, 100 µL (1 µg/mL) of Goat anti-mouse IgG:HRP (Bio-Rad Laboratories Ltd, UK) was added to the surface and left for 1 hour at 25^{o}C. Then, the surfaces were washed three times with PBS buffer to remove any unbound antibody. 200 µL of TMB solution was added as the enzyme substrate to generate a coloured product. Finally, 100 µL of

the TMB solution were extracted from the sensor surface and mixed with 100 µL of TMB stop solution inside 96 well plates. The intensity of the coloured product was read at 450 nm using a microplate reader (SpectraMax ID5, Molecular Devices).

4.2.4 Validation of antibody-protein interaction at the sensor surface

In order to validate the binding of caspase to the sensor surface, an assay based on sandwich ELISA was performed. The functionalised ZnO-CuO nano-surfaces were prepared as previously described in Section 4.2.2. Following a thorough wash step to remove unbound antibody and milk proteins, capase-9 spiked PBS solutions were added onto the surface and incubated for 30 minutes. Five concentrations of caspase-9 (0.1 U/mL, 0.25 U/mL, 0.5 U/mL, 1 U/mL and 2 U/mL) were studied. According to the manufacturer's technical specification state one unit of activity contains approximately 0.135 – 0.4 µg (0.27 µg on average) of caspase-9. The molecular weight of caspase-9 is 35 kDa. Therefore, the concentrations tested in this study were: 0, 1 nM, 2 nM, 4 nM, 8 nM and 16 nM. For control purposes, 50 µL of fresh PBS buffer without caspase-9 was added to the sensor surface. Following incubation with the caspase-9 solutions, 50 µL (1 µg/mL) of mouse anti-cas9 IgG (sc-56073) was added to the sensor surface for 1 hour to probe for any bound caspase-9. To probe for the mouse anti-body, 100 µL (1 µg/mL) of goat anti-mouse IgG:HRP were added to the surface and left for 1 hour. Finally, colour formation was generated from the TMB:HRP reaction was measured at 450 nm using a microplate reader.

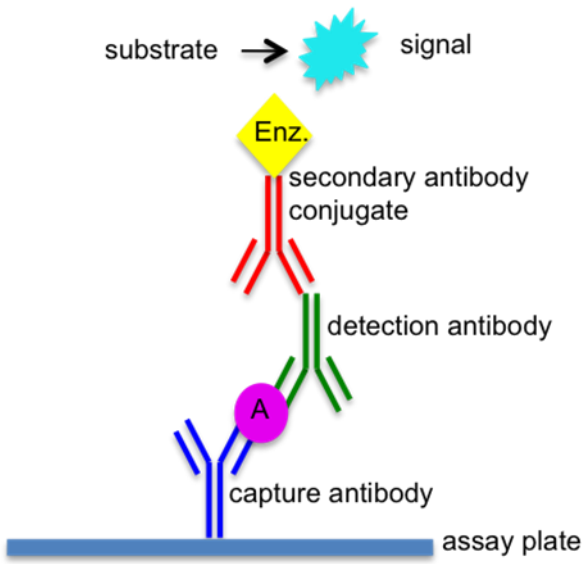

Figure 4.2. Schematic illustration of the sandwich ELISA assay. 1) Coating the sensor surface with capture antibody. 2) Add the antigen. 3) Add the detection antibody (mouse anti-cas9). 4) Add the secondary antibody conjugated to enzyme (rabbit anti-mouse). 5) Add the substrate which is then converted to a measurable luminescent signal.

4.2.5 Impedance measurements of caspase-9 in buffer

A HF2IS impedance Spectroscope with the HF2TA 50 MHz Current Amplifier (Zurich Instruments, Switzerland) was used to measure the impedance of the nano-crystal surfaces. The electrodes are insulated by the glass. Consequently, no DC current can flow between the electrodes and therefore redox reactions are prevented. Four terminal impedance measurement mode was used to reduce the sensitivity of the measurement to the resistivity of the connecting leads. In this mode, the HF2IS instrument generates a sine wave voltage excitation signal and the measured current and voltage drop across the sensor was used to calculate the impedance. The output voltage, Vz, was measured directly by the second

differential of Input 1+ and input 1- of the HF2IS. The experimental setup is shown in **Fig. 4.1**. Impedance was measured from 15 MHz to 100 Hz at a voltage of 2 Vpp with 200 test points. This electrode voltage is applied to generate a sufficient electrostatic field beyond the glass layer to penetrate into the ZnO and ZnO/CuO substrates. The impedance plots were analysed using the ZiControl Frequency Response Analyzer tool.

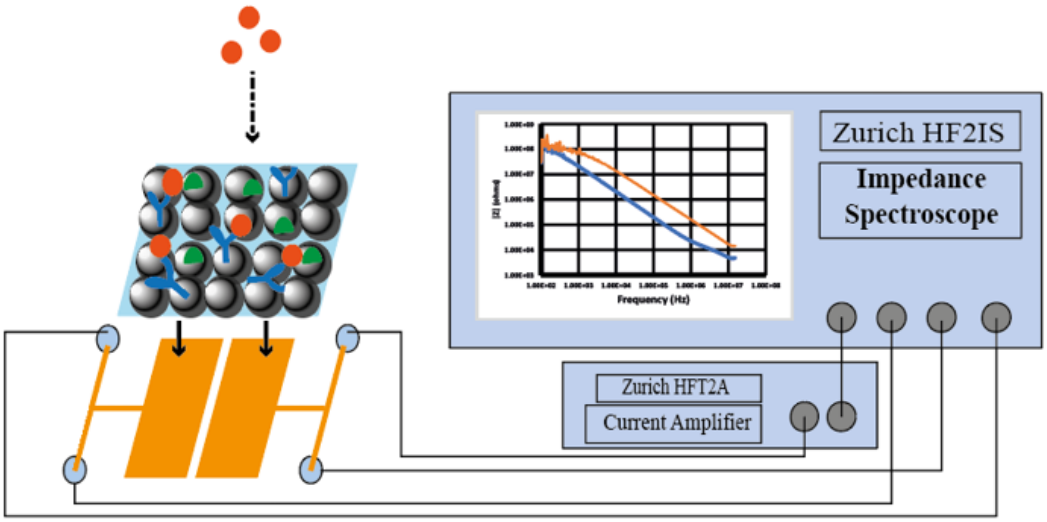

Figure 4.3. Experimental setup with sensor connected in four terminal mode to the HF2IS Impedance analyser for the impedance analysis in the frequency of 100 Hz – 15 MHz.

The impedance amplitude and phase were measured after a 5 min incubation time for 15 min following the addition of increasing concentrations (0, 0.1, 0.25, 0.5, 1 and 2 U/mL) of human recombinant active caspase-9 (CC120). The sensing surface was washed with 0.01 M PBS and dried with paper towel before addition of each new sample. Damage to the sensor surface was minimised by carefully applying the paper towel to the edges of the sensing

region and absorbing the liquid through capillary action. Sensor response was plotted using readings taken at a frequency of 6 MHz. Impedance amplitude, phase change and capacitance were evaluated as function of antigen (caspase-9) concentration in the buffer. The phase change was defined as the difference between the phase value of the biosensor after 10 min incubation with caspase-9 and the phase value of the control (surfaces without anti-caspase-9 functionalisation). Results were plotted using a logarithmic scale on the x axis.

To demonstrate specificity of the anti-cas9 antibody, control experiments consisting of 2 U/mL of caspase-3 (C1224, Sigma-Aldrich) and caspase-8 (C1099, Sigma-Aldrich) were added to the sensor surface functionalised with anti-cas9 antibody (ab52298).

4.2.6 Induction of apoptosis

CHO-K1 cell lines were grown in F12K media supplemented with 10% foetal bovine serum. They were maintained in T-75 flasks, incubated at 37ºC in a humified 5% CO^2 atmosphere until 90% confluency. CHO-K1 cells were counted, and cell viability was calculated by Trypan blue dye exclusion using an automated cell counter (Luna II™; Logos Biosystems, Inc., Annandale, VA, USA). Cells were then seeded into 6 well plates and incubated at 37ºC for 24 hours.

Staurosporine (19-123M, Merck, UK) was diluted to produce a 1 mM stock solution. Following the 24 hours incubation, cells were treated with 1 µM staurosporine and then incubated at 37ºC for 24 hours. Cell images were captured using the Olympus SC50 industrial microscope camera fitted with a 20x objective lens (LCPLFLN20xLCD).

To extract the cell lysate, supernatant was removed from the cells, cells were then washed with PBS. The cells were then scraped from the flask. The sample was centrifuged at 1665

rpm for 5 minutes at 4 °C (Eppendorf Centrifuge 5804, A-4-44 swinging bucket rotor). The supernatant was then removed and discarded. The cell pellet was resuspended in 100 µL NP-40 Cell Lysis Buffer (Thermofisher) and incubated on ice for 10 minutes. Afterwards, samples were sonicated as follows: amplitude 50%, 5 sec ON, 10 sec OFF, for a total sonication time of 1 minute. Tubes were centrifuged at 8000 rpm for 15 minutes at 4°C and supernatants were moved to quantification via EIS.

4.2.7 Impedimetric measurements of caspase-9 in cell culture

ZnO-CuO biosensors were prepared as described in Section 4.2.2, using rabbit anti-cleaved antibodies as the bioreceptor. Impedance amplitude, phase angle and capacitance measurements were performed on cell culture samples at 0, 1, 3, 4, 6 and 24 hours following exposure to staurosporine. New sensors were used for the testing of subsequent samples. For control purposes, fresh F-12K medium without cells were also studied. A Kruskal-Wallis test was used to analyse the data and level of significance was defined as $p \leqslant 0.05$.

4.2.8 Luminescence caspase activity assay

CHO-K1 cells were cultured in the same conditions as described in Section 4.2.6. In order to compare with the EIS data, chemiluminescent assays were carried out using a well-described Caspase-Glo® 9 Assay Systems from Promega (United Kingdom) following the manufacturer's recommended protocol. The assay provides a luminogenic caspase-9 substrate in a buff er system optimized for caspase activity, luciferase activity and cell lysis. The addition of Caspase-Glo® 9 reagent results in cell lysis, followed by caspase cleavage of the substrate. Briefly, the chemiluminescent assay was based on the luminescence of a p-

nitroaniline (pNA) moiety that was released upon proteolytic activity of caspase-9 on a pNA-conjugate peptide substrate. The generated luminescence signal is correlated to the activity of caspase-9 present in the sample. Readings were taken at 0, 1, 3, 6 and 24 hours following exposure to staurosporine. Six cell concentrations (5000, 10000, 20000, 40000, 80000 and 160000 cells/50 µL) and five concentrations (1, 2, 4, 8 and 16 µM) of staurosporine were also studied. For control purposes, fresh F12-K medium with the peptide substrate only (without cells or toxins) were added to the control wells, and luminescence readings were measured using a microplate reader (SpectraMax ID5, Molecular Devices).

To determine the relationship between luminescence and caspase-9 activity. Caspase-9 activity was measured across different concentrations (0.1, 0.25, 0.5, 1, 2, 3, 4 U/mL) of caspase-9 (CC120). Caspase-9 was diluted in F12K media and incubated with an equal volume (50 µL) of Caspase-Glo® 9 reagent for 30 min at 37^{o}C. Luminescence readings were measured using a microplate reader.

4.2.9 Nuclei morphology imaging

CHO-K1 cells were cultured in F-12K culture medium as described in Section 4.2.6 and 100,000 cells were seeded onto 13 mm glass coverslips and left in 1 ml of medium to settle overnight. Coverslips were exposed to 500 µL of 1 µM of staurosporine in medium and incubated for 0, 1, 3, 6 and 8 hours. Upon reaching the specific time point, the respective coverslips were fixed in 500 µL of 4% PFA in PBS (0.1M, pH7.2) for 20 minutes. Before mounting, coverslips were stained with Hoechst solution (1: 10,000 dilution in PBS, Thermo Fisher Scientific) for 10 minutes, protected from light. The cells were imaged on a Leica SP5

confocal laser scanning microscope using a 63x, 1.4 NA objective. Single stack images were taken.

Image analysis was conducted using the FiJi/ImageJ software, version 1.53c (NIH, FiJi, USA). A macro was devised (language: IJ1 Macro) to segment objects of interest (i.e. nuclei) within the images and measure their area and circularity [4π(area/perimeter^2)], and calculate the Nuclear area factor (NAF). The macro performed Huang thresholding (global threshold) on the images (8 bit), with the "fill holes" and "watershed" functions applied and calibrated to measure objects between 10 and 560 µm^2. Measurements entailed: mean nuclear area (µm^2) and mean NAF. Data was collected from between 1900 and 3600 (nuclei) from each time interval, consisting of both intact and fragmented nuclei. Mean values, % changes with associated standard error bars and relevant statistical tests were calculated using Microsoft Excel 2016 and graphically depicted. The Pearson Correlation (2-tailed) test was performed on nuclei area and NAF data, at the level of significance $p \leqslant 0.05$.

4.3. Results and discussions

4.3.1 Antibody functionalisation and validation

To validate the immobilisation of proteins on the ZnO-CuO nano-surfaces, an enzyme linked immunosorbent assay (ELISA) was performed (Section 4.2). Here, 1 μg/mL of anti-cas9 was added to the ZnO-CuO composite surfaces and a secondary antibody conjugated with horse radish peroxidase (HRP) was used to detect the specific protein binding on the nano-surfaces. The results shown in **Fig. 4.4a** indicate that the ZnO-CuO nano-surface was capable of capturing antibody even through physical adsorption. The surfaces with antibody recorded an optical density (OD) of 0.76 compared with only 0.16 for surfaces without primary antibody. The high isoelectric points (pI) of ZnO (IEP~9.5) [197] and CuO (IEP~10) [198] enables stable immobilisation of biomolecules with lower IEP through electrostatic interaction. In contrast, IgG antibodies typically have a pI between 6.5 and 8.5 and are negatively charged at physiological pH [199]. Therefore, biomolecules can be readily immobilised on a positively charged ZnO/CuO through strong electrostatic interactions.

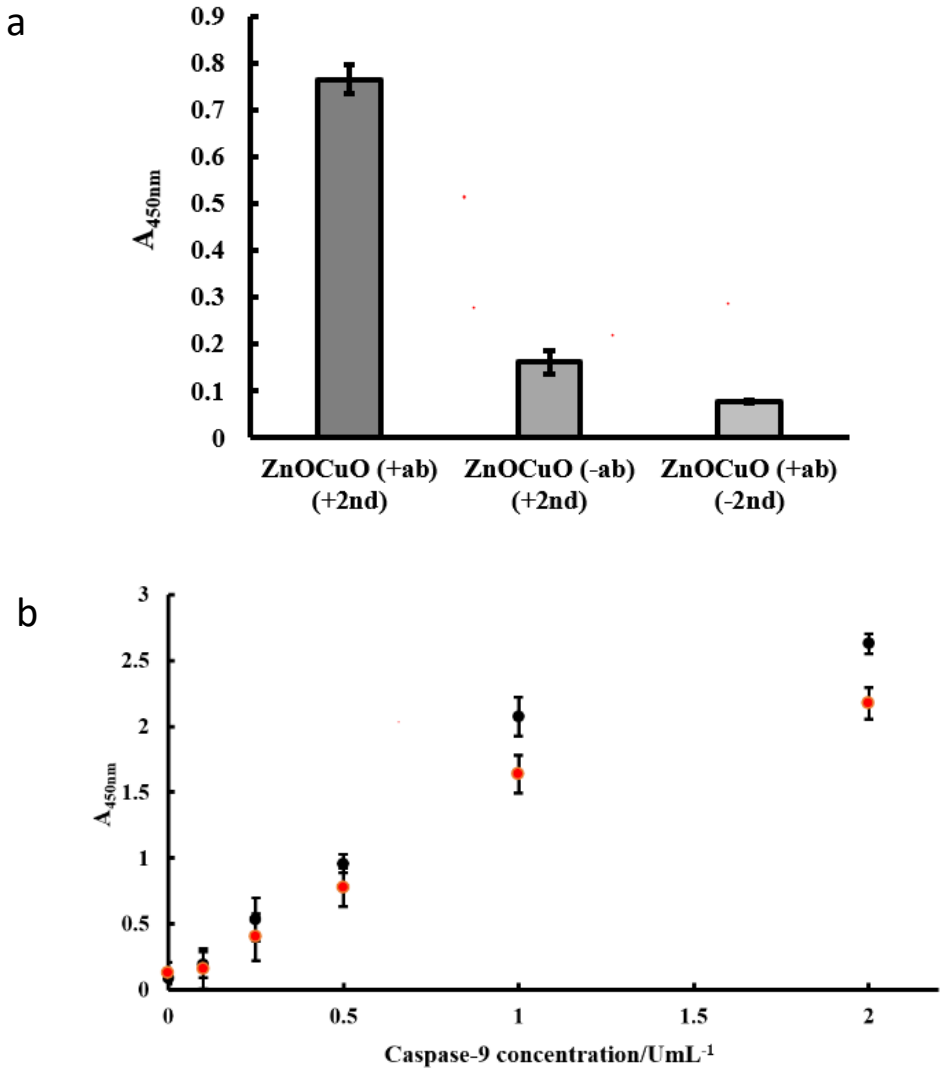

Figure 4.4. Validation of nano-surface chemistry (a) Bar chart of anti-cas9 immobilisation on nano-surfaces expressed by colour formation at 450 nm from HRP-TMB reaction. Third bar: without secondary antibody. (b) Sandwich ELISA assay for the detection of caspase-9 binding. Antibody concentrations tested are 1 ug/mL (●) and 0.5 ug/mL (●). Standard error bars are shown (n=5)

The sandwiched ELISA-based assay is used to validate the biomolecular binding of caspase-9 on the actual ZnO/CuO biosensor surface (Section 4.2.4). The measured absorbance values indicate caspase-9 binding can be detected on the sensor surface and the signal is linear between the concentration range of 0.1 to 1 U/mL (**Fig. 4.4b**). It can be seen that for the biosensors fabricated using 1 μg/mL generated larger output signals compared with the sensors fabricated with 0.5 μg/mL antibody, with greater differences at higher caspase-9 concentrations (**Fig. 4.4b**). This is to be expected as there are more binding sites available for antigen capture resulting increased caspase-9 binding at the sensor surface and thus increased signal output. Two control experiment were conducted: one without the capture antibody produced an optical density of 0.238 and one without the secondary antibody produce an optical density of 0.088 (**Fig 4.4a**). This indicates the change in colour intensity is due to the antibody-caspase-9 binding and not non-specific binding of the secondary antibody.

4.3.2. Detection of caspase 9 through impedimetric measurements

4.3.2.1 Impedance changes versus frequency

Following the characterisation of the functionalised sensor surface with and colorimetric assays, the specific binding interactions of caspase-9 were measured with electrical impedance spectroscopy. Impedance spectroscopy is a well-established approach for the analysis of complex biological liquids [200,201]. The sensor detects a variation of complex impedance, induced by dielectric constant change. In impedimetric sensors incorporating an insulating layer, such as the one described in this thesis, the sensor response is mostly gained from a capacitive component of the complex impedance [201]. Previous publications have demonstrated that a capacitive mode can be preferable for measurement of an antibody capture of an antigen [228]. In a typical non-faradaic impedance plot, the absence of redox reaction eliminates the parameters in the Randles model associated with electron transfer, i.e. charge transfer resistance (R_{ct}) and Warburg impedance (Z_w), as these tend to infinity. Therefore, in a non-faradaic EIS system, the impedance is inversely proportional to the electrical double layer capacitance.

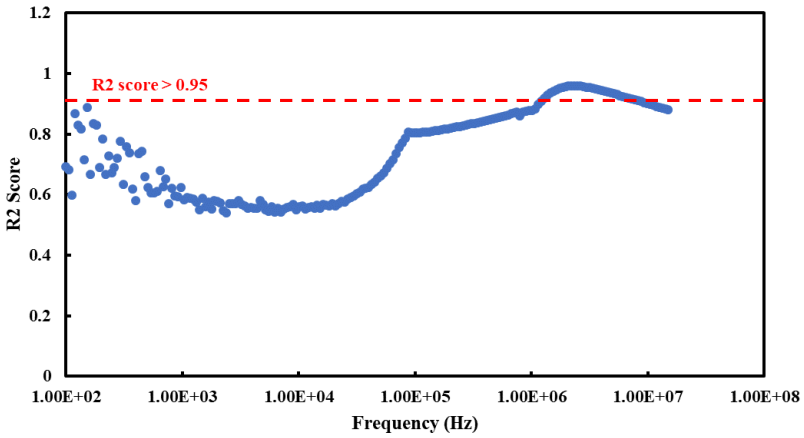

Figure 4.5. Correlation analysis of the y-variable (impedance magnitude) and x-variable (caspase-9 concentration) across the frequency range (100 Hz -15 MHz). Correlation of determination, R^2, tells you how strong of a linear relationship there is between two variables. A R^2 score > 0.9 indicates the regression line strongly fits the data.

For the characterisation of the biosensor performance, for each concentration of protein solution dropped onto the biosensor surface, the impedance magnitude (|Z|), phase and capacitance measurements were performed for each caspase-9 concentration (0.1, 0.25, 0.5, 1 and 2 U/mL). The analysis of protein solutions was made over the frequency range of 100 Hz to 15 MHz encompassing both α (1 Hz – 100 kHz) and β (100 kHz – 10 MHz) dielectric dispersion regions [201] for the caspase-9 solution (n = 5). The experimental setup is shown in **Fig. 4.3**. In the R^2, coefficient of determination plot (**Fig. 4.5**), areas of high correlation could be observed at low (<1000 Hz) and high (>1 MHz) frequencies, although the correlations tended to be more sporadic at lower frequencies (**Fig. 4.6)**. This is due to the fact that the impedance instrument is approaching its upper impedance boundary.

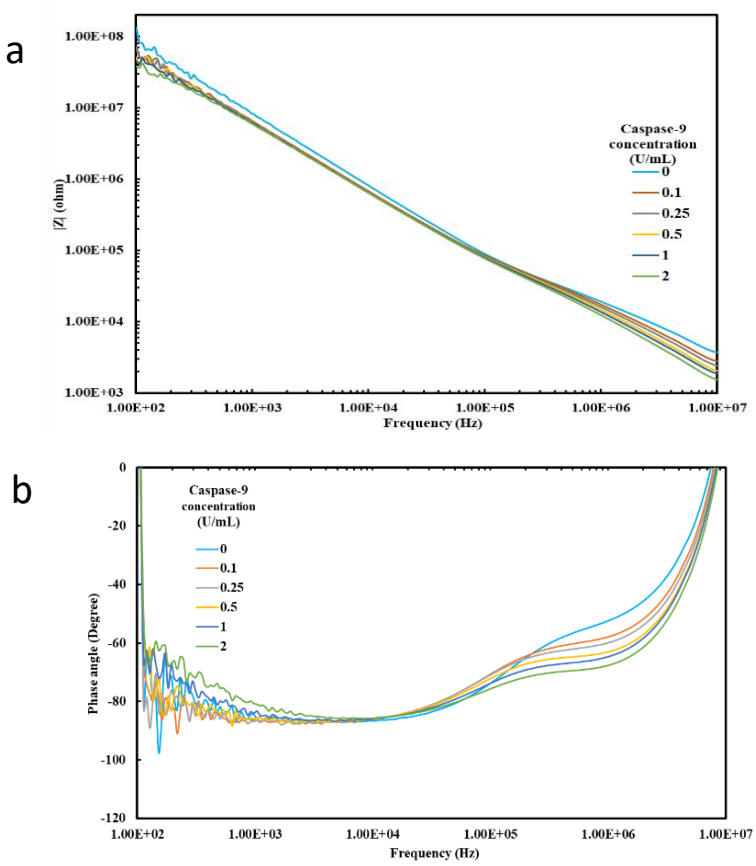

Figure 4.6. Frequency dependent phase and impedance responses (a) Impedance spectra (100 Hz – 10 MHz) of the biosensor coated with 1% ZnO/CuO functionalised with 1 µg/mL anti-cas-9. Responses to caspase-9 loading (0 – 2 U/mL) were recorded. (b) Equivalent phase plot (100 Hz – 10 MHz).

As shown in **Fig 4.7a** and **Fig 4.7b**, the mid-high frequency regions (100 kHz – 10 MHz) appear to contain the most significant changes in both impedance magnitude and phase shift. This finding concurred with previous literature. For example, Oseev et al. [201] demonstrated the distinguishing sensor response on various protein concentrations in the frequency ranges of β (100 kHz – 10 MHz) and δ (10 MHz – 1 GHz) dispersion regions. In this PhD study, a frequency of 6 MHz was selected for the calibration plots, because at this frequency, a

significant statistical difference (2σ) between the buffer measurement (0 U/mL) and the first sample (0.1 U/mL) was calculated.

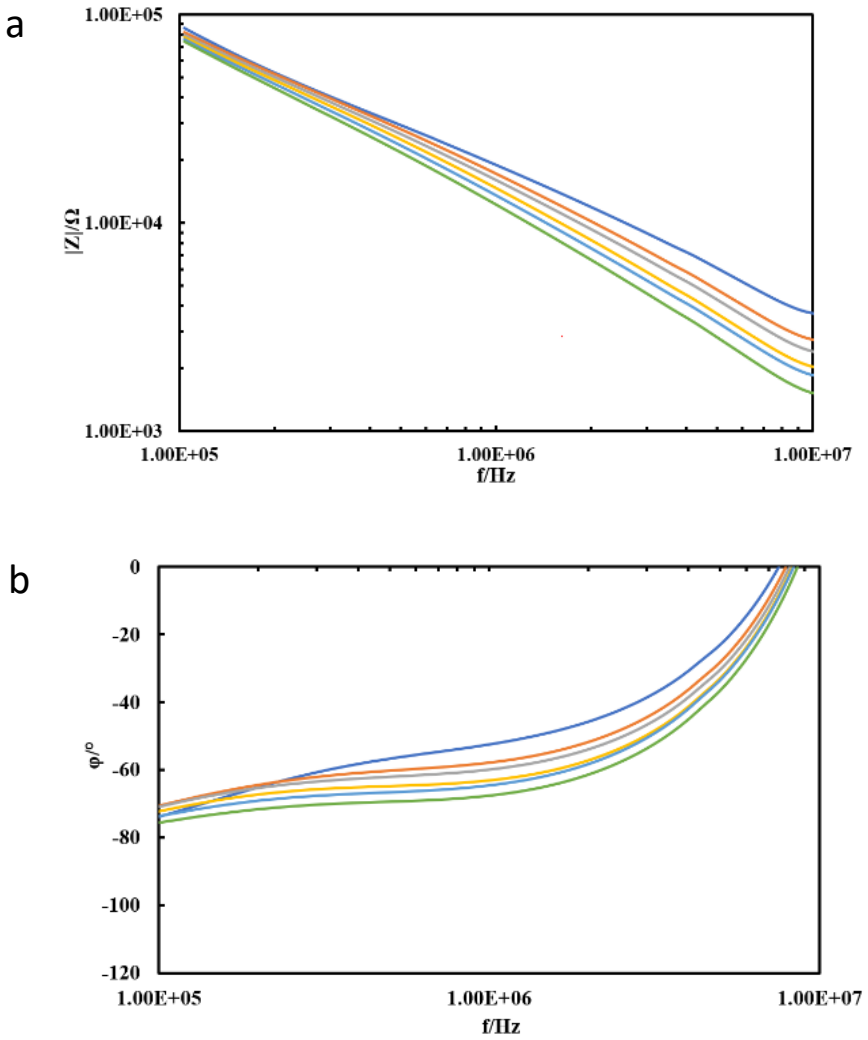

Figure 4.7. Frequency dependent phase and impedance responses (a) Impedance magnitude spectra (100 kHz – 10 MHz) of the biosensor coated with 1% ZnO/CuO functionalised with 1 µg/mL anti-cas-9. Responses to caspase-9 loading at various concentrations: 0 (■), 0.1 (■), 0.25 (■), 0.5 (■), 1 (■) and 2 (■) U/mL, were recorded. (b) Equivalent phase plot (100 Hz – 10 MHz).

4.3.2.2 Impedance magnitude and phase angle with caspase loading

Fig. 4.8a shows the generated calibration curves containing the corresponding impedance and phase values with different concentrations (0, 0.1, 0.25, 0.5, 1, 2 U/mL) of caspase-9 after 10 minutes incubation on the sensor surface, measured at a frequency of 6 MHz (the mean of 5 replicates). Both impedance magnitude and phase angle decrease with caspase-9 concentration. There are several explanations of this phenomenon. Semiconductor materials, such as ZnO and CuO, will readily form an electrical double layer when they interact with the liquid electrolyte, resulting in charge accumulation at the interface region [89]. Furthermore, the binding interaction between the capture antibody and target biomolecule at the electrode surface results in a capacitive increase [200]. When caspase-9 antigen binds to the ZnO/CuO surface through capture by receptor antibody, a decrease in impedance is measured. These results indicate that there is increased negative charge accumulation due the effect of bound antigen's net charge. Therefore, the decrease in impedance can be interpreted as a decrease in overall positive charge with increased caspase-9 loading. This dominant capacitive behaviour can be observed in the Bode magnitude and phase plots in the ranges from 6000 Ω to 10000 Ω and from -50^{o} to -70^{o} in **Fig. 4.6a** and **4.6b** respectively.

Using the logarithmic regression model on the capacitance data (**Fig. 4.6b**), the limit of detection (LOD) of the experiment was defined as 0.07 U/mL (0.032 µM) with a confidence level higher than 95% when ± 2σ (0.286 pF) was considered. The regression line associated with the data from the sensor has a R^2 value of 0.9852, indicating high degree of correlation in the observed data. A statistical analysis of the impedance values taken at a frequency of 6 MHz is shown in **Table 4.1**. The interassay %CV is calculated to be 8.17 % demonstrating high degree of reproducibility.

Caspase-9 (U/mL)	Average |Z| (Ω)	ST DEV	CV (%)
0	5440.104792	464.8039	8.544024
0.1	4454.39874	356.232	7.997309
0.25	3588.922833	160.607	4.475074
0.5	3167.860615	276.6673	8.73357
1	2750.677673	314.0749	11.41809
2	2339.656479	184.1654	7.87147

Table 4.1. Data analysis on impedance values for each caspase-9 concentration at 6 MHz. The %CV = (Standard Deviation/Mean*100) was used to compare variation.

It has been reported that an increase in protein load can result in a reduction in protein solution impedance [201]. To determine if this was the case, impedance measurements of caspase-9 were performed on non-functionalised surfaces. It can be seen from the dose response curves that there was a small reduction in impedance magnitude with the initial concentrations of caspase 9 (**Fig. 4.7c**). This was likely a result of non-specific interactions at the electrode-electrolyte interface caused by electrostatic interactions and other physical adsorption processes. However, despite this, the addition of recognition layer resulted in significantly larger signal outputs relative to the control, $p = 0.02$ (Kruskal-Wallis test).

The selectivity of the antibody-functionalized immunosensor for caspase-9 was tested by comparing the EIS signal changes brought about by two other caspase proteins: caspase-3 and caspase-8. **Figure 4.8d** compares the EIS responses of the immunosensor for 0.5 and 2 U/mL of caspase-3 and caspase-8 solutions in the absence of caspase-9. The results showed that caspase-3 and caspase-8 did not exhibit any significant decrease in impedance magnitude. In contrast to the incubation of the immunosensor in 2 U/mL caspase-9, the resulting

impedance greatly decreased. For both concentrations tested for caspase-3 and caspase-8, the resulting readings were not statistically significant compared to the buffer control ($p \leq 0.05$) (**Fig. 4.8d**).

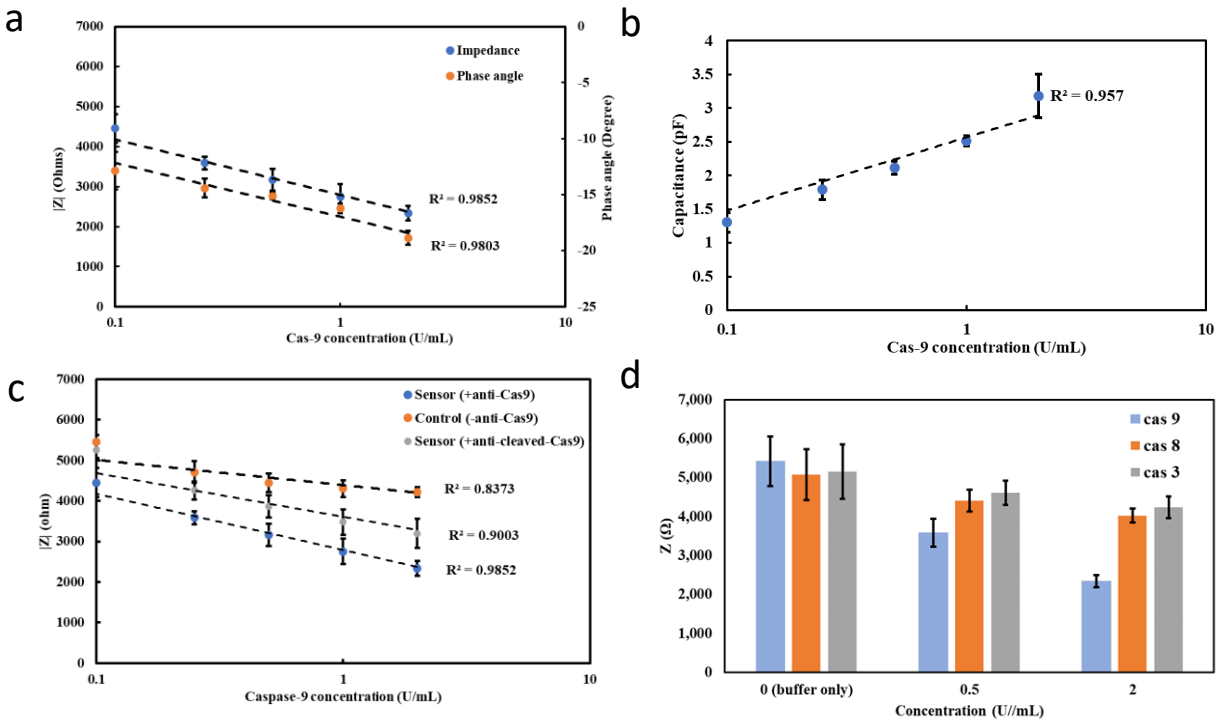

Figure 4.8. (a) Impedance magnitude (●) and phase angle (●) values recorded at 6 MHz from sensor with 200 ng capture antibody tested with PBS spiked with increasing concentrations of caspase-9: 0.1, 0.25, 0.5, 1, 2 U/mL. (b) Capacitance measurements vs caspase-9 concentration (0.1, 0.25, 0.5, 1, 2 U/mL). (c) Impedance plot comparing the responses from cas-9 antibody (●), cleaved cas-9 antibody (●) and control (●). Control experiments were conducted without anti-cas-9 functionalisation. Because of logarithmic scale buffer reading is represented at 0.01 U/mL Cas-9 concentration. Error bars represent 1 standard deviation (n=5). (d) Specificity of the caspase-9 (●) sensor. Interferents of caspase-3 (●) and caspase-8 (●) were tested. Error bars represent 1 standard deviation (n=5).

4.3.2.3 Equivalent electrical circuit modelling

The explanation of obtained experimental results can be completed with the help of the appropriate equivalent circuits that simultaneously fit to the sensor design and to experimental dependencies **(Fig. 4.9**). The equivalent circuit was deduced from the obtained experimental data presented in **Fig. 4.8**. The data for each element of the equivalent circuit are summarised in **Table 4.2**.

The measured impedance change, identified as non-faradaic, is dominated by the capacitance of the double layer formed at the sensing electrode-fluid interface. And for the biosensor described in this work, the impedance change can be attributed to the change in number of binding events at the biosurface-solution interface. Small changes in the number of binding events can result in changes in capacitance (fF~pF changes). Similar capacitive biosensors have been reported [229], where two measurement electrodes are positioned underneath an insulating layer to measure the capacitance of the biosensor, as the dielectric properties of the solution changes with the total number of biorecognition events.

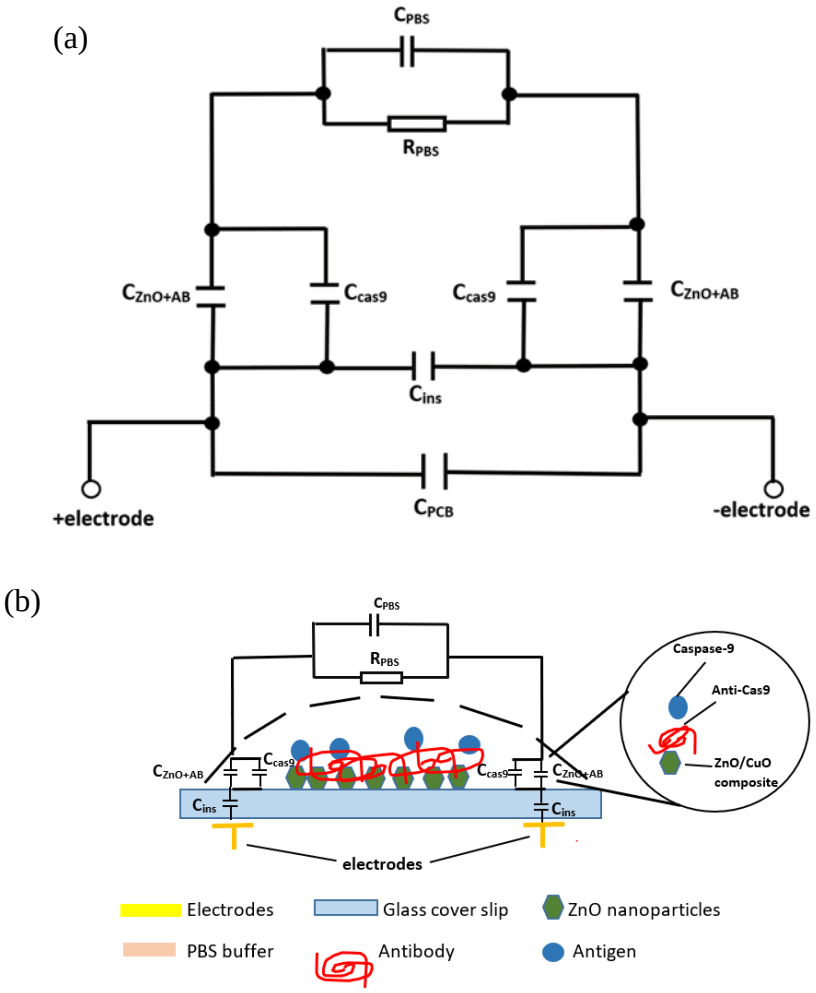

Figure 4.9. (a) Equivalent circuit model for the biosensor. Measured capacitance comprised of four capacitors including the fixed capacitance of the insulator, C_{ins}, the interfacial capacitance associated with ZnO/CuO and caspase-9 antibodies, C_{ZnO+AB}, the caspase-9 binding capacitance which reflects when the target protein binds to the capture antibody bound to the ZnO/CuO surface, C_{cas9}, and the PBS buffer bulk capacitance and resistance, C_{PBS} and R_{PBS}. (b) Cross-sectional image of the biosensor.

The total capacitance of the sensor could be depicted as a network of several capacitors. The first capacitor, Cins, constitutes the insulating layer of borosilicate glass on the electrode surface and represents the fixed dielectric constant of the insulator capacitance. The second

capacitor, C_{ZnO+AB}, includes the capacitance of the ZnO-CuO nanofilm and anti-caspase9 molecular layer and this represents the capacitance formed at the contact surface between the sensor and the bioreceptor layer. The third capacitor, C_{cas9}, represents a capacitance associated by the concentration-dependent biomolecular interactions between caspase-9 and its antibody at the biosensor surface. The bulk PBS impedance is modelled as parallel circuit containing C_{pbs} and R_{pbs}, capacitance and resistance (400 Ω, calculated from conductivity of the ionic solution). As can be seen in **Table 4.2**, the parameters prescribed to the caspase-9 binding events have the largest influence. At the highest concentration of caspase-9, the deduced capacitance values were 13-fold higher compared to the PBS only controls.

Equivalent component	PBS	PBS/Cas9 [0.1 U/mL]	PBS/Cas9 [0.25 U/mL]	PBS/Cas9 [0.5 U/mL]	PBS/Cas9 [1 U/mL]	PBS/Cas9 [2 U/mL]
C_{ins} [fF]	85.34	85.34	85.34	85.34	85.34	85.34
C_{ZnO+AB} [fF]	26.11	26.11	26.11	26.11	26.11	26.11
C_{cas9} [fF]	190.4	765.38	1246.88	1575.1	1974.65	2639.18

Table 4.2. Calculated capacitance values (at 6 MHz). Equivalent circuit components. C_{ins}: insulator capacitance, C_{ZnO+AB}: interfacial capacitance associated with ZnO/CuO and caspase-9 antibodies, C_{cas9}: caspase-9 binding capacitance.

4.3.3 Detection of caspase-9 in the culture media

To test the impedimetric biosensor's ability to detect caspase release in mammalian cell culture, CHO-K1 cells were subjected to a cell death stimulus (staurosporine) which can effectively trigger apoptosis [230]. Zhang et al. [231] demonstrated that CHO-K1 cells treated with staurosporine exhibit distinct apoptotic phenotypes including nuclear condensation, DNA fragmentation and cell shrinkage. These apoptotic phenotypes are associated with an increase in cellular caspase activity [231]. Staurosporine (1 μM) was added to the cell culture medium to initiate apoptosis.

4.3.3.1 Morphological characterisation of apoptosis in CHO cell culture

Morphologic criteria are considered reliable evidence of apoptosis. However, demonstration of complete apoptotic morphology by a single method is difficult. Nuclear condensation, shrinkage of the cell and fragmentation into apoptotic bodies can be visualised using light microscopy [232]. **Fig. 4.10** shows the clear differences in cell morphology between healthy CHO cells and staurosporine-treated cells. Within 6 hours, condensation of cytoplasm, organelles and membrane (pyknosis) and nuclear fragmentation (karyorrhexis) can be observed. Another key feature of apoptotic morphology is the separation of neighbouring cells, and this is a result of cell shrinkage and cell death via secondary necrosis (**Fig. 4.10c and 4.10d**). Also to note, the asynchronous nature of apoptotic cell death in cell populations is mainly due to the variable duration of the initiation phase. As a result, imaging methods alone may not capture the true extent of apoptotic progression across the entire cell population. Cell viability was assessed by trypan blue staining. The results show a significant drop (10%) in viability after 3 hours of staurosporine treatment (**Fig. 4.10e**). The untreated controls did not display any morphological signs of apoptosis or loss of cell viability.

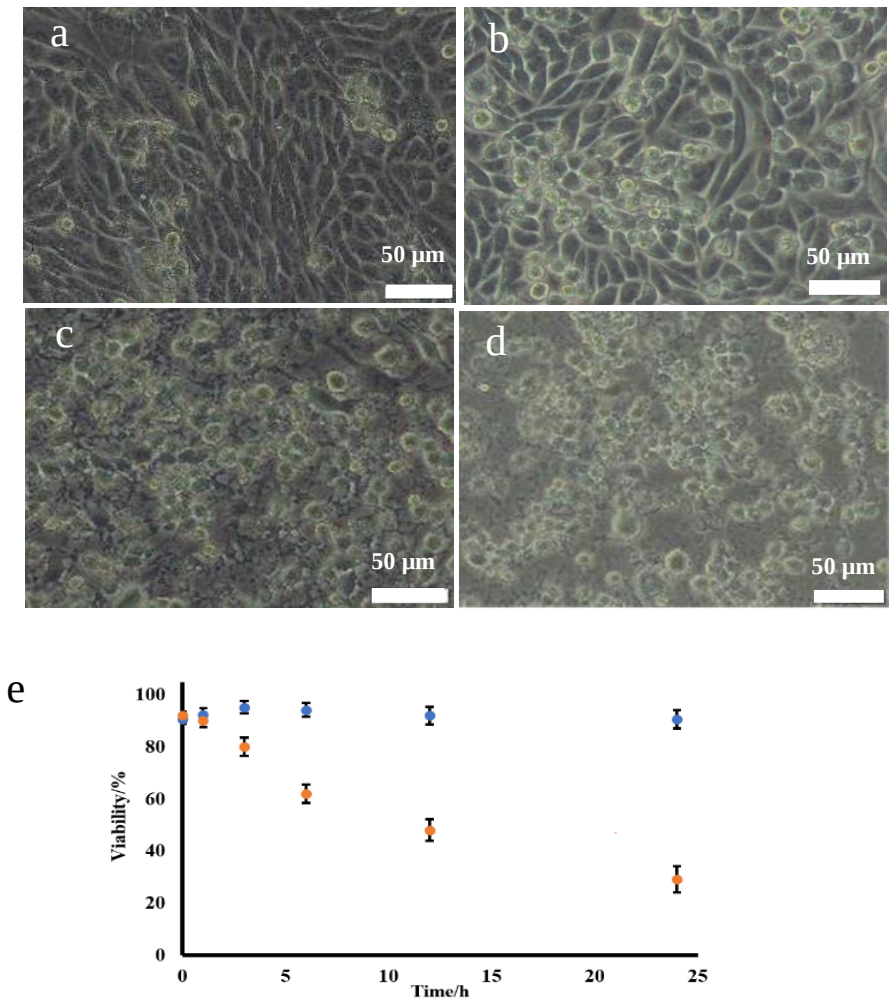

Figure 4.10. Bright-field microscope images of CHO-K1 cells incubated for, (a) 6 h and (b) 24 h, at 37°C. Images of CHO-K1 cells treated with 1 µM staurosporine and incubated for (c) 6 h and (d) 24 h, at 37°C. (e) Cell viability assay analysis of staurosporine (1 µM) treated (●) and non-treated (●) CHO-K1 cells. Error bars (1 σ) are shown (n=6).

Fig. 4.11a. illustrates the morphological progression of apoptosis. As expected, the nuclear size reduced as apoptosis progressed by ~24.273% (75.152 – 56.91 µm^2) over the 8-hour time window. The rate of reduction is calculated to be ~3.03% per hour. The greatest size reduction was seen between the intervals, 6 and 8 hours: ~10.66% (63.7– 56.91 µm^2).

Statistical analysis using the (2-tailed) Pearson Correlation confirmed that there is a significant negative relationship between staurosporine exposure time and nuclear area reduction: Pearson Correlation of determination = -0.993, p value = 0.001.

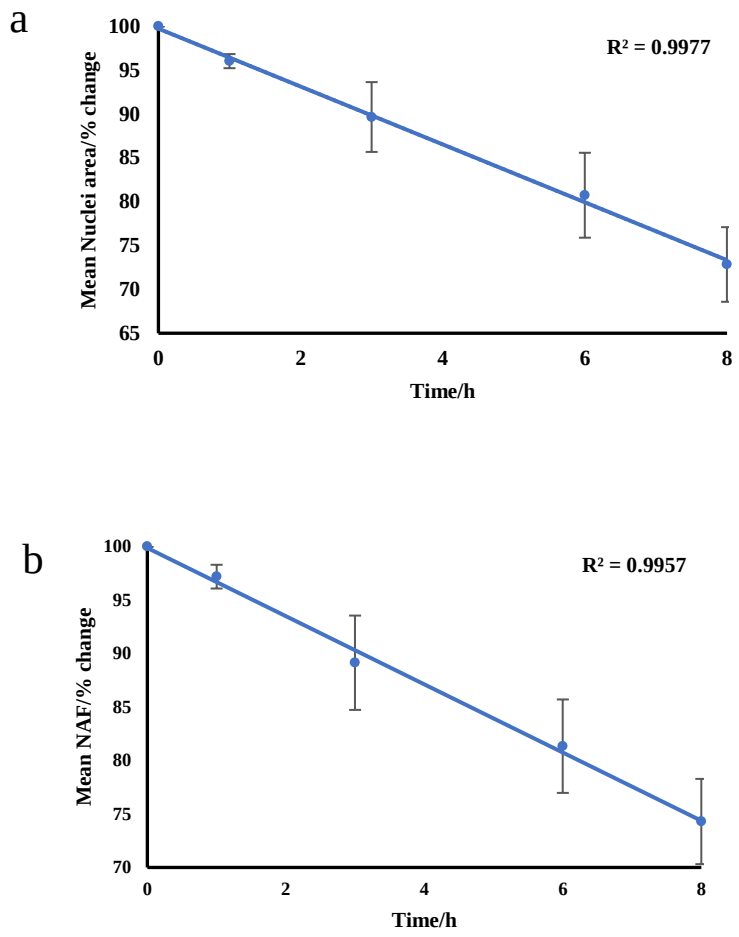

Figure 4.11. (a) The mean % change of the nuclear area (μm^2) with respect to exposure of staurosporine. (b) The mean % change of the Nuclear Area Factor (NAF) with respect to exposure of staurosporine. The NAF calculation entailed: nuclear area/circularity. The % change of the mean nuclei area and NAF was calculated and compared against each other over the 8 hour period. Time point 0hr was the initial point (100% = whole nuclei). Mean + standard error of the mean is shown.

A more robust measure of apoptosis is the Nuclear Area Factor (NAF) [217,218,233]. NAF is a quantitative method: nuclear area/circularity, where a low NAF value indicates greater cell death. Circularity is a measurement supplied by ImageJ, which determines whether an object is a perfect circle: $4\pi(\text{area}/\text{perimeter}^2)$. The score would be between 0 (polygon shape) and 1.0 (perfect circle) [217,218,233,234]. Over the 8-hour period the mean NAF reduced overall by ~22.634% (88.236 – 68.265). **Fig. 4.11b** illustrates this negative trend, similar to **Fig. 4.11a**, NAF decreases as apoptosis progresses and was substantiated using the Pearson Correlation test: Pearson Correlation Coefficient = -0.994, p= 0.001.

4.3.3.2 Enzymatic detection of caspase-9 in CHO cell culture

For biochemical measurements for apoptosis, luminescent caspase-9 assays were performed using a commercially available test kit as described in the Experimental **Section 4.2.8**. The assay uses a luminogenic substrate containing a caspase specific sequence. Following caspase cleavage, amino luciferin is released, resulting in the luciferase reaction and the production of light. The effect of staurosporine exposure on caspase-9 activity was monitored over a 24-hour timeframe (1, 3, 6 and 24 hour). The signal generated is proportional to the amount of caspase activity present. A twofold increase in caspase-9 activity was observed following 6 hours exposure to staurosporine (**Fig. 4.12a**). No significant change in caspase activity was detected in the control samples (**Fig. 4.12a**). The results are consistent with previous literature. For example, Mokhtar *et al.* [235] measured a significant increase in LEHD-cleaving activity in HEK293T cells 4 hours following apoptosis induction.

a

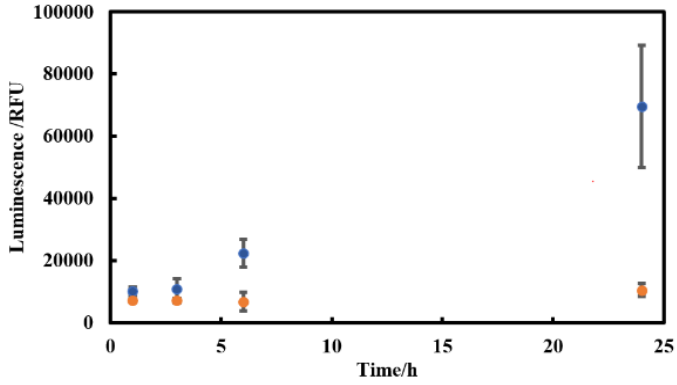
Luminescence /RFU
100000
80000
60000
40000
20000
0
0
5
10
15
20
25
Time/h

b

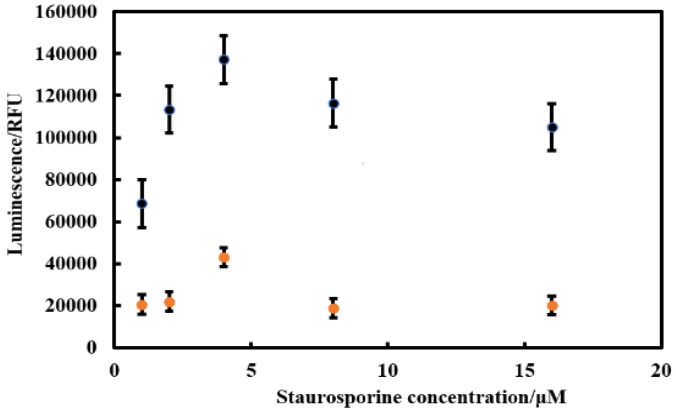
Luminescence/RFU
160000
140000
120000
100000
80000
60000
40000
20000
0
0
5
10
15
20
Staurosporine concentration/μM

c

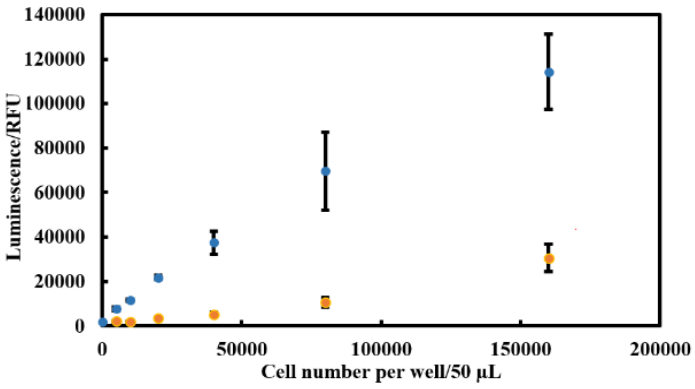
Luminescence/RFU
140000
120000
100000
80000
60000
40000
20000
0
0
50000
100000
150000
200000
Cell number per well/50 μL

d

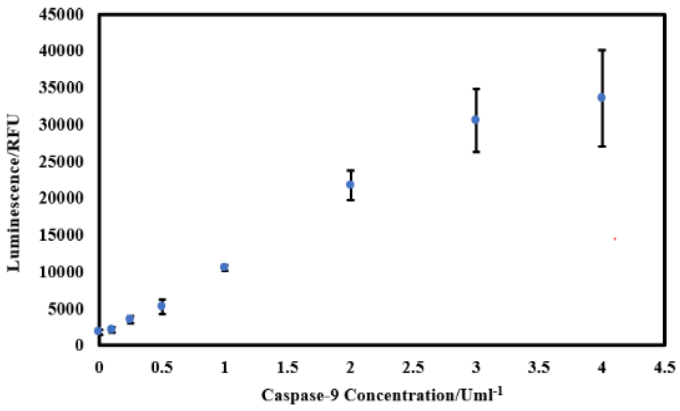
Luminescence/RFU
45000
40000
35000
30000
25000
20000
15000
10000
5000
0
0
0.5
1
1.5
2
2.5
3
3.5
4
4.5
Caspase-9 Concentration/Uml-1

Figure 4.12. Caspase activity assays. (a) CHO-K1 cells were subjected to 1 μM of staurosporine exposure for 1, 3, 6 and 24 hours. (b) CHO-K1 cells were exposed to varying concentrations of staurosporine (1, 2, 4, 8 and 16 μM) for 24 hours. (c) CHO-K1 (varying starting cell number) were subjected to 1 μM of staurosporine and incubated for 24 hours. Treated (●) and untreated controls (●) were plotted and errors bars (1 σ) are shown (n=5). Controls refer to the cell samples without exposure to staurosporine. (d) Caspase activity assay with standard concentrations of caspase-9 (0.1, 0.25, 0.5, 1, 2, 3, 4 U/mL). Error bars (1 σ) are shown (n=6).

To gain further insight into the staurosporine induced caspase activation and caspase release, an experiment using different starting cell numbers (5000, 10000, 20000, 40000, 80000, 160000 cells/50 μL) was conducted. These specific cell numbers were used to represent a high-density CHO culture process at the end of the exponential growth phase, as the culture becomes confluent and cell concentration reaches above 1,000,000 cells/mL. By varying the starting cell number, total caspase activity and production should differ in response to the same drug treatment. The results show a linear relationship between caspase activity and increasing cell number (**Fig. 4.12c**), this is reflective of increasing caspase concentration in the culture media and the staurosporine's toxic effect. In the untreated controls, caspase activity also increased with cell number but with significantly lower luminescence values (**Fig. 4.12c**). This is the baseline caspase activity as cells are undergoing the natural apoptotic process.

To determine the relationship between luminescence and caspase-9 activity, the relative fluorescence unit (RFU) values for each of the standard caspase-9 concentrations (0.1, 0.25, 0.5, 1, 2, 3, 4 U/mL) were measured. It can be seen from the plot, the luminescence values are linearly correlated with the concentration of caspase-9 in the range of 0.1 - 2 U/mL (**Fig.**

4.12d) and begin to level off when the concentrations reached 3 U/mL. A statistical analysis of the measured luminescence values for each concentration of caspase-9 is shown in **Table 4.3**. The average CV% is calculated to be 14.2%. This result can be compared to the impedance data in **Fig. 4.8**, where the same concentration range was used, further highlighting the relationship between caspase activity and concentration.

Caspase-9 concentration (U/mL)	Average Luminescence (RFU)	ST DEV	CV (%)
0	1809.33	275.05	15.20
0.1	2094.33	385.92	18.43
0.25	3512.00	531.14	15.12
0.5	5276.00	982.21	18.62
1	10540.00	318.29	3.02
2	21714.00	2045.72	9.42
3	30573.00	4276.00	13.99
4	33574.00	6515.67	19.41

Table 4.3. Data analysis on caspase activity assay for each standard caspase-9 concentration. The %CV = (Standard Deviation/Mean*100) was used to compare variation.

4.3.3.3 Evaluation of caspase-9 in CHO culture with impedance spectroscopy

In order to demonstrate the applicability of the technique for early detection of apoptosis in live cell culture samples, a timed study with the impedimetric biosensor to detect caspase-9 over a six-hour time frame was performed. Following the initial addition of staurosporine, impedance magnitude measurements were taken at 6 MHz at regular intervals. The impedance signal response for each of the six time points is shown in **Fig. 4.13a**. The decrease in impedance magnitude was evident following three hours of exposure to staurosporine, where the mean impedance values were significantly different from the untreated controls with a confidence level higher than 95% ($\pm 2\sigma$). This finding was consistent with the caspase activity assay results shown in **Fig. 4.13b**, as the levels of caspase-9 activity increased linearly between 2 to 6 hours. Background apoptotic activity is expected in the cell culture. This is due to cellular debris resulting from low level cell break-down detected being detected through interactions on the sensor surface. This was shown to result in 9.8% change in impedance over 6 hours in the untreated culture samples (**Fig. 4.13a**). On the other hand, a 46.4% change in impedance was recorded in the staurosporine samples over the same time frame (**Fig. 4.13a**).

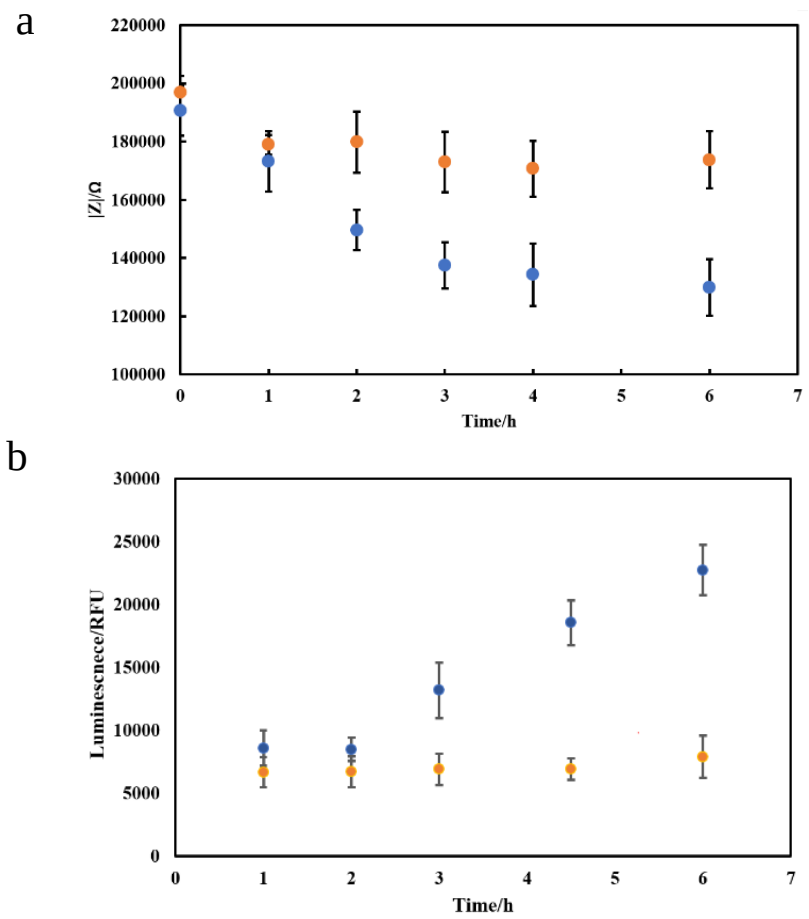

Figure 4.13. Timed measurements of caspase-9 levels with impedance and caspase activity assay in the first six hours (a) Impedance analysis (6 MHz) of CHO-K1 cell culture samples following addition of 1 µM staurosporine. (b) Caspase activity recorded in CHO-K1 cell culture samples following addition of 1 µM staurosporine. Treated (●) and untreated controls (●) were plotted and errors bars (1 σ) are shown (n=5).

Impedimetric biosensing and caspase activity assays were also performed for cell culture samples with defined cell concentrations and the relationship between caspase-9 activity and concentration was explored (**Fig. 4.14**). In this study, these specific cell numbers were used to represent a high-density CHO culture process at the end of the exponential growth phase, as

the culture becomes confluent and cell concentration reaches above 1,000,000 cells/mL. From the caspase activity assay data, it is evident that an increase in the number of cells leads to an increase in caspase-9 activity (RFU readings) for a given toxic challenge (**Fig. 4.14**). The impedance behaviour was consistent with the results from the calibration curve data in **Fig. 4.6**, i.e. a decrease in impedance magnitude was measured with increasing caspase-9 concentration. The decrease in impedance reflects an increase in the overall capacitance of the system. This capacitance change is largely dominated by the charge accumulation as a result of antigen binding with antibody and to a lesser extent, an increase in polarity of the solution due to an increased caspase-9 load [201,228].

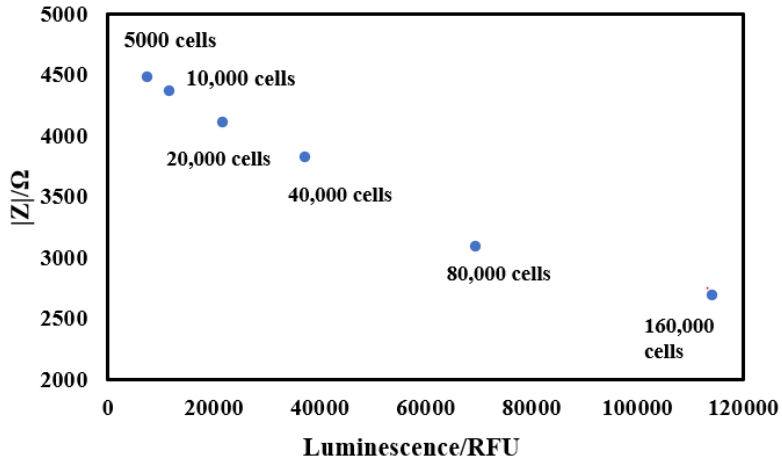

Figure 4.14. Comparison between luminescence readings and impedance output (6 MHz) of CHO-K1 cell culture sample following 24-hour exposure to 1 μM staurosporine. Different starting cell numbers were tested. Higher luminescence reading (higher caspase-9 activity) is correlated with lower impedance output.

We have successfully demonstrated the application of electrical impedance spectroscopy for the detection of early apoptotic markers in cell culture samples before clearly detectable morphological hallmarks are present.

4.4. Conclusions

We have successfully shown the application of impedimetric biosensor technology in the detection of apoptosis and experimentally confirmed the sensor's ability to measure caspase-9. The sensor is fabricated using a simple and inexpensive colloidal sonication technique. It is stable against electrode polarisation and capacitive artefacts especially for the analysis in the mid-high frequency ranges. The sensor was evaluated experimentally with different concentrations of caspase-9 protein solutions and with samples extracted from CHO cell culture. The performance of the biosensor was evaluated with impedance spectroscopy, with a limit of detection of around 0.07 U/mL (0.032 μM) being achieved and it was tested as a proof of concept with culture media spiked with increasing caspase-9 concentrations. The average analysis time (45 minutes including preparation) is shorter than commercial ELISA (at least 2.5 hrs). The sensor can be activated at a single frequency which would further lower the cost of instrumentation and analysis time. Additional benefits of this biosensing technique include the lack of contact between electrodes and measurement matrix. As a result, the charge transfer parameter is negligible, and no redox probes are required. Measurements can be performed with a sample volume of 50 μL without the need for sample dilution for rapid analysis. The biosensor fabrication methodology can be adapted to the measurement of any other analytes where the binding partner can be obtained.

The administration of staurosporine increased apoptotic activity in CHO cells. A significant increase in caspase-9 activity and caspase-9 concentration as early as 3 hours after drug exposure was measured. Therefore, potentially this impedimetric approach may serve as a practical tool for the sensitive, precise and real-time detection of apoptotic cells, complementing the state-of-the-art strategies for apoptosis detection. The current set of experiments was conducted in a 2D cell culture system and may not fully reflect the cell state of CHO cells in suspension in larger bioreactors. Further work will need to be carried out to fully evaluate the sensor in conditions that more closely mimic the bioreactor environment and improve the reproducibility of the sensor fabrication, particularly through the automation of the fabrication process.

Chapter 5
Conclusion

5.1 Key Findings

The overall aim of this research was to develop a non-faradic biosensor for the detection of apoptosis through the measurement of caspase-9 released into cell culture media. In order to demonstrate this five objectives were set and addressed by the experimental work set out in this thesis.

1. **To design and fabricate a sensitive caspase-9 biosensor surface through an investigation of critical parameters, in particular, the ratio of ZnO:CuO and antibody loading associated with functionalisation.**

The caspase biosensor was developed using a mixture of ZnO and CuO. The facile fabrication of nano-surfaces was enabled by the ability to source ZnO and CuO nanoparticles of defined shape and size thus removing the need to synthesis the nanoparticles from precursors. The colloidal dispersion of nanoparticles was achieved using a simple sonication method and a SEM analysis revealed differences in the surface morphology when three different concentrations of ZnO suspension were applied. The formulation of the ZnO/CuO composite film used was optimised to give the highest surface roughness when there was a complete coverage of the substrate. This was found to be a 1% ZnO and 1% CuO. The higher surface roughness contributes to an additional surface area for biological binding when compared to a smooth surface. Antibody was passively adsorbed on to the nanocrystalline surface though electrostatic interactions. The analytical performance of the biosensor is

related to the availability of antibody on the surface to bind caspase-9 when added to the surface. It was found that the optimal antibody loading on the sensor surface was 200 ng.

2. To demonstrate a working ZnO/CuO impedimetric biosensor to caspase-9, with high sensitivity, selectivity and reproducibility.

Caspase-9 measurements made in buffer using the ZnO/CuO biosensors, confirmed a stable and reproducible change in the impedance signal that was related to changing caspase-9 concentrations. The 1% ZnO/1% CuO sensor demonstrated a linear range from 1 – 16 nM, with a limit of detection of 0.33 nM which is far more sensitive that the other caspase-9 biosensor reported in the literature which had a detection limit of 80 nM (see table 3.2). This enhanced sensitivity can be related to the nanostructure of the surface and the frequency of the measurements creates a dynamic double layer which limits charge screening. In addition, a good precision profile was observed when measuring Caspase-9 in cell culture media, with a CV of 4.5% at 0.25 U/mL. This is particularly good considering all sensors are handmade.

The sensor fabrication technique is simple, inexpensive and avoids the use of harsh chemicals. As there is no direct contact between electrodes and the measurement matrix, there is negligible charge transfer, eliminating the need for redox probes. Furthermore, a sample volume as low as 50 μL can be utilised, without requiring sample dilution and thus facilitating rapid analysis. Using a single frequency AC signal simplifies the signal processing, reducing the cost of the instrumentation and the analysis time.

3. **To develop a cell model for apoptosis in CHO cells, using apoptotic agents, which can be validated using optical and enzymatic methods.**

In chapter 4 a cell model was developed using CHO cells with the induction of apoptosis in the cells through staurosporine administration. Apoptosis of the cells caused a significant enhancement in both caspase-9 activity and concentration, evident as early as 3 hours post-exposure to the drug. Two other standard apoptosis detection methods were used to evaluate the apoptotic model and to validate the caspase-9 biosensor. One approach was to use a microscopic examination of cell and nuclear morphology to capture the extent of apoptotic progression in a subset of cell culture. Secondly, an enzymatic assay based on chemiluminescence was deployed to assess caspase-9 activity over time across the entire cell population. The application of staurosporine to induce apoptosis in CHO cells was validated using these two techniques and was deemed a suitable model to test the caspase-9 biosensor.

4. **To demonstrate that the impedimetric biosensor can measure increasing caspase-9 concentrations with higher levels of apoptosis in cell culture media from the CHO cell model.**

The caspase biosensor exhibits a negative dose response to increasing concentrations of caspase-9. When CHO cells were exposed to increasing concentrations of staurosporine, and increasing apoptosis, there was a dose dependent reduction in the impedance signal. This change in impedance signal was correlated with the optical and caspase-9 enzyme activity showing that the caspase-9 biosensor was detecting apoptosis of CHO cells and was able to measure caspase-9 in the cell media in which the cells were growing. A decrease in impedance magnitude was evident following three hours of exposure to staurosporine which was consistent with the caspase activity assay results. There was however, some background

apoptotic activity in the cell culture noted, resulting in low level cell breakdown and cell debris deposition on the sensor surface. However, the difference between the treatment group and control became evident after the 3 hours. This successfully demonstrated the application of electrical impedance spectroscopy for the detection of early apoptotic markers in cell culture samples before clearly detectable morphological hallmarks are present.

The performance of the biosensor was evaluated with impedance spectroscopy and a detection limit of 0.07 U/mL (32 nM) was calculated from dose response curves using culture media spiked with increased caspase-9 concentrations. The difference in the detection limit between the caspase-9 biosensor used in buffer (0.33 nM) and when used in cell culture media can be attributed to low level, background, apoptosis and the fact that cell culture media is a complex matrix containing many proteins and peptides which may exhibit non-specific binding to the biosensor.

5. To develop a theoretical model of a non-faradaic impedimetric, ZnO/CuO biosensor.

A theoretical model was developed that represented the electrical components of a non-faradaic biosensor for the measurement of caspase-9. The modelling approach, described in chapter 2, involved the adaptation of the Randles equivalent circuit to provide a detailed representation of the structure of the nanoparticle based impedimetric sensor. The model considered the composition of each of the different layers of the sensing system: the interfacial surface, the buffer solution, the ZnO/CuO nano-film, glass substrate, the electrodes and casapase-9 substrate. The limitations of the impedance measurement set-up were also defined. Experiments performed and reported in section 4.3.2.3 and table 4.2 verified the

model, showing that the main contribution to the dose dependent signal was the capacitance associated with the antibody/caspase interaction.

5.2 Suggestions for Future Work

5.2.1 Targets

In this study, caspase-9 was used as the analyte of interest to evaluate the sensor's performance under buffer and complex media conditions. The sensor design, including the antibody immobilization process and antibody quantity, the geometry of the sensor and the electrodes could be further optimised to achieve improved performance and compatibility for the detection of apoptosis in a bioreactor setup. However, the versatile nature of the sensor fabrication process and the use of an established detection principle can allow for the adaption of the sensor for detection of various biomarkers, including other apoptotic markers, cardiac biomarkers, cancer biomarkers etc. The principle of detection is based on the interaction between antibody and antigen which results in a change in capacitance at the sensor surface which is measured using non-faradaic impedance spectroscopy. Furthermore, the extent of non-specific binding was evaluated using other caspase proteins, but the selectivity investigation can also be extended using various proteins, hormones, and molecules to establish how the sensor reacts to non-specific binding.

5.2.2 Fabrication and Design

Exploring the active region of the biosensor in more depth has the potential to enhance its performance. Binding interactions that occur within the Debye length of the electrode/electrolyte interface are known to yield significant alterations in the electrical double layer capacitance, suggesting that investigating shorter binding partners could be a viable avenue for improvement. Notably, alterations in electrode dimensions and biorecognition layer thickness will likely impact the electrical double layer capacitance, necessitating careful consideration in any further investigations.

An alternative modification to the sensor design involves altering the surface material, aiming to optimize the immobilization of antibodies for potentially improved performance. For example, the use of graphene may prove to have beneficial effects such as large surface area, electrical conductivity and its capacity to immobilize different molecules [236]. Graphene oxide is widely used due to its capacity to allow for different strategies for antibody attachment [236]. Kailashiya *et al* [237] developed a graphene oxide-based electrochemical sensor for the diagnosis of cardiovascular disease. GO was employed as the matrix as it can be easily functionalized while providing stable and thin conductive layer on electrode surface [237]. It is worth investigating different surface compositions and different surface chemistries to find the optimal fabrication method and thus resulting in improved sensing performance.

The current set of experiments was conducted in a simple 2D cell culture system and may not fully reflect the cell state of CHO cells in suspension in larger bioreactors. Staurosporine was used to accelerate the apoptotic process which otherwise would take days or weeks to occur

in a bioreactor setting. Other factors such as shearing, oxygen levels and nutrient concentrations provided minimal impact on the health of the cell culture in this study but these factors could play an important role in the induction of apoptosis in larger automated bioreactors. Further work will need to be carried out to fully evaluate the sensor in conditions that more closely mimic the bioreactor environment and improve the reproducibility of the sensor fabrication, particularly through the automation of the fabrication process.

5.2.3 Evaluation of background activity

Avoiding and recognizing matrix effects in complex samples is important, where components other than the target analyte influence biosensor response. Background apoptotic activity was observed in the untreated cell cultures evidenced by the difference in impedance signal between the treated and the control sample. It was hypothesized in this study that the changes in impedance was due to cell debris interacting with the surface due to low-level cellular breakdown. However, the rate at which normal cellular occurs may differ from the staurosporine induced apoptotic progression. Additional research and repeated experimentation are required to identify a consistent signal line indicative of background activity. Employing signal processing techniques to eliminate background noise from the signal line enables the differentiation between stress-induced apoptosis and the inherent apoptotic processes. Additionally, exploring the influence of minor changes in bioreactor conditions on the background signal could provide valuable insights.

5.2.4 Future applications

In addition to the improvements discussed in the sections above many steps are needed for the caspase-9 biosensor presented in the thesis to have future applications in an industrial bioreactor. The system needs to be optimised for the chosen target and careful control of the fabrication processes will be required to ensure reproducibility. A fluid system could allow for consistent flow through the active sensor regions and enclosing the sensor in a case would help limit the sensor's exposure to external environment. A comprehensive electrical circuit model will need to be developed and fitted to the experimental data to reveal the impedance contribution of each constituent component of the sensor. Thorough testing of the system with real samples and within industrial settings will be crucial to validate the sensors' utility and practicality as a tool for apoptosis detection.

References

1. Ecker, D., Crawford, T. & Seymour, P. MAb Products: Market Trends and Projections - BioProcess InternationalBioProcess International. https://bioprocessintl.com/business/economics/the-market-for-therapeutic-mab-products/ (2020).

2. Dietmair, S., Nielsen, L. K. & Timmins, N. E. Mammalian cells as biopharmaceutical production hosts in the age of omics. *Biotechnol J* **7**, 75–89 (2012).

3. Tripathi, N. K. & Shrivastava, A. Recent Developments in Bioprocessing of Recombinant Proteins: Expression Hosts and Process Development. *Front Bioeng Biotechnol* **7**, 420 (2019).

4. Jozala, A. F. *et al.* Biopharmaceuticals from microorganisms: from production to purification. *Brazilian Journal of Microbiology* **47**, 51–63 (2016).

5. Krampe, B. & Al-Rubeai, M. Cell death in mammalian cell culture: molecular mechanisms and cell line engineering strategies. *Cytotechnology* **62**, 175–88 (2010).

6. Krause, M., Neubauer, A. & Neubauer, P. The fed-batch principle for the molecular biology lab: Controlled nutrient diets in ready-made media improve production of recombinant proteins in Escherichia coli. *Microb Cell Fact* **15**, 1–13 (2016).

7. Yun, C. Y. *et al.* Specific inhibition of caspase-8 and -9 in CHO cells enhances cell viability in batch and fed-batch cultures. *Metab Eng* **9**, 406–418 (2007).

8. Bielser, J. M., Wolf, M., Souquet, J., Broly, H. & Morbidelli, M. Perfusion mammalian cell culture for recombinant protein manufacturing – A critical review. *Biotechnol Adv* **36**, 1328–1340 (2018).

9. Mercille, S., Johnson, M., Lanthier, S. P., Kamen, A. A. & Massie, B. Understanding Factors that Limit the Productivity of Suspension-Based Perfusion Cultures Operated at High Medium Renewal Rates. *Biotechnol Bioeng* **67**, 435–450 (2000).

10. Degterev, A. & Yuan, J. Expansion and evolution of cell death programmes. *Nat Rev Mol Cell Biol* **9**, 378–390 (2008).

11. Patil, A. A., Bhor, S. A. & Rhee, W. J. Cell death in culture: Molecular mechanisms, detections, and inhibition strategies. *Journal of Industrial and Engineering Chemistry* vol. 91 37–53 Preprint at https://doi.org/10.1016/j.jiec.2020.08.009 (2020).

12. Kroemer, G. *et al.* Classification of cell death: Recommendations of the nomenclature committee on cell death. *Cell Death Differ* **12**, 1463–1467 (2005).

13. Kerr, J. F. R., Wyllie, A. H. & Currie, A. R. Apoptosis: a basic biological phenomenon with wide-ranging implications in tissue kinetics. *Br J Cancer* **26**, 239–257 (1972).

14. Chen, Q., Kang, J. & Fu, C. The independence of and associations among apoptosis, autophagy, and necrosis. *Signal Transduction and Targeted Therapy 2018 3:1* **3**, 1–11 (2018).

15. Kono, H. & Rock, K. L. How dying cells alert the immune system to danger. *Nature Reviews Immunology* vol. 8 279–289 Preprint at https://doi.org/10.1038/nri2215 (2008).

16. Gump, J. M. & Thorburn, A. Autophagy and apoptosis: what is the connection? *Trends Cell Biol* **21**, 387–392 (2011).

17. Dhuriya, Y. K. & Sharma, D. Necroptosis: a regulated inflammatory mode of cell death. *Journal of Neuroinflammation 2018 15:1* **15**, 1–9 (2018).

18. D'Arcy, M. S. Cell death: a review of the major forms of apoptosis, necrosis and autophagy. *Cell Biology International* Preprint at https://doi.org/10.1002/cbin.11137 (2019).

19. Nikoletopoulou, V., Markaki, M., Palikaras, K. & Tavernarakis, N. Crosstalk between apoptosis, necrosis and autophagy. *Biochimica et Biophysica Acta (BBA) - Molecular Cell Research* **1833**, 3448–3459 (2013).

20. Saraste, A. & Pulkki, K. Morphologic and biochemical hallmarks of apoptosis. *Cardiovasc Res* **45**, 528–537 (2000).

21. Marquez, R. T. & Xu, L. Bcl-2:Beclin 1 complex: multiple, mechanisms regulating autophagy/apoptosis toggle switch. *Am J Cancer Res* **2**, 214 (2012).

22. Pasquier, B. Autophagy inhibitors. *Cellular and Molecular Life Sciences 2015 73:5* **73**, 985–1001 (2015).

23. Xu, X. *et al.* The genomic sequence of the Chinese hamster ovary (CHO)-K1 cell line. *Nat Biotechnol* **29**, (2011).

24. Tang, H. L., Tang, H. M., Fung, M. C. & Hardwick, J. M. In vivo Caspase tracker biosensor system for detecting anastasis and non-apoptotic caspase activity. *Sci Rep* **5**, 1–7 (2015).

25. Elmore, S. Apoptosis: A Review of Programmed Cell Death. *Toxicologic Pathology* vol. 35 495–516 Preprint at https://doi.org/10.1080/01926230701320337 (2007).

26. Aggarwal, B. B. Signalling pathways of the TNF superfamily: a double-edged sword. *Nat Rev Immunol* **3**, 745–756 (2003).

27. Bao, Q. & Shi, Y. Apoptosome: A platform for the activation of initiator caspases. *Cell Death and Differentiation* vol. 14 56–65 Preprint at https://doi.org/10.1038/sj.cdd.4402028 (2007).

28. Martinez, M. M., Reif, R. D. & Pappas, D. Detection of apoptosis: A review of conventional and novel techniques. *Analytical Methods* vol. 2 996–1004 Preprint at https://doi.org/10.1039/c0ay00247j (2010).

29. Riedl, S. J. & Shi, Y. Molecular mechanisms of caspase regulation during apoptosis. *Nature Reviews Molecular Cell Biology* vol. 5 897–907 Preprint at https://doi.org/10.1038/nrm1496 (2004).

30. Wei, Y. Y. C. *et al.* Proteomics analysis of chinese hamster ovary cells undergoing apoptosis during prolonged cultivation. *Cytotechnology* **63**, 663–677 (2011).

31. Sgonc, R. & Gruber, J. Apoptosis detection: an overview. *Exp Gerontol* **33**, 525–533 (1998).

32. Banfalvi, G. Methods to detect apoptotic cell death. *Apoptosis* **22**, 306–323 (2017).

33. Izquierdo, A., Casas, C. & Herrero, E. Selenite-induced cell death in Saccharomyces cerevisiae: Protective role of glutaredoxins. *Microbiology (N Y)* **156**, 2608–2620 (2010).

34. Yasuhara, S. *et al.* Comparison of comet assay, electron microscopy, and flow cytometry for detection of apoptosis. *Journal of Histochemistry and Cytochemistry* **51**, 873–885 (2003).

35. Madeo, F. *et al.* A Caspase-Related Protease Regulates Apoptosis in Yeast. *Mol Cell* **9**, 911–917 (2002).

36. Koopman, G. *et al.* Annexin V for Flow Cytometric Detection of Phosphatidylserine Expression on B Cells Undergoing Apoptosis. *Blood* **84**, 1415–1420 (1994).

37. Yu, B. *et al.* Assessing Apoptosis Gene Expression Profiling with a PCR Array in the Hippocampus of Ts65Dn Mice. *Biomed Res Int* **2015**, (2015).

38. Smith, C. J. & Osborn, A. M. Advantages and limitations of quantitative PCR (Q-PCR)-based approaches in microbial ecology. *FEMS Microbiol Ecol* **67**, 6–20 (2009).

39. Kumar, A. *et al.* Converging Evidence of Mitochondrial Dysfunction in a Yeast Model of Homocysteine Metabolism Imbalance. *Journal of Biological Chemistry* **286**, 21779–21795 (2011).

40. Ludovico, P. *et al.* Cytochrome c release and mitochondria involvement in programmed cell death induced by acetic acid in Saccharomyces cerevisiae. *Mol Biol Cell* **13**, 2598–2606 (2002).

41. Schwamb, S. *et al.* Monitoring CHO cell cultures: Cell stress and early apoptosis assessment by mass spectrometry. *J Biotechnol* **168**, 452–461 (2013).

42. Butterick, T. A. *et al.* Use of a Caspase Multiplexing Assay to Determine Apoptosis in a Hypothalamic Cell Model. *J Vis Exp* 51305 (2014) doi:10.3791/51305.

43. Taatjes, D. J., Sobel, B. E. & Budd, R. C. Morphological and cytochemical determination of cell death by apoptosis. *Histochem Cell Biol* **129**, 33 (2008).

44. Banfalvi, G. Methods to detect apoptotic cell death. *Apoptosis* **22**, 306–323 (2017).

45. Hu, X. M. *et al.* Guidelines for Regulated Cell Death Assays: A Systematic Summary, A Categorical Comparison, A Prospective. *Front Cell Dev Biol* **9**, 368 (2021).

46. Paludan, S. R., Reinert, L. S. & Hornung, V. DNA-stimulated cell death: implications for host defence, inflammatory diseases and cancer. *Nature Reviews Immunology 2019 19:3* **19**, 141–153 (2019).

47. Kroemer, G. *et al.* Classification of cell death: Recommendations of the Nomenclature Committee on Cell Death 2009. *Cell Death and Differentiation* Preprint at https://doi.org/10.1038/cdd.2008.150 (2009).

48. Wimmer, K., Sachet, M. & Oehler, R. Circulating biomarkers of cell death. *Clin Chim Acta* **500**, 87–97 (2020).

49. Banerjee, P. P., Banerjee, S. & Brown, T. R. Bcl-2 Protein Expression Correlates with Cell Survival and Androgen Independence in Rat Prostatic Lobes. *Endocrinology* **143**, 1825–1832 (2002).

50. Dong, H. *et al.* Rapid detection of apoptosis in mammalian cells by using intact cell MALDI mass spectrometry. *Analyst* **136**, 5181–5189 (2011).

51. Singhal, N., Kumar, M., Kanaujia, P. K. & Virdi, J. S. MALDI-TOF mass spectrometry: An emerging technology for microbial identification and diagnosis. *Front Microbiol* **6**, 791 (2015).

52. Vigneshvar, S., Sudhakumari, C. C., Senthilkumaran, B. & Prakash, H. Recent advances in biosensor technology for potential applications - an overview. *Front Bioeng Biotechnol* **4**, 11 (2016).

53. Mehrotra, P. Biosensors and their applications – A review. *J Oral Biol Craniofac Res* **6**, 153 (2016).

54. Tetyana, P., Shumbula, P. M. & Njengele-Tetyana, Z. Biosensors: Design, Development and Applications. *Nanopores* (2021) doi:10.5772/INTECHOPEN.97576.

55. Clark, L. C. & Lyons, C. ELECTRODE SYSTEMS FOR CONTINUOUS MONITORING IN CARDIOVASCULAR SURGERY. *Ann N Y Acad Sci* **102**, 29–45 (1962).

56. Lucarelli, F., Tombelli, S., Minunni, M., Marrazza, G. & Mascini, M. Electrochemical and piezoelectric DNA biosensors for hybridisation detection. *Anal Chim Acta* **609**, 139–159 (2008).

57. Fu, Z., Lu, Y.-C. & Lai, J. J. Recent Advances in Biosensors for Nucleic Acid and Exosome Detection. *Chonnam Med J* **55**, 86 (2019).

58. Kaushik, A. *et al.* A sensitive electrochemical immunosensor for label-free detection of Zika-virus protein. *Sci Rep* **8**, (2018).

59. Tuteja, S. K. *et al.* A label-free electrochemical immunosensor for the detection of cardiac marker using graphene quantum dots (GQDs). *Biosens Bioelectron* **86**, 548–556 (2016).

60. Dervisevic, M., Alba, M., Adams, T. E., Prieto-Simon, B. & Voelcker, N. H. Electrochemical immunosensor for breast cancer biomarker detection using high-density silicon microneedle array. *Biosens Bioelectron* **192**, 113496 (2021).

61. Ma, J., Sengupta, M. K., Yuan, D. & Dasgupta, P. K. Speciation and detection of arsenic in aqueous samples: a review of recent progress in non-atomic spectrometric methods. *Anal Chim Acta* **831**, 1–23 (2014).

62. Mandelkow, R. *et al.* Detection and quantification of nuclear morphology changes in apoptotic cells by fluorescence microscopy and subsequent analysis of visualized fluorescent signals. *Anticancer Res* **37**, (2017).

63. Hochreiter, B. *et al.* Fluorescent Proteins as Genetically Encoded FRET Biosensors in Life Sciences. *Sensors* **15**, 26281–26314 (2015).

64. Edgington-Mitchell, L. E. & Bogyo, M. Detection of active caspases during apoptosis using fluorescent activity-based probes. in *Methods in Molecular Biology* vol. 1419 27–39 (Humana Press Inc., 2016).

65. Demchenko, A. P. Beyond annexin V: fluorescence response of cellular membranes to apoptosis. *Cytotechnology* **65**, 157–72 (2013).

66. Li, Y. Chemiluminescent determination of the activity of caspase-3 using a specific peptide substrate and magnetic beads. *Microchimica Acta 2012 177:3* **177**, 443–447 (2012).

67. Mali, S. M. *et al.* Heterostructural CuO–ZnO Nanocomposites: A Highly Selective Chemical and Electrochemical NO2 Sensor. *ACS Omega* **4**, 20129–20141 (2019).

68. Pan, Y. *et al.* Colorimetric detection of apoptosis based on caspase-3 activity assay using unmodified gold nanoparticles. *Chemical Communications* **48**, 997–999 (2012).

69. Wang, H. *et al.* Graphene Oxide-Peptide Conjugate as an Intracellular Protease Sensor for Caspase-3 Activation Imaging in Live Cells. *Angewandte Chemie International Edition* **50**, 7065–7069 (2011).

70. Sang, S. *et al.* Progress of new label-free techniques for biosensors: a review. *http://dx.doi.org/10.3109/07388551.2014.991270* **36**, 465–481 (2015).

71. Gibson, N. *et al.* Radiolabelling of engineered nanoparticles for in vitro and in vivo tracing applications using cyclotron accelerators. *Arch Toxicol* **85**, 751–773 (2011).

72. Zhang, Y. *et al.* Label-free electrochemical immunosensor based on enhanced signal amplification between Au@Pd and CoFe2O4/graphene nanohybrid. *Scientific Reports 2016 6:1* **6**, 1–8 (2016).

73. Welch, N. G., Scoble, J. A., Muir, B. W. & Pigram, P. J. Orientation and characterization of immobilized antibodies for improved immunoassays (Review). *Biointerphases* **12**, 02D301 (2017).

74. Menti, C., Henriques, J. A. P., Missell, F. P. & Roesch-Ely, M. Antibody-based magneto-elastic biosensors: potential devices for detection of pathogens and associated toxins. *Applied Microbiology and Biotechnology 2016 100:14* **100**, 6149–6163 (2016).

75. Goddard, J. M. & Hotchkiss, J. H. Polymer surface modification for the attachment of bioactive compounds. *Prog Polym Sci* **32**, 698–725 (2007).

76. Singh, N. K., Thungon, P. D., Estrela, P. & Goswami, P. Development of an aptamer-based field effect transistor biosensor for quantitative detection of Plasmodium falciparum glutamate dehydrogenase in serum samples. *Biosens Bioelectron* **123**, 30–35 (2019).

77. Justino, C. I. L. *et al.* Disposable immunosensors for C-reactive protein based on carbon nanotubes field effect transistors. *Talanta* **108**, 165–170 (2013).

78. Song, H. Y., Zhou, X., Hobley, J. & Su, X. Comparative study of random and oriented antibody immobilization as measured by dual polarization interferometry and surface plasmon resonance spectroscopy. *Langmuir* **28**, 997–1004 (2012).

79. Wahab, H. A. *et al.* Zinc oxide nano-rods based glucose biosensor devices fabrication. *Results Phys* **9**, 809–814 (2018).

80. Ahmad, R. *et al.* Highly Efficient Non-Enzymatic Glucose Sensor Based on CuO Modified Vertically-Grown ZnO Nanorods on Electrode. *Scientific Reports 2017 7:1* **7**, 1–10 (2017).

81. Domínguez, R. A. S., Hinostroza, O. O., Díaz, A. O. & Jiménez, M. Á. D. Antibody Immobilization in ZnO-Thin Film Transistors for Low-Cost Biosensors Applications. *Engineering Proceedings 2021, Vol. 4, Page 23* **4**, 23 (2021).

82. Safavipour, M., Kharaziha, M., Amjadi, E., Karimzadeh, F. & Allafchian, A. TiO2 nanotubes/reduced GO nanoparticles for sensitive detection of breast cancer cells and photothermal performance. *Talanta* **208**, 120369 (2020).

83. Nath, N. & Chilkoti, A. Label-free biosensing by surface plasmon resonance of nanoparticles on glass: Optimization of nanoparticle size. *Anal Chem* **76**, 5370–5378 (2004).

84. Tanak, A. S., Jagannath, B., Tamrakar, Y., Muthukumar, S. & Prasad, S. Non-faradaic electrochemical impedimetric profiling of procalcitonin and C-reactive protein as a dual marker biosensor for early sepsis detection. *Anal Chim Acta X* **3**, 100029 (2019).

85. Tang, R. *et al.* Nitrocellulose Membrane for Paper-based Biosensor. *Appl Mater Today* **26**, 101305 (2022).

86. Tang, R. *et al.* Improved Analytical Sensitivity of Lateral Flow Assay using Sponge for HBV Nucleic Acid Detection. *Sci Rep* **7**, (2017).

87. Quesada-González, D. *et al.* Signal enhancement on gold nanoparticle-based lateral flow tests using cellulose nanofibers. *Biosens Bioelectron* **141**, (2019).

88. Sivaselvi, K. & Ghosh, P. Characterization of modified Chitosan thin film. in *Materials Today: Proceedings* vol. 4 442–451 (Elsevier Ltd, 2017).

89. Cao, L., Kiely, J., Piano, M. & Luxton, R. Nanoparticle-based 3D membrane for impedimetric biosensor applications. *Bioelectrochemistry* **136**, 107593 (2020).

90. Naresh, V. & Lee, N. A Review on Biosensors and Recent Development of Nanostructured Materials-Enabled Biosensors. *Sensors 2021, Vol. 21, Page 1109* **21**, 1109 (2021).

91. Grieshaber, D., MacKenzie, R., Vörös, J. & Reimhult, E. Electrochemical Biosensors - Sensor Principles and Architectures. *Sensors (Basel)* **8**, 1400–1458 (2008).

92. Ding, J. & Qin, W. Recent advances in potentiometric biosensors. *TrAC Trends in Analytical Chemistry* **124**, 115803 (2020).

93. Chaubey, A. & Malhotra, B. D. Mediated biosensors. *Biosens Bioelectron* **17**, 441–456 (2002).

94. Beck, F. Cyclic voltammetry—simulation and analysis of reaction mechanisms. By David K. Gosser, Jr., VCH, New York 1993, xi, 154 pp., hardcover, DM 124.00, ISBN 3-527-28226-2, disks included (5 1/4″ and 3 1/2″). *Electroanalysis* **7**, 298–298 (1995).

95. Martins, T. D. *et al.* New Insights on Optical Biosensors: Techniques, Construction and Application. *State of the Art in Biosensors - General Aspects* (2013) doi:10.5772/52330.

96. Zhang, J. *et al.* Visualization of caspase-3-like activity in cells using a genetically encoded fluorescent biosensor activated by protein cleavage. *Nature Communications 2013 4:1* **4**, 1–13 (2013).

97. Koulov, A. v., Stucker, K. A., Lakshmi, C., Robinson, J. P. & Smith, B. D. Detection of apoptotic cells using a synthetic fluorescent sensor for membrane surfaces that contain phosphatidylserine. *Cell Death & Differentiation 2003 10:12* **10**, 1357–1359 (2003).

98. Pan, Y. *et al.* Colorimetric detection of apoptosis based on caspase-3 activity assay using unmodified gold nanoparticlesw. *Chem. Commun* **48**, 997–999 (2012).

99. Skládal, P. Piezoelectric biosensors. *TrAC Trends in Analytical Chemistry* **79**, 127–133 (2016).

100. Tong, F., Lian, Y., Zhou, H., Shi, X. & He, F. Multichannel series piezoelectric quartz crystal cell sensor for real time and quantitative monitoring of the living cell and assessment of cytotoxicity. *Anal Chem* **86**, 10415–10421 (2014).

101. Peduru Hewa, T. M., Tannock, G. A., Mainwaring, D. E., Harrison, S. & Fecondo, J. v. The detection of influenza A and B viruses in clinical specimens using a quartz crystal microbalance. *J Virol Methods* **162**, 14 (2009).

102. Magar, H. S., Hassan, R. Y. A. & Mulchandani, A. Electrochemical Impedance Spectroscopy (EIS): Principles, Construction, and Biosensing Applications. *Sensors (Basel)* **21**, (2021).

103. Manickam, A., Chevalier, A., McDermott, M., Ellington, A. D. & Hassibi, A. A CMOS Electrochemical Impedance Spectroscopy (EIS) Biosensor Array. *IEEE Trans Biomed Circuits Syst* **4**, 379–390 (2010).

104. Xia, N. *et al.* Impedimetric biosensor for assay of caspase-3 activity and evaluation of cell apoptosis using self-assembled biotin-phenylalanine network as signal enhancer. *Sens Actuators B Chem* **320**, 128436 (2020).

105. Deng, D. *et al.* A signal-on electrochemical biosensor for evaluation of caspase-3 activity and cell apoptosis by the generation of molecular electrocatalysts on graphene electrode surface for water oxidation. *Sens Actuators B Chem* **286**, 415–420 (2019).

106. Ohno, R. *et al.* Electrochemical impedance spectroscopy biosensor with interdigitated electrode for detection of human immunoglobulin A. *Biosens Bioelectron* **40**, 422–426 (2013).

107. Hung, V. W. S. *et al.* Electrochemical impedance spectroscopy for monitoring caspase-3 activity. *Electrochim Acta* **162**, 79–85 (2015).

108. Adriano Dorledo de Faria, R., Guilherme Dias Heneine, L., Matencio, T. & Messaddeq, Y. Faradaic and non-faradaic electrochemical impedance spectroscopy as transduction techniques for sensing applications. doi:10.15406/ijbsbe.2019.05.00148.

109. Lin, S. P., Vinzons, L. U., Kang, Y. S. & Lai, T. Y. Non-faradaic electrical impedimetric investigation of the interfacial effects of neuronal cell growth and differentiation on silicon nanowire transistors. *ACS Appl Mater Interfaces* **7**, 9866–9878 (2015).

110. Krukiewicz, K. Electrochemical impedance spectroscopy as a versatile tool for the characterization of neural tissue: A mini review. *Electrochem commun* **116**, 106742 (2020).

111. Cao, L., Kiely, J., Piano, M. & Luxton, R. A copper oxide/zinc oxide composite nano-surface for use in a biosensor. *Materials* **12**, (2019).

112. Sakamoto, S. *et al.* Enzyme-linked immunosorbent assay for the quantitative/qualitative analysis of plant secondary metabolites. *J Nat Med* **72**, 32 (2018).

113. Vabbina, P. K., Kaushik, A., Pokhrel, N., Bhansali, S. & Pala, N. Electrochemical cortisol immunosensors based on sonochemically synthesized zinc oxide 1D nanorods and 2D nanoflakes. *Biosens Bioelectron* **63**, 124–130 (2015).

114. Salgame, P. *et al.* An ELISA for Detection of Apoptosis. *Nucleic Acids Res* **25**, 680–681 (1997).

115. Chen, Y.-J. *et al.* Combining Whispering-Gallery Mode Optical Biosensors with Microfluidics for Real-Time Detection of Protein Secretion from Living Cells in Complex Media. *Small* **14**, 1703705 (2018).

116. Chen, N., Huang, Y., Yang, L., Liu, R. & Yang, J. J. Designing Caspase-3 Sensors for Imaging of Apoptosis in Living Cells. *Chemistry* **15**, 9311 (2009).

117. Cai, Y., Kang, K., Liu, Y., Wang, Y. & He, X. Development of a lateral flow immunoassay of C-reactive protein detection based on red fluorescent nanoparticles. *Anal Biochem* **556**, 129–135 (2018).

118. Sixiang, S. *et al.* Amperometric Detection of Apoptosis by using p-Methoxyaniline-Conjugated Substrate for Caspase-3. *ChemElectroChem* **4**, 941–946 (2017).

119. Shin, J. H. *et al.* Electrochemical detection of caspase-3 based on a chemically modified M13 phage virus. *Bioelectrochemistry* **145**, 108090 (2022).

120. Gasser, A., Eveness, J., Kiely, J., Attwood, D. & Luxton, R. A non-contact impedimetric biosensing system for classification of toxins associated with cytotoxicity testing. *Bioelectrochemistry* **133**, 107448 (2020).

121. Shen, Y. C. *et al.* IGZO thin film transistor biosensors functionalized with ZnO nanorods and antibodies. *Biosens Bioelectron* **54**, 306–310 (2014).

122. Deng, D. *et al.* A signal-on electrochemical biosensor for evaluation of caspase-3 activity and cell apoptosis by the generation of molecular electrocatalysts on graphene electrode surface for water oxidation. *Sens Actuators B Chem* **286**, 415–420 (2019).

123. Arya, S. K. *et al.* Recent advances in ZnO nanostructures and thin films for biosensor applications: Review. *Anal Chim Acta* **737**, 1–21 (2012).

124. Shanmugam, N. R., Muthukumar, S. & Prasad, S. A review on ZnO-based electrical biosensors for cardiac biomarker detection. *Future Sci OA* **3**, FSO196 (2017).

125. Batra, N., Tomar, M. & Gupta, V. ZnO-CuO composite matrix based reagentless biosensor for detection of total cholesterol. *Biosens Bioelectron* **67**, 263–71 (2015).

126. Gerbreders, V. *et al.* ZnO nanostructure-based electrochemical biosensor for Trichinella DNA detection. *Sens Biosensing Res* **23**, 100276 (2019).

127. Shi, J. & Marshall, D. Surface Modification Approaches for Electrochemical Biosensors. in *Biosensors - Emerging Materials and Applications* (InTech, 2011). doi:10.5772/17770.

128. Yakimova, R. *et al.* ZnO materials and surface tailoring for biosensing. *Frontiers in Bioscience - Elite* **4 E**, 254–278 (2012).

129. Olejnik, M. *et al.* Cell-biological effects of zinc oxide spheres and rods from the nano- to the microscale at sub-toxic levels. *Cell Biol Toxicol* 1–21 (2020) doi:10.1007/s10565-020-09571-z.

130. Stefaniuk, I., Cieniek, B., Rogalska, I., Virt, I. S. & Kosciak, A. Magnetic properties of ZnO:Co layers obtained by pulsed laser deposition method. *Materials Science- Poland* **36**, 439–444 (2018).

131. Yuan, H. *et al.* Electrostatic and electrochemical nature of liquid-gated electric-double-layer transistors based on oxide semiconductors. *J Am Chem Soc* **132**, 18402–18407 (2010).

132. Janotti, A. & van de Walle, C. G. Fundamentals of zinc oxide as a semiconductor. *Reports on Progress in Physics* **72**, 126501 (2009).

133. Tripathy, N. & Kim, D. H. Metal oxide modified ZnO nanomaterials for biosensor applications. *Nano Convergence* vol. 5 Preprint at https://doi.org/10.1186/s40580-018-0159-9 (2018).

134. Karunakaran, C., Vinayagamoorthy, P. & Jayabharathi, J. Nonquenching of charge carriers by Fe3O4 core in Fe3O4/ZnO nanosheet photocatalyst. *Langmuir* **30**, 15031–15039 (2014).

135. Qian, J. *et al.* Non-enzymatic glucose sensor based on ZnO–CeO2 whiskers. *Mater Chem Phys* **239**, 122051 (2020).

136. Bertel, L. *et al.* Nanostructured Titanium Dioxide Surfaces for Electrochemical Biosensing. *Sensors 2021, Vol. 21, Page 6167* **21**, 6167 (2021).

137. Lee, J. E. *et al.* ZnO-CuO Core-Hollow Cube Nanostructures for Highly Sensitive Acetone Gas Sensors at the ppb Level. *ACS Appl Mater Interfaces* **12**, 35688–35697 (2020).

138. Aryanto, D. *et al.* Preparation and structural characterization of ZnO thin films by sol-gel method. *J Phys Conf Ser* **817**, 012025 (2017).

139. Khan, M. I., Bhatti, K. A., Qindeel, R., Alonizan, N. & Althobaiti, H. S. Characterizations of multilayer ZnO thin films deposited by sol-gel spin coating technique. *Results Phys* **7**, 651–655 (2017).

140. Zheng, X. *et al*. Tunable channel width of a UV-gate field effect transistor based on ZnO micro-nano wire. *RSC Adv* **4**, 18378 (2014).

141. Tripathy, N. & Kim, D.-H. Metal oxide modified ZnO nanomaterials for biosensor applications. *Nano Converg* **5**, 27 (2018).

142. Munje, R. D., Muthukumar, S. & Prasad, S. Lancet-free and label-free diagnostics of glucose in sweat using Zinc Oxide based flexible bioelectronics. *Sens Actuators B Chem* **238**, 482–490 (2017).

143. Cao, L., Kiely, J., Piano, M. & Luxton, R. Facile and inexpensive fabrication of zinc oxide based bio-surfaces for C-reactive protein detection. *Sci Rep* **8**, 12687 (2018).

144. Morfa, A. J. *et al.* Fabrication of ZnO thin films from nanocrystal inks. *Journal of Physical Chemistry C* **114**, 19815–19821 (2010).

145. Anusha, J. R. *et al.* Simple fabrication of ZnO/Pt/chitosan electrode for enzymatic glucose biosensor. *Sens Actuators B Chem* **202**, 827–833 (2014).

146. Thonglerth, P., Sujaridworakun, P. & Boondamnoen, O. Preparation of ZnO Nanoparticles Water-based Dispersion. *J Phys Conf Ser* **2175**, 012029 (2022).

147. Cao, D., Gong, S., Shu, X., Zhu, D. & Liang, S. Preparation of ZnO Nanoparticles with High Dispersibility Based on Oriented Attachment (OA) Process. *Nanoscale Res Lett* **14**, 1–11 (2019).

148. Anand, K. & Varghese, S. Role of surfactants on the stability of nano-zinc oxide dispersions. *http://dx.doi.org/10.1080/02726351.2015.1131787* **35**, 67–70 (2016).

149. Chung, S. J. *et al.* Characterization of ZnO nanoparticle suspension in water: Effectiveness of ultrasonic dispersion. *Powder Technol* **194**, 75–80 (2009).

150. Lee, K. S. *et al*. Ultrasonic fabrication of flexible antibacterial ZnO nanopillar array film. *Colloids Surf B Biointerfaces* **170**, 172–178 (2018).

151. Kivirand, K., Min, M. & Rinken, T. Challenges and Applications of Impedance-Based Biosensors in Water Analysis. *Biosensors for Environmental Monitoring* (2019) doi:10.5772/INTECHOPEN.89334.

152. Shanmugam, N. R., Muthukumar, S. & Prasad, S. Ultrasensitive and low-volume point-of-care diagnostics on flexible strips-a study with cardiac troponin biomarkers. *Sci Rep* **6**, 1–10 (2016).

153. Kazemi, H. *et al.* Ultra-Sensitive Radio Frequency Biosensor at an Exceptional Point of Degeneracy induced by Time Modulation. *IEEE Sens J* **21**, 7250–7259 (2019).

154. Strong, M. E., Richards, J. R., Torres, M., Beck, C. M. & La Belle, J. T. Faradaic electrochemical impedance spectroscopy for enhanced analyte detection in diagnostics. *Biosens Bioelectron* **177**, 112949 (2021).

155. Prodromidis, M. I. Impedimetric immunosensors—A review. *Electrochim Acta* **55**, 4227–4233 (2010).

156. Lin, K. C., Jagannath, B., Muthukumar, S. & Prasad, S. Sub-picomolar label-free detection of thrombin using electrochemical impedance spectroscopy of aptamer-functionalized MoS2. *Analyst* **142**, 2770–2780 (2017).

157. Luo, X., Xu, M., Freeman, C., James, T. & Davis, J. J. Ultrasensitive Label Free Electrical Detection of Insulin in Neat Blood Serum. *Anal Chem* **85**, 4129–4134 (2013).

158. Garrote, B. L., Santos, A. & Bueno, P. R. Label-free capacitive assaying of biomarkers for molecular diagnostics. *Nature Protocols 2020 15:12* **15**, 3879–3893 (2020).

159. Ahmed, A., Rushworth, J. V., Wright, J. D. & Millner, P. A. Novel impedimetric immunosensor for detection of pathogenic bacteria Streptococcus pyogenes in human saliva. *Anal Chem* **85**, 12118–12125 (2013).

160. Wen, Q., Zhang, X., Cai, J. & Yang, P. H. A novel strategy for real-time and in situ detection of cytochrome c and caspase-9 in Hela cells during apoptosis. *Analyst* **139**, 2499–2506 (2014).

161. Deniz, H. & Onur, Z. Impedimetric Biosensors for Label-Free and Enzymless Detection. in *State of the Art in Biosensors - General Aspects* (InTech, 2013). doi:10.5772/52169.

162. Park, J. S. *et al.* Amyloid Beta Detection by Faradaic Electrochemical Impedance Spectroscopy Using Interdigitated Microelectrodes. *Sensors (Basel)* **18**, (2018).

163. Mozaffari, S. A., Rahmanian, R., Abedi, M. & Amoli, H. S. Urea impedimetric biosensor based on reactive RF magnetron sputtered zinc oxide nanoporous transducer. *Electrochim Acta* **146**, 538–547 (2014).

164. Lin, K. C. *et al.* Biogenic nanoporous silica-based sensor for enhanced electrochemical detection of cardiovascular biomarkers proteins. *Biosens Bioelectron* **25**, 2336–2342 (2010).

165. Khademi, M. & Barz, D. P. J. Structure of the Electrical Double Layer Revisited: Electrode Capacitance in Aqueous Solutions. *Langmuir* **36**, 4250–4260 (2020).

166. Munje, R. D., Muthukumar, S., Panneer Selvam, A. & Prasad, S. Flexible nanoporous tunable electrical double layer biosensors for sweat diagnostics. *Scientific Reports 2015 5:1* **5**, 1–11 (2015).

167. Morgado, J. Modulation of the electrical double layer in metals and conducting polymers. *Scientific Reports 2022 12:1* **12**, 1–5 (2022).

168. Ertürk, G. & Mattiasson, B. Capacitive Biosensors and Molecularly Imprinted Electrodes. *Sensors (Basel)* **17**, (2017).

169. Dorledo de Faria, R. A., Dias Heneine, L. G., Matencio, T. & Messaddeq, Y. Faradaic and non-faradaic electrochemical impedance spectroscopy as transduction techniques for sensing applications. *Int J Biosens Bioelectron* **Volume 5**, (2019).

170. Eveness, J., Cao, L., Kiely, J. & Luxton, R. Equivalent circuit model of a non-faradaic impedimetric ZnO nano-crystal biosensor. *Journal of Electroanalytical Chemistry* **906**, 116003 (2022).

171. Jacobs, M., Muthukumar, S., Panneer Selvam, A., Engel Craven, J. & Prasad, S. Ultra-sensitive electrical immunoassay biosensors using nanotextured zinc oxide thin films on printed circuit board platforms. *Biosens Bioelectron* **55**, 7–13 (2014).

172. Panneer Selvam, A., Muthukumar, S., Kamakoti, V. & Prasad, S. A wearable biochemical sensor for monitoring alcohol consumption lifestyle through Ethyl glucuronide (EtG) detection in human sweat. *Scientific Reports 2016 6:1* **6**, 1–11 (2016).

173. Palazzo, G. *et al.* Detection Beyond Debye's Length with an Electrolyte-Gated Organic Field-Effect Transistor. *Advanced Materials* **27**, 911–916 (2015).

174. Smith, A. M., Lee, A. A. & Perkin, S. The Electrostatic Screening Length in Concentrated Electrolytes Increases with Concentration. *Journal of Physical Chemistry Letters* **7**, 2157–2163 (2016).

175. Pungetmongkol, P., Mogi, K., Hatsuki, R. & Yamamoto, T. Direct Evaluation of the Electrokinetic Properties of Electrolytes in a Nanochannel using Electrical Impedance Spectroscopy. *Isr J Chem* **54**, 1607–1614 (2014).

176. Amin, M. & Küpper, J. Variations in Proteins Dielectric Constants. *ChemistryOpen* **9**, 691 (2020).

177. Li, P. *et al.* Caspase-9: structure, mechanisms and clinical application. *Oncotarget* **8**, 23996–24008 (2017).

178. Erickson, H. P. Size and Shape of Protein Molecules at the Nanometer Level Determined by Sedimentation, Gel Filtration, and Electron Microscopy. *Biol Proced Online* **11**, 32 (2009).

179. Kesler, V., Murmann, B. & Soh, H. T. Going beyond the Debye Length: Overcoming Charge Screening Limitations in Next-Generation Bioelectronic Sensors. *ACS Nano* **14**, 16194–16201 (2020).

180. Widdershoven, F. *et al.* CMOS biosensor platform. *Technical Digest - International Electron Devices Meeting, IEDM* (2010) doi:10.1109/IEDM.2010.5703484.

181. Laborde, C. *et al.* Real-time imaging of microparticles and living cells with CMOS nanocapacitor arrays. *Nat Nanotechnol* **10**, 791–795 (2015).

182. Ghoreishizadeh, S. S., Zhang, X., Sharma, S. & Georgiou, P. Study of Electrochemical Impedance of a Continuous Glucose Monitoring Sensor and its Correlation with Sensor Performance. *IEEE Sens Lett* **2**, (2018).

183. Xu, Y., Li, C., Mei, W., Guo, M. & Yang, Y. Equivalent circuit models for a biomembrane impedance sensor and analysis of electrochemical impedance spectra based on support vector regression. *Med Biol Eng Comput* **57**, 1515–1524 (2019).

184. Dak, P., Ebrahimi, A. & Alam, M. A. Non-faradaic impedance characterization of an evaporating droplet for microfluidic and biosensing applications. *Lab Chip* **14**, 2469–2479 (2014).

185. Kechadi, M., Chaal, L., Vivier, V., Tribollet, B. & Gamby, J. Finite element modelling of non-faradic electric impedance spectroscopy through flexible polymer microchip. *Journal of Electroanalytical Chemistry* **807**, 203–212 (2017).

186. Wang, Z., Hu, Y., Lu, H. & Yu, F. Dielectric properties and crystalline characteristics of borosilicate glasses. *J Non Cryst Solids* **354**, 1128–1132 (2008).

187. Yunus, Y. *et al.* Review of the Common Deposition Methods of Thin-Film Pentacene, Its Derivatives, and Their Performance. *Polymers 2022, Vol. 14, Page 1112* **14**, 1112 (2022).

188. Lee, J. K. *et al.* Regenerative Strategy of Gold Electrodes for Long-Term Reuse of Electrochemical Biosensors. *ACS Omega* **8**, 1389 (2022).

189. Thonglerth, P., Sujaridworakun, P. & Boondamnoen, O. Preparation of ZnO Nanoparticles Water-based Dispersion. *J Phys Conf Ser* **2175**, 012029 (2022).

190. Rimbu, C. *et al.* Zinc oxide application in the textile industry: surface tailoring and water barrier attributes as parameters with direct implication in comfort performance. *http://dx.doi.org/10.1177/0040517513478460* **83**, 2142–2151 (2013).

191. Navas, D., Ibañez, A., González, I., Palma, J. L. & Dreyse, P. Controlled dispersion of ZnO nanoparticles produced by basic precipitation in solvothermal processes. *Heliyon* **6**, e05821 (2020).

192. Nguyen, N.-T. Fabrication technologies. *Micromixers* 113–161 (2012) doi:10.1016/B978-1-4377-3520-8.00004-8.

193. Natsume, Y. & Sakata, H. Zinc oxide films prepared by sol-gel spin-coating. *Thin Solid Films* **372**, 30–36 (2000).

194. Widiarti, N., Sae, J. K. & Wahyuni, S. Synthesis CuO-ZnO nanocomposite and its application as an antibacterial agent. *IOP Conf Ser Mater Sci Eng* **172**, 012036 (2017).

195. Perry, S. C., Gateman, S. M., Sifakis, J., Pollegioni, L. & Mauzeroll, J. Enhancement of the Enzymatic Biosensor Response through Targeted Electrode Surface Roughness. *J Electrochem Soc* **165**, G3074–G3079 (2018).

196. Kang, M. *et al.* Nanoconfined 3D redox capacitor-based electrochemical sensor for ultrasensitive monitoring of metabolites in bacterial communication. *Sens Actuators B Chem* **345**, 130427 (2021).

197. Fatehah, M. O., Aziz, H. A. & Stoll, S. Stability of ZnO Nanoparticles in Solution. Influence of pH, Dissolution, Aggregation and Disaggregation Effects. *Journal of Colloid Science and Biotechnology* **3**, 75–84 (2014).

198. Sousa, V. S. & Teixeira, M. R. Aggregation kinetics and surface charge of CuO nanoparticles: the influence of pH, ionic strength and humic acids. *Environmental Chemistry* **10**, 313 (2013).

199. Li, G. *et al.* Purification of human immunoglobulin G: A new approach to plasma fractionation. *Vox Sang* **83**, 332–338 (2002).

200. Katz, E. & Willner, I. Probing Biomolecular Interactions at Conductive and Semiconductive Surfaces by Impedance Spectroscopy: Routes to Impedimetric Immunosensors, DNA-Sensors, and Enzyme Biosensors. *Electroanalysis* **15**, 913–947 (2003).

201. Oseev, A., Schmidt, M. P., Hirsch, S., Brose, A. & Schmidt, B. Two-component dielectric dispersion impedance biosensor for in-line protein monitoring. *Sens Actuators B Chem* **239**, 1213–1220 (2017).

202. Santos, A., Davis, J. J. & Bueno, P. R. Fundamentals and Applications of Impedimetric and Redox Capacitive Biosensors. *Journal of Analytical & Bioanalytical Techniques 2015 0:0* **S7**, (2014).

203. Reverberi, R. & Reverberi, L. Factors affecting the antigen-antibody reaction. *Blood Transfusion* **5**, 227 (2007).

204. Riquelme, M. v. *et al.* Optimizing blocking of nonspecific bacterial attachment to impedimetric biosensors. *Sens Biosensing Res* **8**, 47–54 (2016).

205. Sabry, R. S., Alkareem, R. A. S. A., Sabry, R. S. & Alkareem, R. A. S. A. Synthesis of ZnO-CuO flower-like hetero-nanostructures as volatile organic compounds (VOCs) sensor at room temperature. *MatSP* **36**, 452–459 (2018).

206. Wang, W. *et al.* Electrospun palladium (IV)-doped copper oxide composite nanofibers for non-enzymatic glucose sensors. *Electrochem commun* **11**, 1811–1814 (2009).

207. Chitralekha *et al.* Dielectric and impedance studies of binary ZnO–CuO nanocomposites for hydroelectric cell application. *Mater Chem Phys* **291**, 126690 (2022).

208. Gurtu, V., Kain, S. R. & Zhang, G. Fluorometric and Colorimetric Detection of Caspase Activity Associated with Apoptosis. *Anal Biochem* **251**, 98–102 (1997).

209. Khalilzadeh, B. *et al.* A reliable self-assembled peptide based electrochemical biosensor for detection of caspase 3 activity and apoptosis. *RSC Adv* **5**, 58316–58326 (2015).

210. Qi, G. *et al.* Fast Activation and Tracing of Caspase-3 Involved Cell Apoptosis by Combined Electrostimulation and Smart Signal-Amplified SERS Nanoprobes. *Anal Chem* **92**, 7861–7868 (2020).

211. Xia, N. *et al.* Protease Biosensor by Conversion of a Homogeneous Assay into a Surface-Tethered Electrochemical Analysis Based on Streptavidin-Biotin Interactions. *ACS Sens* **6**, 1166–1173 (2021).

212. Luo, K. Q., Yu, V. C., Pu, Y. & Chang, D. C. Measuring dynamics of caspase-8 activation in a single living HeLa cell during TNFα-induced apoptosis. *Biochem Biophys Res Commun* **304**, 217–222 (2003).

213. Chen, B., Kiely, J., Williams, I. & Luxton, R. A non-faradaic impedimetric biosensor for monitoring of caspase 9 in mammalian cell culture. *Bioelectrochemistry* **153**, 108456 (2023).

214. Guo, M. *et al.* Apoptosis detection: a purpose-dependent approach selection. *Cell Cycle* **20**, 1033 (2021).

215. Doonan, F. & Cotter, T. G. Morphological assessment of apoptosis. *Methods* **44**, 200–204 (2008).

216. Galluzzi, L. *et al.* Guidelines for the use and interpretation of assays for monitoring cell death in higher eukaryotes. *Cell Death & Differentiation 2009 16:8* **16**, 1093–1107 (2009).

217. Helmy, I. M. & Abdel Azim, A. M. Efficacy of ImageJ in the assessment of apoptosis. *Diagn Pathol* (2012) doi:10.1186/1746-1596-7-15.

218. Eidet, J. R., Pasovic, L., Maria, R., Jackson, C. J. & Utheim, T. P. Objective assessment of changes in nuclear morphology and cell distribution following induction of apoptosis. *Diagn Pathol* (2014) doi:10.1186/1746-1596-9-92.

219. Jin, J. *et al.* Machine Learning Classifies Ferroptosis and Apoptosis Cell Death Modalities with TfR1 Immunostaining. *ACS Chem Biol* **17**, 654–660 (2022).

220. Slee, E. A., Adrain, C. & Martin, S. J. Serial killers: ordering caspase activation events in apoptosis. *Cell Death Differ* **6**, 1067–1074 (1999).

221. Xia, N. *et al.* Protease Biosensor by Conversion of a Homogeneous Assay into a Surface-Tethered Electrochemical Analysis Based on Streptavidin-Biotin Interactions. *ACS Sens* **6**, 1166–1173 (2021).

222. O'Brien, M. *et al.* A bioluminescent caspase-1 activity assay rapidly monitors inflammasome activation in cells. *J Immunol Methods* **447**, 1–13 (2017).

223. Ehrnhoefer, D. E. *et al.* A Quantitative Method for the Specific Assessment of Caspase-6 Activity in Cell Culture. *PLoS One* **6**, 27680 (2011).

224. Gregoraszczuk, E. L., Rak-Mardyła, A., Ryś, J., Jakubowicz, J. & Urbański, K. Effect of Chemotherapeutic Drugs on Caspase-3 Activity, as a Key Biomarker for Apoptosis in Ovarian Tumor Cell Cultured as Monolayer. A Pilot Study. *Iran J Pharm Res* **14**, 1153 (2015).

225. Liu, Q., Wang, J. & Boyd, B. J. Peptide-based biosensors. *Talanta* **136**, 114–127 (2015).

226. Liu, J. *et al.* Fluorescent molecular probes V: A sensitive caspase-3 substrate for fluorometric assays. *Bioorg Med Chem Lett* **9**, 3231–3236 (1999).

227. Monsees, T., Geiger, R. & Miska, W. A novel bioluminogenic assay for α-chymotrypsin. *J Biolumin Chemilumin* **10**, 213–218 (1995).

228. HTN, L., J, P. & S, C. A Probeless Capacitive Biosensor for Direct Detection of Amyloid Beta 1-42 in Human Serum Based on an Interdigitated Chain-Shaped Electrode. *Micromachines (Basel)* **11**, (2020).

229. Couniot, N., Francis, L. A. & Flandre, D. A 16 × 16 CMOS Capacitive Biosensor Array Towards Detection of Single Bacterial Cell. *IEEE Trans Biomed Circuits Syst* **10**, 364–374 (2016).

230. Belmokhtar, C. A., Hillion, J. & Ségal-Bendirdjian, E. Staurosporine induces apoptosis through both caspase-dependent and caspase-independent mechanisms. *Oncogene* **20**, 3354–3362 (2001).

231. Zhang, G., Yan, G., Gurtu, V., Spencer, C. & Kain, S. R. Caspase inhibition prevents staurosporine-induced apoptosis in CHO-K1 cells. *Apoptosis* **3**, 27–33 (1998).

232. Saraste, A. & Pulkki, K. Morphologic and biochemical hallmarks of apoptosis. *Cardiovasc Res* **45**, 528–537 (2000).

233. S. Afifi, N., Abdel-Hamid, E. S. & M. Baghdadi, H. Nuclear Area Factor as a Novel Estimate for Apoptosis in Oral Squamous Cell Carcinoma -Treated Cell Line: A Comparative in-vitro Study with DNA Fragmentation Assay. *J Clin Exp Pathol* (2012) doi:10.4172/2161-0681.1000107.

234. Hussain, S. S., Faizi, S., Rafi, K. & Simjee, S. U. Novel Mannich base 3FB3FA8H induces apoptosis by upregulating P53 pathway in neuroblastoma cells. *Mol Cell Biochem* (2020) doi:10.1007/s11010-020-03755-1.

235. Mokhtar-Ahmadabadi, R. *et al.* Developing a circularly permuted variant of Renilla luciferase as a bioluminescent sensor for measuring Caspase-9 activity in the cell-free and cell-based systems. *Biochem Biophys Res Commun* **506**, 1032–1039 (2018).

236. Peña-Bahamonde, J., Nguyen, H.N., Fanourakis, S.K. et al. Recent advances in graphene-based biosensor technology with applications in life sciences. *J Nanobiotechnol* 16, 75 (2018). https://doi.org/10.1186/s12951-018-0400-z

237. Kailashiya J, Singh N, Singh SK, Agrawal V, Dash D. Graphene oxide-based biosensor for detection of platelet-derived microparticles: A potential tool for thrombus risk identification. *Biosens Bioelectron*. 2015 Mar 15;65:274-80. doi: 10.1016/j.bios.2014.10.056. Epub 2014 Oct 28. PMID: 25461169.

238. Y. Zhang, T. R. Nayak, H. Hong and W. Cai. Biomedical Applications of Zinc Oxide Nanomaterials. *Current Molecular Medicine*. Volume 13, Issue 10, 2013. doi: 10.2174/15665240136661311111130058